Electronic structure and lattice relaxations

in

quantum confined Pb films

Electronic structure and lattice relaxations
in
quantum confined Pb films

Proefschrift

ter verkrijging van de graad van doctor
aan de Technische Universtiteit Delft,
op gezag van de Rector Magnificus prof.dr.ir. J.T. Fokkema,
voorzitter van het College van Promoties,
in het openbaar te verdedigen op maandag 17 januari 2005 om 15:30 uur
door

Antonie MANS

natuurkundig ingenieur
geboren te Dordrecht.

Dit proefschrift is goedgekeurd door de promotoren:
Prof.dr. H.H. Weitering
Prof.dr.ir. F. Tuinstra

Samenstelling promotiecommissie:

Rector Magnificus	voorzitter
Prof.dr. H.H. Weitering	The University of Tennessee, promotor
Prof.dr.ir. F. Tuinstra	Technische Universiteit Delft, promotor
Prof.dr. H.W.M. Salemink	Technische Universiteit Delft
Prof.dr. T. Hibma	Rijksuniversiteit Groningen
Prof.dr.ir. B. Poelsema	Universiteit Twente
Prof.dr. J. van Ruitenbeek	Universiteit Leiden
Dr. A.R.H.F. Ettema	Technische Universiteit Delft

Dr. A.R.H.F. Ettema heeft als begeleider aan de totstandkoming van het proefschrift bijgedragen.

Cover: Photoemission branches of Pb films on Si(111)7×7 crossing the Fermi level.

Voor Erika

Voor Michiel, Nanette en Jacqueline

Contents

Chapter 1

Introduction

1.1   History and development of the quantum theory

Never before in history, a scientific theory changed everyday life so drastically as the quantum theory has done. At the beginning of the 21th century life is dominated by technology which ultimately is founded on this theory. It is hard to imagine how society would have evolved if it had been deprived from the knowledge of quantum theory. There would probably be no television, no computers, no lasers, no GSM's and so on. Our world would still be ruled by (electro)mechanical means instead of microelectronics. This does not mean, however, that all of these devices have been developed by scientists with a thorough grasp of quantum theory. Microelectronic engineers do not need to know the underlying concepts of quantum theory in order to design a reliably working device.

The quantum theory has disseminated not only every day life, but nearly all branches of physics and chemistry. This is evident from the names given to these branches of science: quantum electro dynamics, quantum field theory, quantum statistics, quantum chemistry, and quantum mechanics. Although the theoretical foundations of the quantum theory are still under debate, its predictions have proven to be very reliable.

The quantum theory was initiated in the year 1900 by Max Planck, who announced a quantitatively exact formula for the radiation spectrum of a black body as a function of temperature. He had to assume discrete values for the energy of the emitted particles, i.e., energy quantization. In 1906 Albert Einstein postulated the particle nature of light in order to explain the photoelectric effect. Later he used this energy quantization to derive the specific heat of diatomic gasses. The development by Niels Bohr of a revolutionary model for the hydrogen atom, postulating quantization of angular momentum, is arguably the most important result during the first two decades of the twentieth century.
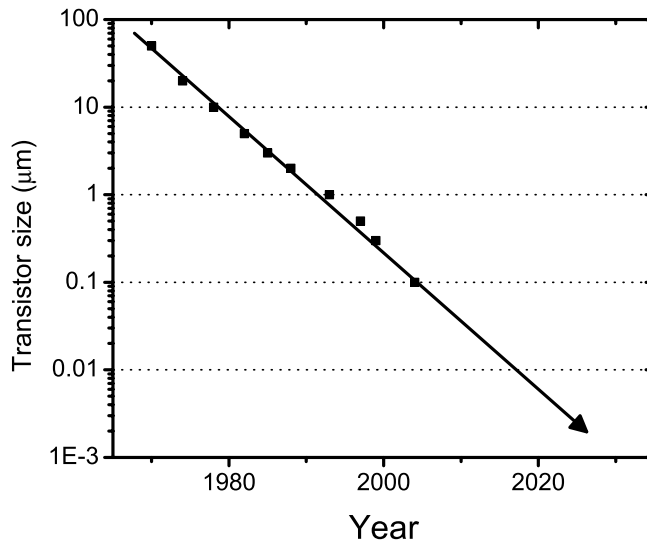
Figure 1.1: Development of the transistor size in integrated circuits versus time. Soon after the year 2030, the curve will reach the dimensions of a single atom.

These results of Planck, Einstein and Bohr initiated of a series of remarkable developments, having one thing in common: quantization of a physical property. Quantum theory soon evolved from a set of more or less ad hoc rules to a generally accepted and consistent scientific theory with sound mathematical basis. The correctness of the theory was illustrated in the forties and fifties by the fact that theoretical predictions were experimentally confirmed in different branches of science.

Quantum theory was soon used in applied science, including solid-state and materials science. The quantum theory of solids or 'band theory' was able to explain the tremendous variations in the electrical conductivity of solids and offered fundamental understanding of the difference between a metal and a semiconductor. The subsequent invention of the semiconductor transistor and the integrated circuit (IC) triggered a development of electronic devices of smaller and smaller size, leading to the microelectronics. Ever since the introduction of the IC, the dimensions of the working parts have been reduced. In 1965, Gordon Moore made the observation that the number of transistors per unit area in an IC doubles every 18 months. This trend (known as Moore's Law) has succeeded for decades and is still being fulfilled nowadays. Fig. 1.1 shows the development of the transistor size on a logarithmic scale versus time. From

the graph it is evident that this development must deviate from Moore's Law in the near future, since the transistor dimension will never decrease beyond the size of a single atom (~ 0.3 nm). This single atom limit is expected to be reached around the year 2030, but it is likely that Moore's law will fail even earlier.

Considering the natural limit of the single atom, the question arises whether it would be possible to design structures to be used in information technology from sub-atomic particles, like electrons, protons or even elementary particles. Nature has taught us that under terrestrially obtainable conditions of temperature and pressure the atomic configuration is the most stable by far compared to any other arrangement of (elementary) particles. Therefore, it is very unlikely that in the next decades sub-atomic information units will be available. Only when the obtainable conditions of pressure and temperature can be extended several orders of magnitude, one can start thinking of information technology based on sub-atomic entities (electrons in a plasma, for example).

Before reaching the atomic limit, Moore's curve will enter a regime where the quantum theory of the infinite crystal does not hold anymore and where the Schrödinger equation would have to be solved for each individual case, depending on the exact nature of the boundary conditions and on the exact number of interacting quantum particles. While so far the designer of microelectronics devices used the rules of quantum theory in everyday work, he did not need the ability to perform a complete quantum mechanical analysis. As the dimensions of the details in the IC shrink, however, a thorough grasp on the theory is needed. The fast approach of this regime is illustrated by the observation of significant deviation from the extrapolated properties in nanostructures of ~ 30 nm size [1], while commercially available chips have details smaller than 100 nm.

1.2   Nanoscience, nanophase materials, and the self organization of matter

1.2.1   Nanoscience

In nano*technology*, the focus is mostly on scaling down existing fabrication methods. The process of tailoring smaller and smaller devices in this way is called the *top-down* approach. Apart from the fundamental limitations mentioned above, somewhere in the near future this top-down approach will also fail because of the physical limitations of the fabrication methods used. Lithographical methods, for example, which are a common tool in microelectronics, are limited by the wavelength of the probing particles. Alternatively, the so-called *bottom-up* approach, i.e. building new structures atom-by-atom, was already envisioned some fifty years ago by Richard Feynman during his famous speech at Caltech [2]. Of course, building structures atom-by-atom would be

very labor intensive unless one can make clever use of the tendency of matter toward self-organization into stable or meta-stable structures. Meaningful experiments require a total control over the fabrication of these small devices on a nanometer scale. The subsection of physics studying these small structures and devices is nowadays called *nanoscience*.

1.2.2   Nanophase materials

Microelectronics and 'downscaling' are usually associated with silicon based materials. However, the promise of nanoscience and technology extends far beyond miniaturized silicon devices. Significant progress has been made in the field of 'advanced electronic materials', think for example of high T_c superconductivity, colossal magneto resistance (CMR), magnetic semiconductors, fullerenes, and carbon nanotubes. These novel materials often exhibit exotic physical properties, which involve some sort of nanoscale phase separation (e.g. stripes in high T_c materials, clustered phases in CMR materials and dilute magnetic semiconductors [3, 4]). One can easily imagine the significance and potential of these novel electronic materials for the advancement of nanoscience. Understanding nanoscale phase separation and its relation to exotic physical properties adds another dimension to the promise of nanoscience, especially if these properties can be further tuned using the tools and knowledgebase of nanoscience.

The material of interest in this thesis is Pb. We will show that the structure and properties of Pb can be tuned at the nanoscale. Since Pb is a superconductor (albeit a conventional type-I BCS superconductor), one could envision tuning superconductivity through controlled confinement at the nanoscale. Indeed, recent experiments indicate that ultrathin films of Pb are type-II superconductors with a thickness-dependent T_c, upper critical field, and critical current density [5].

1.2.3   Self organization

Self organization is a process where the organization of a system spontaneously increases, i.e. without this increase being controlled by the environment or an encompassing or otherwise external system. Self organization in the present context implies that the material under investigation assumes an ordered mesoscopic structure without the explicit intervention or involvement from the experimentalist. Nonetheless, to make clever use of this phenomenon, one needs to understand the relationship between chemical identity, (electronic) structure, and morphology. How dramatic the interplay between these three aspects can be was illustrated as early as 1984 by W.D. Knight et al. [6] who measured mass spectra of sodium clusters. Fig. 1.2 shows such a spectrum with an increased abundance of certain cluster masses, due to some kind of self organization. The so-called 'magic' numbers can be ex-
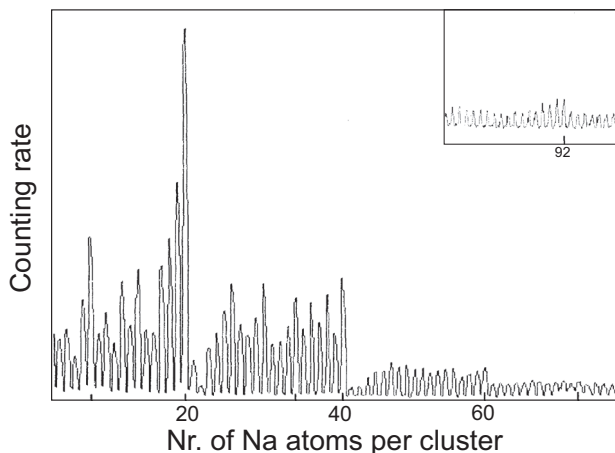
Figure 1.2: Mass spectrum of Na clusters. The observed 'magic' numbers in the relative abundance must be explained by quantum mechanics. Figure from W. D. Knight et. al. [6].

plained from elementary quantum mechanics. Electrons within the cluster assume a shell structure, analogous to the shell structure of free atoms. Certain clusters will have completely filled 'outermost' shells. Incorporation of additional atoms would require population of higher shells which is energetically unfavorable. Hence, clusters with completely filled shells are more abundant than clusters with partially filled shells. Other examples are self-assembled monolayers of lipids on the surface of liquids [7], or the formation of nanowires on vicinal surfaces [8, 9].

1.3   Scope and Outline

The above examples show the importance of the self organization for nanoscience and the bottom-up approach. However, there are still no microscopic techniques available to determine the atomic arrangement and positions in great detail. The Scanning Tunneling Microscope can only provide information about the local surface density of states and also (High Resolution) Transmission Electron Microscopy (HRTEM) has too many limitations for this purpose. Therefore, macroscopic techniques still have to be used to investigate the structure of nanoscale objects with sub-angstrom accuracy. With a macroscopic method we indicate that the technique provides the average atomic arrangement over a 'macroscopic' area. It does so, however, with sub-Angstrom precision and detail. In this thesis, we will show how a macroscopic structural tool can be used to precisely determine the atomic coordinates in a thin film nanostructure.

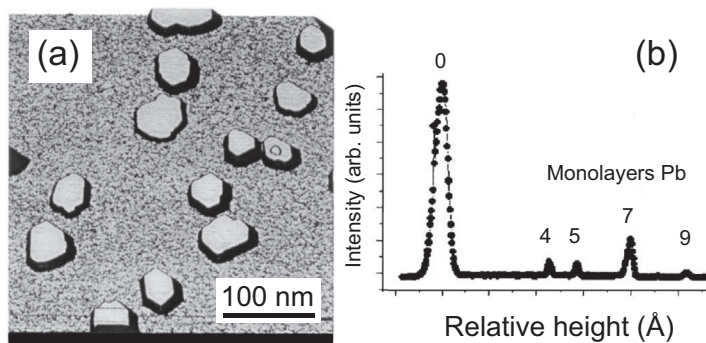Figure 1.3: a) STM image of Pb island on Si(111)7×7. b) Histogram of heights from the STM image of a) showing the magic thicknesses. Figure from W. B. Su et. al. [10].

This thesis deals with the manifestation of nanoscale phase separation and self organization in thin film growth, in particular the growth of Pb on Si(111). The behavior of ultrathin lead films on a Si(111)7×7 substrate has attracted considerable attention in the recent years. In the thickness regime of several monolayers of lead, quantum mechanics dictates the morphology of the film. In a way, this situation resembles that of the magic clusters discussed above. Fig. 1.3(a) shows an STM image of Pb islands grown at 180 K (lower temperatures provide smooth films) on Si(111)7×7, and (b) the corresponding histogram of heights. Magic numbers (or magic heights) occur in the histogram, just as in the case of the sodium clusters of Fig. 1.2; a clear manifestation of the quantum size effect (QSE).

In order to understand the thickness dependent stability of the lead films, detailed knowledge of the quantized energy spectrum of the electrons in the film is needed. The energy levels in thin films can be measured directly by photoemission spectroscopy, as will be analyzed in Chapter 3. First, we present an overview of previous contributions to this field and discuss the theoretical aspects of the relation between quantum electronic structure and thin film morphology (Chapter 2). The photoemission results of Chapter 3 will provide direct evidence for the increased stability (and abundance) of odd-numbered atom layers. This bilayer periodicity in the stability of the film can be understood from the bilayer periodicity in the quantum electronic structure of the films.

The atomic arrangements in these films is the subject of the second part of this thesis. The stable atomic arrangement in the solid state is determined by the forces between the electrons and atomic nuclei. Or more precisely formulated, the forces applied on the ion cores by the equilibrium charge distribution of the valence electrons. An infinite solid refers to a crystalline arrangement

which is thought to extend to infinity in all directions. In a nanoscale structure, however, this condition is not even approximately fulfilled. Due to the physical boundaries of a nanoscale object, forces on the ion cores and their final arrangement can differ appreciably from those in the bulk structure. The atomic displacements with respect to the bulk structure can to a certain extent be regarded as a relaxation from the bulk structure. In thin films these relaxations are dependent on the thickness of the film.

The lateral dimensions of a thin film are large compared to the thickness. For this reason macroscopic techniques can still be used to investigate the exact positions of the atoms. For example Pb films grown with the molecular beam epitaxial (MBE) technique fulfill this requirement. They can be viewed as having nanoscale dimensions in one direction only (perpendicular to the substrate) and 'macroscopic' size in the other directions. This makes them particularly suitable to explore the effect of nanoscale dimensions or 'quantum confinement' on structure and relaxation using a macroscopic diffraction technique. Low energy electron diffraction (LEED) and particularly the variety LEED I(V) is a suitable technique for this purpose, as it has proven its strength in surface structure determination [11]. Because of the low kinetic energy of the electrons they penetrate the solid by only a few atomic layers. In conventional LEED, the symmetry and ordering of the atoms at the surface is usually deduced from a visual inspection of the diffraction pattern. In LEED I(V), the energy dependent diffraction intensities are analyzed to find the precise atomic coordinates.

The second part of this thesis, consisting of the chapters 4 and 5, describes the theory of LEED I(V) and the results of the structure determination of the quantum confined Pb films, respectively. The analysis shows that the Pb lattice differs significantly between even- and odd-numbered layers. This behavior is perfectly consistent with the observations in chapter 3, which revealed a bilayer periodicity in the electronic structure and stability of the films. Together, these results prove that one-dimensional quantum confinement of Pb leads to a redistribution of the valence charge in the films which in turn induces a bilayer periodicity in the structure, electronic structure and stability. Because of its two-dimensional nature, the atomic response to the changing charge distribution is rather small, and can be compared to the periodic lattice distortions in 2D charge density wave compounds. Nonetheless, the valence charge redistribution in these 2D nanostructures does lead to a measurable displacement of the ionic core positions. This result is not only of fundamental importance but may even be a practical consideration in lower dimensions (1D, 0D) as researchers are trying to create novel nanostructures and devices.

Bibliography

[1] T. -C. Chiang, Surf. Sci. Rep. **39**, 181 (2000).

[2] R. P. Feynman, There's plenty of room at the bottom (http://www.zyvex.com/nanotech/feynman.html) (1959).

[3] G. Alvarez, M. Mayr, and E. Dagotto, Phys. Rev. Lett. **89**, 277202 (2002).

[4] A. P. Li, J. Shen, J. R. Thompson, and H. H. Weitering, Phys. Rev. Lett. submitted .

[5] M. M. Özer, J. R. Thompson, and H. H. Weitering, to be published .

[6] W. D. Knight *et al.*, Phys. Rev. Lett. **52**, 2141 (1984).

[7] V. M. Kaganer, H. Möhwald, and P. Dutta, Rev. Mod. Phys. **71**, 779 (1999).

[8] I. K. Robinson, P. A. Bennett, and F. J. Himpsel, Phys. Rev. Lett. **88**, 096104 (2002).

[9] K. Yoo *et al.*, Surf. Sci. **514**, 100 (2002).

[10] W. B. Su *et al.*, Phys. Rev. Lett. **86**, 5116 (2001).

[11] K. Heinz, Rep. Prog. Phys. **58**, 637 (1995).

Chapter 2

The Quantum Size Effect

2.1 Introduction

Over the past several years there has been great interest in the physics of the quantum size effect (QSE) in epitaxial metal layers on metals and semiconductors. Metal deposition on a suitable substrate can give rise to confinement of the valence electrons in the film, perpendicular to the surface. Due to the confinement of the valence electrons in the metal film, the wave number k_z of the electronic states becomes quantized. Physical properties of materials are closely related to their electronic structure and, consequently, quantum confined systems such as ultrathin metal films may exhibit novel properties. Examples include the thickness dependent stability of Pb films on Si(111) [1, 2] or Fe/Co superlattices [3], and the oscillatory ferromagnetic-antiferromagnetic coupling in Cu/Co superlattices [4].

This Chapter serves as an introduction to the physics of the quantum size effect in thin metal films and provides an historical overview of the relevant achievements in this field. First, the textbook example of a quantum particle (e.g. an electron) in the infinite and finite quantum well is discussed. Then the crystal lattice and band structure are introduced. The role of the substrate is analyzed and the thermodynamics and kinetics of thin film growth are illustrated by several examples. Finally, lattice relaxations induced by the electron quantization are discussed.

2.2 The one-dimensional quantum well

The most simple way to describe electron confinement is by the one-dimensional 'infinite quantum well' that can be found in every quantum mechanics textbook and is shown in Fig. 2.1(a). The potential $V(z)$ is zero inside the well ($0 < z < d$) and infinite elsewhere; d is the width of the well. The wave func-
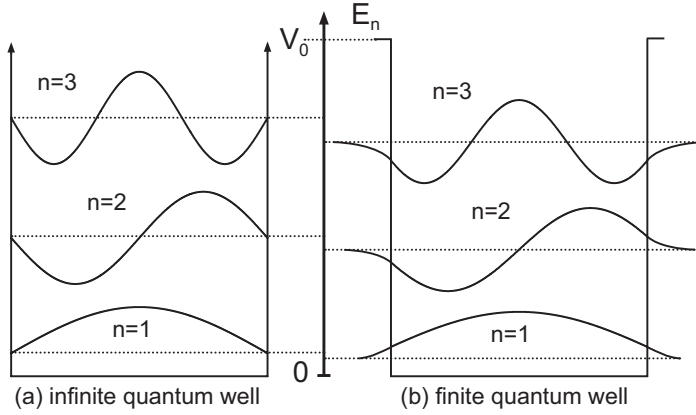
Figure 2.1: Schematic drawing of the wave functions (not normalized) of the first three energy levels in a (a) infinite quantum well and (b) finite quantum well, with n the quantum number of the state.

tions ψ within the well are obtained by solving the the Schrödinger equation with $V(z) = 0$, using the appropriate boundary conditions ($\psi = 0$ at $x = 0, d$). The wave numbers for the allowed states are now:

$$k = \frac{n\pi}{d},\tag{2.1}$$

where n is a positive integer or 'quantum number'. The energy levels are therefore given by

$$E_n = \frac{\hbar^2}{2m}k^2 = \frac{\hbar^2\pi^2n^2}{2md^2},\tag{2.2}$$

with m the free electron mass. The wave functions inside the well are given by:

$$\psi_n(z) = A\sin(\frac{n\pi z}{d}),\tag{2.3}$$

with z the coordinate along the well and A a normalization constant. The cosine term vanishes from the solution, because the wave functions have to be zero at $z = 0$, the left hand side wall. The separation between the levels increases with increasing energy. If d increases, the energy levels and their separation decrease with $1/d^2$.

Infinite potential wells are a theoretical construct and for all practical purposes quantum wells do have finite depth. The potential of the so-called 'finite potential well' is zero inside the well and V_0 on the outside. Elementary quantum mechanics tells us that the solutions of the Schrödinger equation decay exponentially into the classically forbidden region ($z < 0$ and $z > d$). The wave functions of the finite quantum well therefore consist of two parts: the sine (and

cosine) waves inside the quantum well and an exponential tail outside the well. Fig. 2.1(b) shows the wave functions of a finite quantum well. Compared to the infinite well, the kinetic energies (i.e. the energy levels) are slightly lower because the curvatures of the wave functions are slightly lower. The spilling of the wave function into the barriers of the well can mathematically be described by a phase shift ϕ. With this phase shift included, Eq. (2.1) leads to the Bohr-Sommerfeld quantization rule (or phase accumulation model) which describes the energy levels of a finite quantum well:

$$2kd + \phi = 2\pi n, \tag{2.4}$$

with $n = 0, 1, 2, 3, \ldots$ This relationship can also be interpreted as follows: in the scattering picture, the total phase accumulated in a round trip back and forth through the well has to be an integer value of 2π. This total phase accumulation consists of two contributions: the phase collected from travelling twice the width of the box ($2kd$, d is the width of the well) and the total phase shift from reflection at the two walls ϕ.

The phase shift originates from the matching conditions of the wave functions at the boundary of the finite potential well. Since the wave function has to be single-valued, ψ must be continuous across the boundary. Moreover, since V_0 is finite, $\partial\psi/\partial z$ must also be continuous. (Note that $\partial\psi/\partial z$ is discontinuous only in the case of an infinite potential). These matching conditions relate the phase shift to the logarithmic derivative of the wave function at the physical boundary [5]:

$$tan(\frac{\phi_l}{2}) = -\frac{L_l}{k}, \quad tan(\frac{\phi_r}{2}) = \frac{L_r}{k}, \tag{2.5}$$

with the indices l and r for left and right and L the logarithmic derivative of the wave function.

For the infinite well, a vanishing wave function at the location of the wall requires a phase shift of $-\pi$ for each reflection. A phase shift equal to zero, places an antinode at the wall which is unphysical. Because the phase shift equals $-\pi$ for a hard wall potential, the quantum number n in Eq. (2.4) starts from zero. This is in contrast to the conventional picture of Eq. (2.1) where the quantum number starts from one. In this thesis, we will adopt the quantum numbers according to the phase accumulation model.

2.3 The 1D quantum well with a crystal band structure

So far, we have ignored two other important ingredients for understanding quantum size effects in thin metal films, namely the crystal lattice and band structure. The band structure of a free particle ($V = 0$) reduces to the free electron parabola: $E = \hbar^2 k^2/2m$. In a crystal or 'periodic potential', electrons are
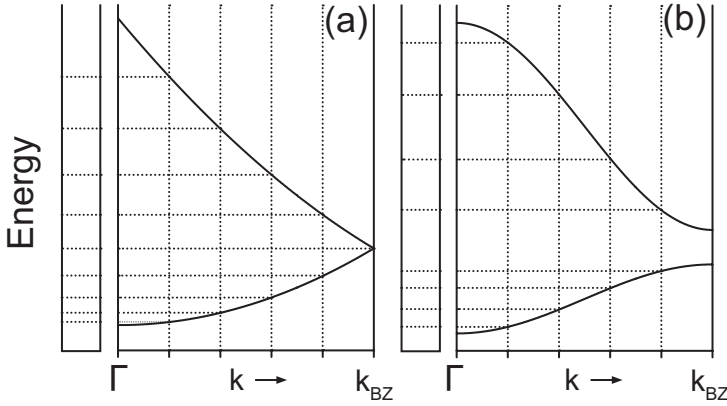
Figure 2.2: Schematic drawing of the energy levels in a quantum well for (a) free electron dispersion and (b) realistic crystal band structure.

no longer represented by free electron plane waves but instead, the wave functions have become Bloch waves. To illustrate the effect of the periodic lattice potential on the quantized energy spectrum of a confined Bloch electron, we first plot the free electron dispersion within the first Brillouin zone (BZ). In this so-called 'empty lattice approximation' [6], the free electron band is backfolded at the Brillouin zone boundary and, assuming hard-wall potential barriers, the size quantization along the z-direction results in a discrete energy spectrum according to Eq. (2.2). The allowed energy eigenvalues are indicated in Fig. 2.2(a). On the other hand, the non-zero Fourier components of the periodic lattice potential open up a gap at the Brillouin zone boundary. Even if the size quantization condition according to Eq. (2.1) remains valid, the resulting energy eigenvalues will be different, as indicated in Fig. 2.2(b). The quantum well energies now follow the band structure of the bulk material, but do not show any dispersion with k_z since their energy only depends on the quantum number n. The separation between the quantum well states becomes smaller near the band edges and larger near the middle of the band.

In thin metal films there is no translation symmetry in the direction normal to the surface (z-direction). The potential in the xy-plane is periodic, while the potential in the z direction represents a quantum well: $V(x, y, z) = V(x, y) + V(z)$. The wave function in the well can therefore be written as the product of two independent functions; a parallel Bloch component $\Phi(x, y)$ and a wave function $\psi(z)$ describing the quantum well behavior in the normal direction:

$$\Psi(x, y, z) = \Phi(x, y)\psi(z). \tag{2.6}$$

With Eq. (2.3) this can be written as:

$$\Psi(x, y, z) = \Phi(x, y) sin(\frac{n_z \pi z}{d}).$$ (2.7)

The energy levels, or 2D subbands rather, are therefore given by:

$$E_n = \frac{\hbar^2}{2m}(k_\parallel^2 + k_\perp^2) = \frac{\hbar^2}{2m}(k_x^2 + k_y^2) + \frac{\hbar^2 \pi^2 n_z^2}{2md^2},$$ (2.8)

where we used the free electron approximation; m is the free electron mass. It follows that, in the free electron approximation, two-dimensional subbands are formed in k-space, which describe the $k_\parallel$-dependence of the quantum well energies. The in-plane dispersion of the quantum well states follows the free electron parabola.

2.4   Boundary conditions

Electrons in a thin metal film on a semiconductor are confined between the vacuum barrier and the potential barrier at the metal-semiconductor interface. The total phase shift ϕ from Eq. (2.4) thus consists of a phase shift at the film-vacuum interface ϕ_B and a phase shift at the film-substrate interface ϕ_C, with $\phi = \phi_B + \phi_C$.

On the vacuum side of the potential well the work function determines the height of the potential barrier. The phase shift at the metal-vacuum interface ϕ_B can be approximated [7, 8] for a $1/r$ image potential by the Wigner-Kramer-Brillouin (WKB) expression:

$$\phi_B(E)/\pi = [3.4/(E_V - E)]^{1/2} - 1,$$ (2.9)

where E_V is the vacuum level (or work function). In the energy region of interest for photoemission spectroscopy (from a few eV binding energy up to the Fermi level) Φ_B is a slowly varying function of energy. With a typical work function of 4 eV, ϕ_B ranges from -0.08π at the Fermi level to -0.39π at 5 eV binding energy.

The conditions for confinement at the metal-substrate interface are less trivial. An electron can only be confined to the film if its energy lies within a band gap of the substrate. However, quantum well states have also been observed in metal-metal systems. Although a metal substrate has a continuous state density in the vicinity of the Fermi level, these states do have definite momentum. If there are no matching momentum states in the film and the substrate, one usually speaks of a 'relative gap' [9]. Coupling between the film and the substrate states can also be disallowed based on symmetry grounds. This situation is called a 'symmetry gap' [10]. For instance, sp derived states in the film do not mix with d-states in the substrate.

A nice example of a relative gap can be found at the Ag(111)-Au(111) interface [9]. At the Fermi level both metals have a gap in the <111> direction
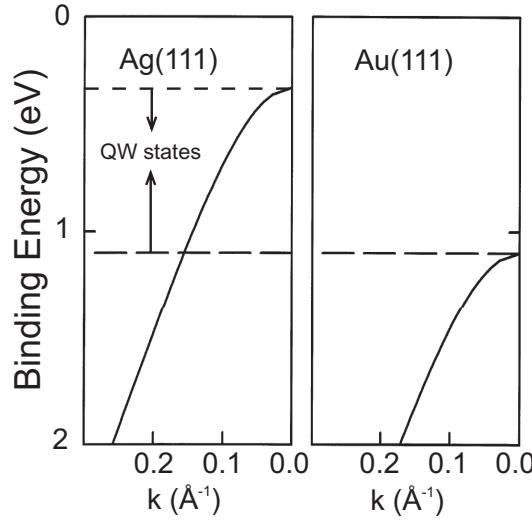
Figure 2.3: Schematic drawing of the band structure of Ag(111) and Au(111). In between the dashed lines quantum well states can exits in Ag films on Au(111). Figure from T. -C. Chiang [9].

as shown in Fig. 2.3. The top of the sp band is at 1.1 eV binding energy for Au(111) compared to 0.3 eV for Ag(111). Au grows in the (111) direction on Ag(111) and vice versa. Growth of Au on Ag(111) does not give rise to quantized states in the Au film. All the sp-states in the Au film at 1.1 eV binding energy or lower can couple to sp-like Ag bulk states. However, in Ag growth on Au(111) the Ag sp-states between 0.3 and 1.1 eV binding energy do not have any substrate states to couple with and remain therefore confined in the film. Below 1.1 eV binding energy coupling does take place. Confinement only occurs in an energy window where there are no substrate states available of suitable momentum or symmetry.

2.5   QSE oscillations in physical properties

The first experimental evidence for quantum size effects in thin metal films were the electron tunneling experiments of Jaklevic et al. [11] in 1971 who showed directly the existence of electron standing waves in thin Pb films. This discovery lead to an increased attention for quantization effects in thin films. Early theoretical calculations on the QSE were performed by F.K. Schulte [12] in 1976 who calculated the properties of free standing thin metal films self-consistently. The framework for the calculations was the density functional theory (DFT) developed by Lang and Kohn [13, 14] in 1970 in their theory
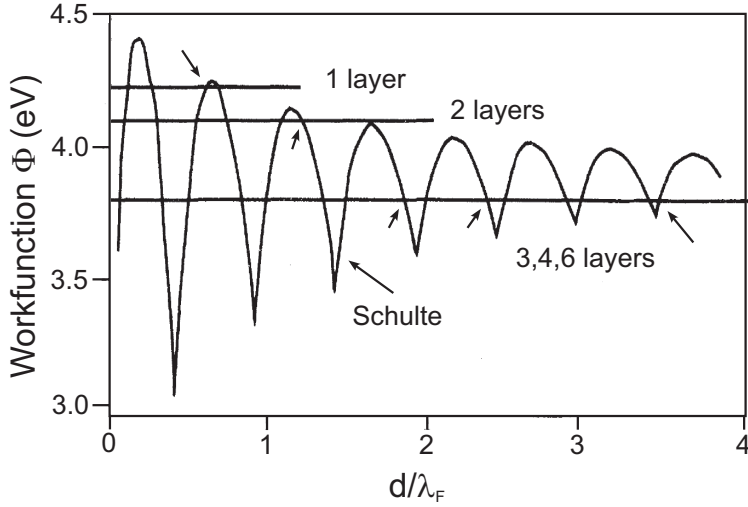
Figure 2.4: Work function as a function of film thickness (in terms of λ_F. The cusp-like curve displays the jellium calculations of Schulte [12] while the horizontal lines indicate the calculated values of ϕ for N-layer Al(111) films, N=1-4,6. The locations of the intersections are roughly at d/λ_F = 0.6, 1.2, 1.9, 2.4 and 3.5. Figure from Feibelman [15]

of metal surfaces. Schulte showed that for jellium slabs electron densities, potentials and work functions all oscillate as a function of the film thickness with a period of half the Fermi wavelength. The relationship between these properties and the QSE is established in the paper, although band structure and crystal lattice were not included.

In the jellium calculations of Schulte [12], the thickness of the slab (i.e. the width of the positive background) can be adjusted in infinitesimal steps. In reality however, the positive charge is located at the ion cores and increments of the slab thickness have to be in units of a monolayer. In his DFT calculations, Feibelman [15] included the lattice and calculated surface energy and work functions for Al(111) and Mg(0001) slabs. The influence of a substrate was not included in this paper. Now the positive charge is no longer smeared out but is located at the ion cores; the ions are allowed to relax from the bulk positions to screen the electron density at the surface. The results of the calculations with relaxed atomic positions are shown in Fig. 2.4. The image shows the cusp-like work function development of Schulte's calculations together with the calculation for relaxed Al(111) film of Feibelman [15]. It can be seen directly that Feibelman's work functions sample Schulte's work functions at discrete layer thickness. Notice that there would not be any oscillation if the interlayer spacing d were exaclty equal to $\lambda_F/2$.

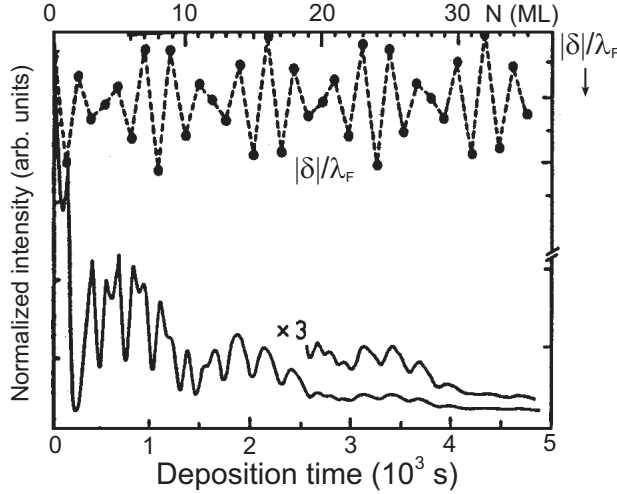Further experimental evidence of QSE oscillations was given by Jalochowski

Figure 2.5: Bottom: Intensity oscillations of the specular He beam during Pb deposition on Cu(111) at 140 K. Top: The corresponding coverage dependence of the misfit δ. Figure from Hinch et al. [17]

and Bauer [16] for Pb on Si(111). They observed QSE oscillations in the electrical resistivity and in the Reflection High Energy Electron Diffraction (RHEED) specular spot intensity during growth. Monolayer oscillations indicating layer-by-layer growth were modulated by an oscillation with a greater periodicity due to the QSE. The periodicity of the modulation is directly related to the mismatch between the lattice parameter and the half Fermi wavelength of Pb. A similar relationship was also found in He atom scattering experiments of Pb on Cu(111) by Hinch et al. [17] The bottom curve of Fig. 2.5 shows the normalized specular intensity in He scattering as a function of deposition time (coverage). The coverage scale in ML is indicated at the top. It can be clearly seen that monolayer oscillations are modulated with a bilayer periodicity. A weaker modulation or 'envelope function' of much longer wavelength can also be discerned. For Pb(111) the lattice parameter d_0 and the Fermi wavelength obey $2d_0 \approx 3\frac{\lambda_F}{2}$, $d_0 = 2.85$ Åand $\lambda_F = 3.95$ Å. Every bilayer of Pb can approximately support three half Fermi wavelengths, causing the observed bilayer oscillations. The misfit $\delta = |Nd_0 - n\frac{\lambda_F}{2}|$ is shown at the top of this figure, with d_0 the Pb(111) lattice parameter and N, n integers. The similarity between the long wavelength modulation in the He scattering data and the period of δ is striking. The nodes of the envelope function are visible at 1400, 2600 and 3800 seconds deposition, corresponding to 11, 20 and 29 ML. The bilayer oscillations correspond to $2d_0 \approx 3\frac{\lambda_F}{2}$, while the long wavelength modulation reflects the mismatch between d_0 and λ_F. The authors also showed that for Pb

growth on Pb(111) monolayer oscillations are found without any bilayer or long
wavelength modulation, since there is no quantum confinement in homoepitax-
ial growth. This shows that the observed oscillations are indeed the result of
quantization effects.

2.6   Preferred heights and stability

Another result of the jellium model of Schulte [12] is the thickness dependent
free energy of the film: the free energy increases as the confinement gets
stronger (energy levels are pushed upward). However, there is another contri-
bution to the free energy of the film when the substrate is included. The tailing
of the wave functions into the substrate (charge spilling) produces an interface
dipole which also contributes to the total energy. These two effects, i.e. quan-
tum confinement and charge spilling, are the major contributions to the free
energy of the film and they are the key ingredients of the 'electronic growth'
model [18].

The free energy has direct consequences for the stability of the film. Since
the free energy is an extensive property, one would normally expect the energy
to be a linear function of the thickness d. However, in the quantum regime,
the oscillatory character of the total free energy (with contributions from the
electronic energy levels and interfacial dipole) can cause $E(d)$ to be less trivial.
When $\partial E/\partial d = 0$ and $\partial^2 E/\partial d^2 > 0$ (Fig. 2.6(a)), one should expect a film of
thickness d to be particularly stable and prevalent. This behavior is similar to
the existence of magic numbers for metal nanoclusters [19]. Fig. 2.6(b) shows
the $E(d)$ curve for an unstable film of thickness d_2. Since $E(d_2)$ is a maximum
of the free energy curve, the total free energy can be lowered by a phase sep-
aration of the film, since $\alpha E(d_a) + (1 - \alpha)E(d_b) < E(d_2)$, with $d_a < d_2 < d_b$. The
unstable films are expected to phase separate into multiple-height islands of
stable thickness, provided that the temperature is high enough to allow suffi-
cient surface diffusion. One can furthermore define a 'critical thickness', d_c, for
smooth film growth if the film is stable for $d > d_c$ and unstable for $d < d_c$. An
X-ray study [20] shows evidence for a critical thickness of approximately five
monolayers in the Pb/Si(111)7×7 system.

The 'electronic growth' model was developed following an experimental
study of Ag on GaAs(110) [21]. After deposition of less than 7 ML of Ag,
followed by a mild annealing step, atomically flat Ag films with 7 ML deep
holes had been observed, i.e., the deposit had 'phase separated' into regions
of 0 ML and 7 ML thick. Similar behavior has been observed in Ag/Si(111)
and Pb/Si(111) [2]. Scanning tunneling microscopy (STM) [22] and spot pro-
file analysis - low energy electron diffraction (SPA-LEED) [2] measurements of
Pb/Si(111) showed islands with flat tops, steep edges, and strongly preferred
heights. An STM image with the histogram of observed heights is shown in
Fig. 2.7 and shows predominantly 7 ML height islands.

Later, it was shown that these preferred heights depend on the Schottky
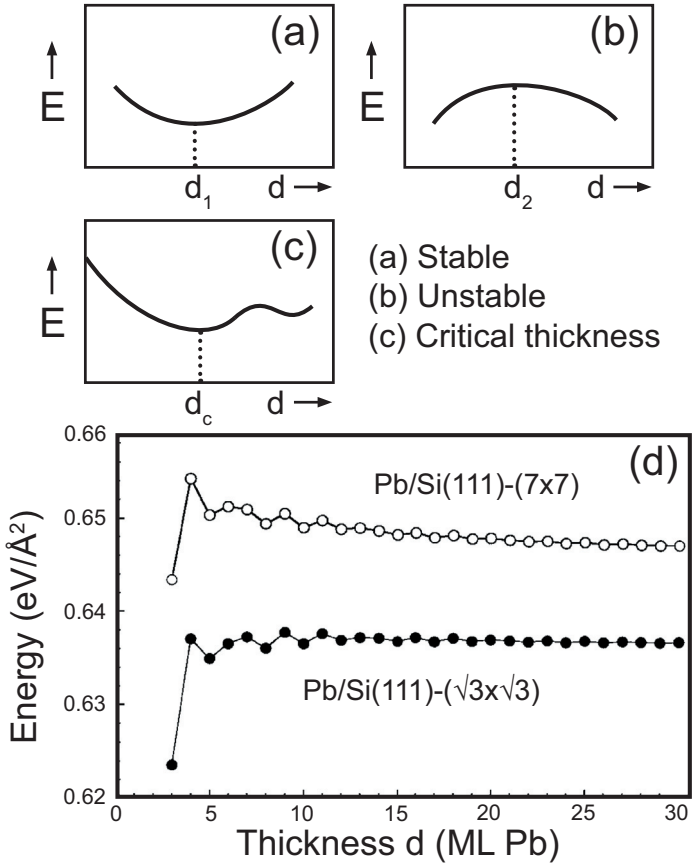
Figure 2.6: (a)-(b) Schematic drawings of the free energy E as a function of thickness d for stable (d_1) and unstable (d_2) configurations. (c) Schematic drawing of a critical thickness, for $d < d_c$ no smooth film growth is allowed. (d) Calculated $E(d)$ curves with the electronic growth model of ref. [18] for Pb on Si(111)7×7 (upper curve) and Pb on Si(111) $\sqrt{3} \times \sqrt{3}$ (lower curve). Fig. (c) from Yeh et al. [2].
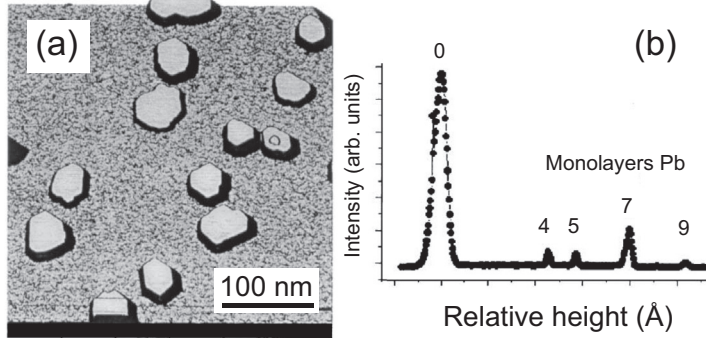
Figure 2.7: (a) STM image of Pb islands on Si(111). The coverage is 3.2 ML. (b) The relative occurrence of the height of the islands in the image of (a). Figure from Su et al. [22]

barrier height (SBH) at the Si/Pb interface [2]. The preferred thickness changes from 7 to 5 ML on changing the substrate from Si(111)7×7 to Si(111) $\sqrt{3} \times \sqrt{3}$-Pb. The first substrate has a SBH of 0.70 eV while the latter has a SBH of 0.93 eV [23]. These results show that there is a link between the boundary conditions and the stability of the film or island.

Fig. 2.6(d) shows the calculated $E(d)$ curves for Pb/Si(111)7×7 and Pb/Si(111) $\sqrt{3} \times \sqrt{3}$, according to the electronic growth model, after subtracting a term linear in the film thickness. The experimentally determined preferred heights are 7 and 5 ML, respectively. The minimum at 5 ML in the lower curve is reproduced by the calculations, but the calculated free energy at 7 ML in the upper curve only is a local minimum. So, the model appears too simplistic to quantitatively reproduce the observed global energy minima of the metal films.

Total energy calculations within the framework of Density Functional Theory (DFT) should be much more accurate but these often cannot include the (usually) incommensurate substrate. Further complications arise from the fact that the structure of the interfacial wetting layer is usually disordered or totally unknown. The Sb/GaAs(110) system [24] is almost commensurate and has been studied with DFT, but the theoretical results have never been verified experimentally.

For all experimental results there appears to be a 'temperature window' in which preferred heights are observed. If the temperature is too low, the adatom mobility is not high enough to smoothen the film. If the temperature is too high, the film will ultimately acquire its thermodynamic equilibrium morphology which, in hetero-epitaxy, implies Stranski-Krastanov growth. From a thermodynamic perspective, flat films or complete wetting can only be realized

when:

$$\gamma_S \geq \gamma_F + \gamma_I \qquad (2.10)$$

with γ_S, γ_F and γ_I the free energies per unit area of the substrate, film and inter-face, respectively. For layer-by-layer growth, this condition has to be satisfied for each new layer. Due to the lattice mismatch in hetero-epitaxy, the interface free energy increases with thickness due to lattice strain and the film will break up into islands at the so-called critical thickness. Note that critical thickness has an entirely different meaning in electronic growth. Critical thickness in the context of electronic growth is the thickness above which flat film growth becomes possible (7 ML for Ag/GaAs(110)). The electronic growth regime for Pb is typically between 150 K and 250 K. Above room temperature, Pb films usually grow in the Stranski-Krastanov mode, which is the true thermodynamic ground state.

So far, we have mainly discussed the formation of flat-top islands. The link between morphological stability and quantum well electronic structure was demonstrated unequivocally in a nice experiment performed by Luh et al. [25]. These authors tested the stability of Ag films on Fe(001) as a function of thickness. By looking at the quantum well states in photoemission spectroscopy they could exactly probe the number of atomic layers of Ag present on the substrate. Upon annealing a film with N atomic layers grown at low temperature (100 K), the film started to bifurcate around 400 K into films with thickness N+1 and N-1. The data are displayed in Fig. 2.8(a). Most films bifurcated around 400 K whereas the film with N=5 was stable up to over 800 K (the 1 and 2 ML films are not taken into account). The temperature at which the bifurcation starts is a measure for the stability of the film. So the 5 ML film is the most stable configuration of the system. The authors of this paper [25] evaluate the total energy of the film by integrating the energy of all valence electrons. In this sum all electrons in the 2D subbands (see Eq. (2.8)) with fixed k_z but with free-electron-like k_x and k_y up to the Fermi level give a non-zero contribution. Fig. 2.8(b) shows the calculated energy difference against bifurcation, defined as:

$$\Delta(N) = \frac{1}{2}[E(N+1) + E(N-1)] - E(N), \qquad (2.11)$$

with $E(N)$ the free energy of thickness N, giving a maximum at the 5 ML thickness. When the summation over k_x and k_y is omitted, the total energy minima are located at the same thickness, as can be seen in Fig 2.8(c). Thus, a summation of the occupied quantum well energies for $k_x = k_y = 0$ gives a good indication of the thickness dependent stability.

In this simple picture of only adding up the quantum well energies, the explanation for the increased stability of the 5 ML film is rather straightforward. As the thickness of the film increases, all quantum well states shift to higher binding energy (Eq. (2.2)). The 4 to 5 ML increment is the only single layer increment that does not produce new subbands below the Fermi level. The $k = 0$ states that are filled in the 5 ML film were already filled in the 4 ML film,
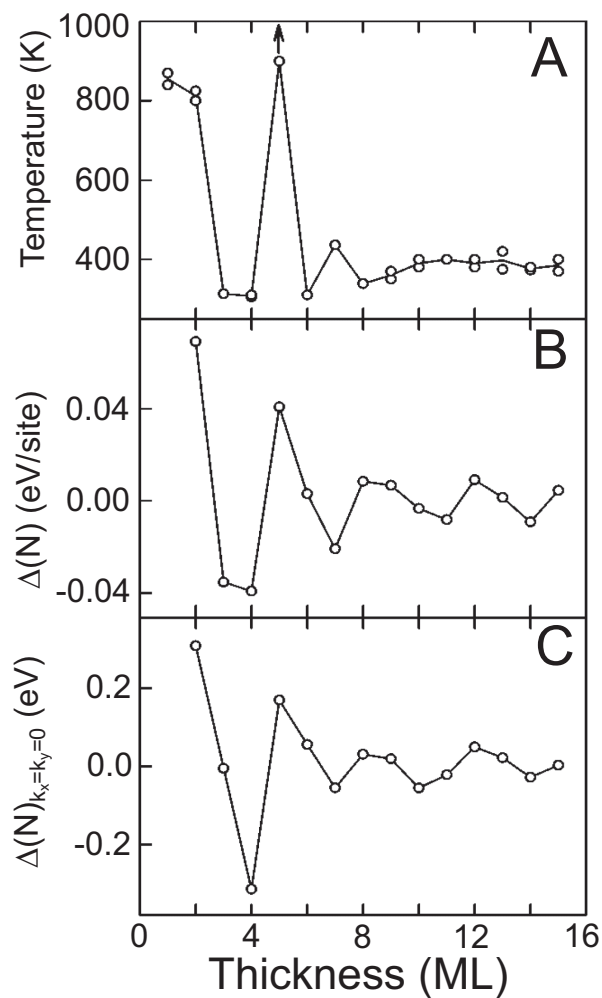
Figure 2.8: (A) Bifurcation temperature versus layer thickness N for Ag on Fe(001). (B) Calculated energy difference $\Delta(N)$ against bifurcation as a function of N. (C) Same as (B) but without the summation over k_x and k_y. Figure from Luh et al. [25]
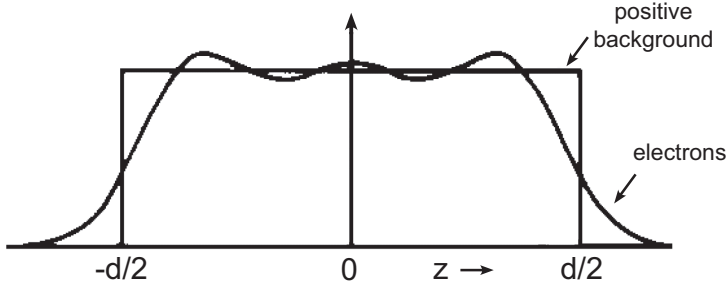
Figure 2.9: Electron density and uniform positive background with width d from the jellium calculations of F.K. Schulte. The electron density shows an oscillation with wavelength $\lambda_F/2$. Figure from F.K. Schulte [12].

but all of them have shifted toward higher binding energy. Therefore the total energy of the 5 ML film must be lower than that of the 4 ML film. All other single layer increments result in the filling of a hitherto unfilled subband and do not result in an obvious lowering of the total energy of the film.

2.7   Surface relaxation: theory

In the previous sections we analyzed the electronic structure and stability of quantum confined thin films. In this section we focus on the implications of the altered electronic structure for the atom positions. The force balance between the ion cores and valence electrons, which determines the crystal structure of the bulk, is different for the thin film geometry. There are two reasons for this: first, the presence of two nearby interfaces and second, the quantization of the electronic structure.

The jellium model is a good starting point for our discussion of lattice relations near a surface or interface. This model treats the positive charge present in the solid as a uniform positive background. Electrons that are moving in this constant background potential are treated using the density functional formalism [26]. Numerical results by F.K. Schulte [12] show that the electron density oscillates with a period of half the Fermi wavelength. The amplitude of the oscillation is strongest at the surface and attenuates towards the interior of the film. Fig. 2.9 from Schulte shows the uniform positive background together with the electron density. The damped oscillation of the electron density, often called 'Friedel oscillation', can be clearly observed. Thus, a step potential gives rise to oscillations in the electron density with a period of $\lambda_F/2$.

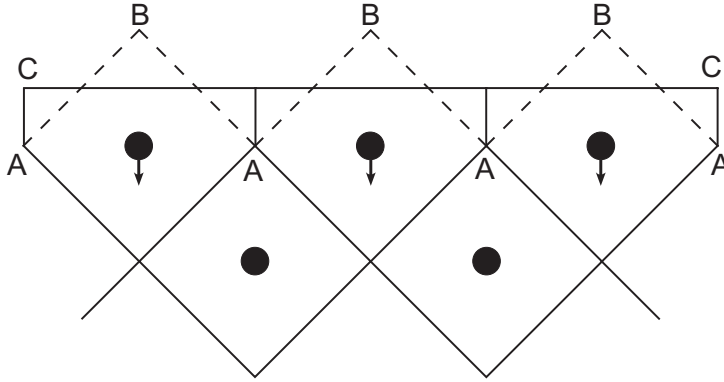We now turn to a model, developed by Finnis and Heine [27], that uses

Figure 2.10: Wigner-Seitz cells at the (110) surface of a simple cubic crystal. The surface layer contracts as indicated by the arrows. Figure from Finnis and Heine [27].

elementary concepts to understand lattice relaxations surfaces of metals. Fig. 2.10 shows the Wigner-Seitz cells at the (110) surface of a simple cubic metal. Each cell contains one atom. The $ABAB\ldots$ dotted line represents the bulk truncated electron density. The work of Smoluchowski [28] showed that the CC line is a much more realistic approximation of the electron density at the surface. The electrons from the corrugated $ABAB\ldots$ structure smear out toward the CC line, which is called 'Smoluchowski charge smoothening' of charge on surfaces. If we assume that the position of the ion core is determined by the electrostatic forces within the corresponding Wigner-Seitz cell, then we see immediately that the center of gravity of the Wigner-Seitz cell provides the coordinates of the ion core. Since the Smoluchowski smoothening moves the center of gravity in the topmost Wigner-Seitz cells in Fig. 2.10 toward the interior bulk, and accordingly, the Finnis-Heine model predicts a contraction of the first interlayer spacing d_{12}. Using the Finnis-Heine model, calculated contractions of the Al(111), Al(100) and Al(110) surfaces are -1.6%, -4.6%, and -16%, respectively. The more open surfaces (i.e., surfaces with fewer atoms per unit area) experience more Smoluchowski smoothening and, consequently, exhibit a greater contraction of the first interlayer spacing. Indeed, the open (110) surface shows a much larger relaxation than the closed-packed (111) surface.

The Finnis-Heine model does not interfere with the aforementioned Friedel charge density oscillation; they can be regarded as two complementary phenomena. In the Finnis-Heine model the charge transfer has a great in-plane component, while the Friedel oscillation only represents charge density oscillations perpendicular to the surface. Friedel oscillations suggest the possibility of oscillatory interlayer relaxations [29, 24], whereas the Finnis-Heine model only considers the first interlayer spacing. It is not obvious whether the Friedel
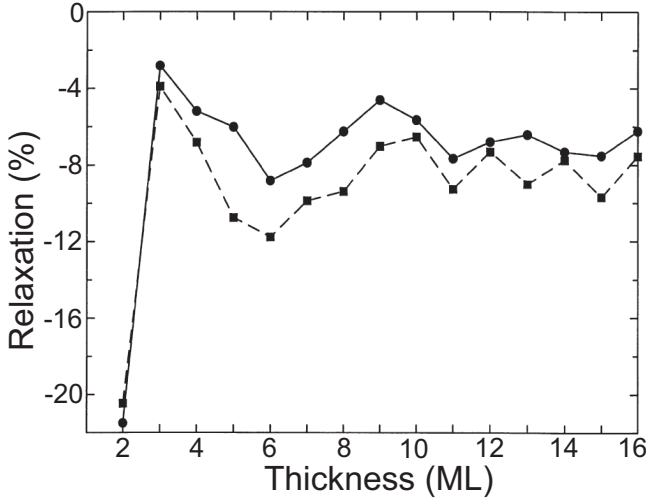
Figure 2.11: Deviation of the first interlayer spacing of Al(110) slabs from the bulk value as function of slab thickness. The squares and dots represent bulk lattice constants of 3.98 and 3.962 Å, respectively. Figure from Kiejna et al. [31]

oscillations or jellium oscillations persist when the uniform positive background is replaced by discrete core potentials. In particular, the relaxation of the core positions is expected to screen these density oscillations. Recent DFT calculations, nonetheless, show that Friedel oscillations in ultrathin Pb films are strong [30].

The other contribution to the multilayer relaxation in quantum confined films originates from the quantized electronic states. The normal component of the electron's wave number k_z is quantized which affects the electron density and force balance between electrons and ion cores. Therefore, multilayer relaxations are expected to be altered by the quantum size effect. Because the electronic structure is very much dependent on the thickness of the film, the multilayer relaxations are also expected to be thickness dependent. Upon increasing the film thickness, the multilayer relaxations should converge to their bulk values.

Kiejna et al. [31] calculated the first interlayer spacing of Al(110) slabs as a function of slab thickness for two different in-plane lattice parameters. Their results are shown in Fig. 2.11. The significant variation in interlayer spacing converging to a certain bulk value can be seen in the image. The quantum size effect on layer relaxations persist for up to 16 layer thick slabs. The value obtained for the thickest slabs agrees very well with the experimental value [32, 33] of -8.5% at the surface of a bulk crystal.

An attempt to include the substrate in calculations of the oscillatory lattice

Table 2.1: Calculated interlayer spacings (in Å) for Sb overlayers on GaAs(110). d_{01} is at the substrate-film interface. Table from Cho et al. [24]

	d_{01}	d_{12}	d_{23}	d_{34}	d_{45}	d_{56}	d_{67}
1 ML	2.39						
2 ML	2.54	2.94					
3 ML	2.41	3.44	2.77				
4 ML	2.44	3.28	2.99	2.88			
5 ML	2.43	3.25	2.86	3.16	2.79		
6 ML	2.44	3.28	2.87	2.97	3.02	2.81	
7 ML	2.43	3.24	2.89	3.00	2.94	3.08	2.81

relaxation phenomenon has been made by Cho et al. [24] who performed first-principles calculations of Sb films on GaAs(110) up to 7 ML film thickness. This system shows a very small lattice mismatch and therefore the substrate can be included in the calculations without the need for extreme computing power. Their results are listed in Table 2.1 and reveal very large oscillations of the interlayer spacings. Deviations from the bulk value can amount to as much as 15 percent. The oscillatory behavior can be most clearly seen in the interlayer spacings near the film-vacuum and film-substrate interface.

2.8   Surface relaxation: experiments

Experimental data for the layer relaxations in quantum-confined thin films come from STM studies [22], Helium atom scattering (HAS) [34, 35] and X-ray diffraction [35, 36]. The STM and He scattering methods actually do not measure the positions of ion cores directly, but probe the spilling electron densities above the surface. The measured step heights are therefore often called 'apparent' step heights. The results of Su et al. [22] for 7 ML high Pb islands on Si(111), however, show a decrease of the first and an increase of the second interlayer spacing on odd-layer islands, which is independent of the tip voltage. This indicates that the measured oscillations in interlayer spacing do have a contribution from the ion cores. In He scattering experiments [34] of Pb films on Ge(001) extremely large lattice relaxations are claimed, but the large values must be attributed to electronic effects.

X-ray scattering experiments from Pb on Ge(001) [35] and Pb on Si(111) [36] both show contraction of 5% in the first interlayer spacing of the Pb film. The authors of ref. [36] show a quasibilayer variation in the interlayer spacings of the films by an extra diffraction peak in the spectra, showing double layer periodicity that can be related to quantization effects.

In all of these experiments, layer relaxations have not been investigated systematically as a function of Pb coverage. The challenge now is to proof the

existence of thickness dependent multilayer relaxations. A suitable experimental technique to measure the positions of the ion cores in thin films is quantitative low energy electron diffraction (QLEED or LEED–I(V)). The energy of the electrons involved in the LEED experiment (30-500 eV) makes this technique most sensitive to deep electron shells. Unlike HAS or STM, LEED is not sensitive to the charge density near the Fermi level. LEED I(V) is described in detail in Chapter 4.

2.9 Photoemission from Quantum Well States

Angle resolved photoemission spectroscopy (ARPES) is a very suitable technique for observing quantum well states in thin films [9, 10]. In the photoemission experiment, photons with energy $h\nu$ impinge on a sample, and photoexcited electrons are emitted from the solid. The electrons that gain enough energy to exit the solid can be measured with an electron energy analyzer. The kinetic energy E_k of the excited electrons is given by

$$E_k = h\nu - E_b - \Phi_a, \tag{2.12}$$

with E_b the binding energy of the electron's initial state, measured with respect to the Fermi level, and Φ_a the analyzer work function. Because of the translation invariance parallel to the surface, the parallel momentum $\mathbf{k}_\parallel$ can be obtained from

$$\hbar\mathbf{k}_\parallel = \sqrt{2mE_k}\,sin\theta, \tag{2.13}$$

with m the electron rest mass and θ the angle between the detector and the surface normal. By making use of the tunable parameters $h\nu$ and θ the electronic structure $E(\mathbf{k})$ can be investigated.

Photoemission from quantum well states adds some very interesting features to the technique. Because the normal component of the wave vector is usually not conserved during the photoemission process, it is often impossible to probe the full 3D band structure with ARPES. However, due to quantum confinement the allowed values for k_z are perfectly known. This allows for the direct determination of the band structure $k_z(E)$ $(= E(k_z)$) in the direction normal to the surface and from this relationship the total phase shift $\phi_B + \phi_C$ can be obtained. The procedure goes as follows: we first select a pair of quantum well states with identical binding energy. Each of these states corresponds to a different film thickness [38]. The phase accumulation model of (Eq. (2.4)) holds for both states:

$$2k_z d_1 + \phi(E) = 2\pi n_1 \tag{2.14}$$
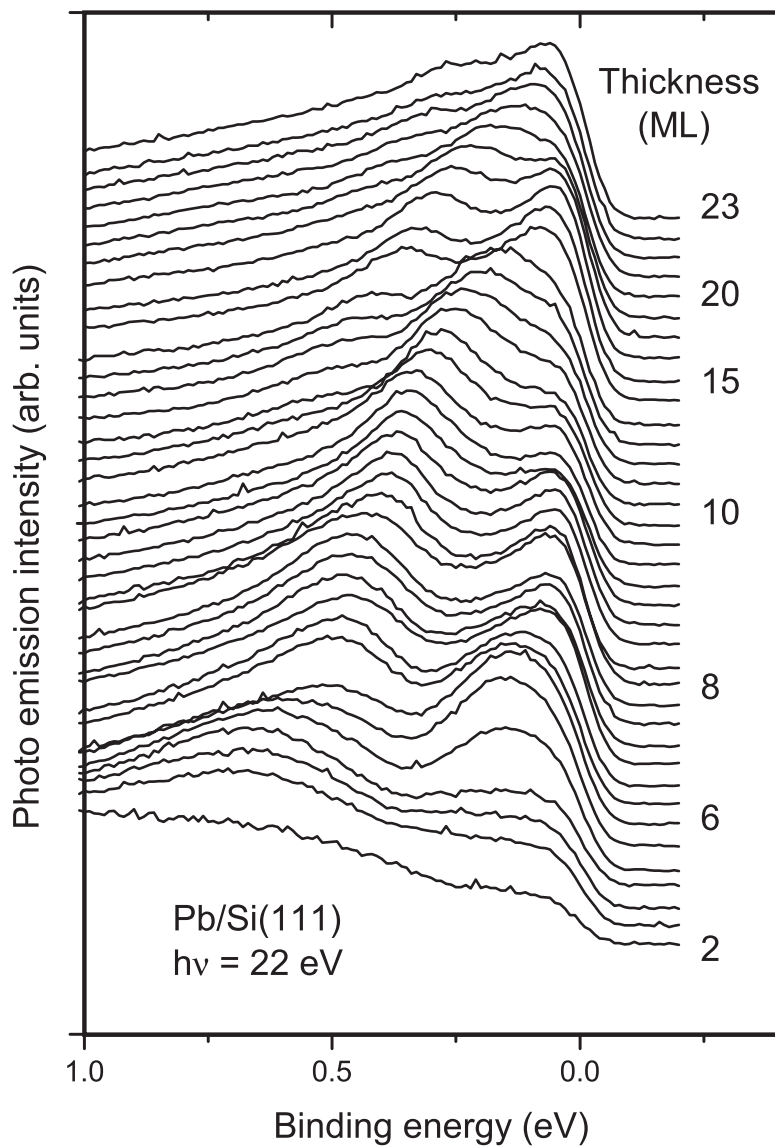
and

$$2k_z d_2 + \phi(E) = 2\pi n_2, \tag{2.15}$$

Figure 2.12: Normal-emission photoemission spectra of Pb on Si(111)7×7. The coverage ranges from 2 to 23 ML [37].

where the indices 1 and 2 refer to the two different film thicknesses. Because the binding energies are equal, the phase shift should also be identical. Subtraction of these two equations gives:

$$k_z = \pi(n_2 - n_1)/(d_2 - d_1), \qquad\qquad (2.16)$$

This value for $k_z(E)$ gives the phase accumulation model value for the total phase shift at binding energy E: $\phi(E) = \phi_B(E) + \phi_C(E)$.

Fig. 2.12 provides an example of photoemission spectra from a quantum confined thin film. The spectra are recorded from Pb films [37] on Si(111)7×7 at 110 K. The signature of the quantum well states is evident from the binding energy shift of the peaks with increasing Pb coverage. As is the case in electron diffraction, photoemission spectra are averaged over the photon spot size on the sample. Therefore, photoemission spectroscopy can only provide layer resolved information when the film coverage is atomically smooth over the entire spot area. Multiple thicknesses or rough growth fronts make the analysis of the spectra more difficult. Fortunately, near-perfect film growth is possible due to the strong self organization of the Pb deposit. Self organization greatly facilitates the analysis of both photoemission spectra and LEED I(V) spectra, thereby allowing for a fundamental study of the quantum size effect and the structural and morphological evolution of the films, which is the core topic of this thesis.

Bibliography

[1] K. Budde, E. Abram, V. Yeh, and M. C. Tringides, Phys. Rev. B **61**, R10602 (2000).

[2] V. Yeh *et al.*, Phys. Rev. Lett. **85**, 5158 (2000).

[3] G. A. Farnan *et al.*, Phys. Rev. Lett. **91**, 226106 (2003).

[4] F. J. Himpsel, J. E. Ortega, G. J. Mankey, and R. F. Willis, Adv. Phys. **47**, 511 (1998).

[5] N. V. Smith, N. B. Brookes, Y. Chang, and P. D. Johnson, Phys. Rev. B **49**, 332 (1994).

[6] C. Kittel, *Introduction to Solid State Physics, 6th edition* (Wiley, New York, 1986).

[7] E. G. McRae, Rev. Mod. Phys. **51**, 541 (1979).

[8] E. G. McRae and M. L. Kane, Surf. Sci. **108**, 435 (1981).

[9] T. -C. Chiang, Surf. Sci. Rep. **39**, 181 (2000).

[10] M. Milun, P. Pervan, and D. P. Woodruff, Rep. Prog. Phys. **65**, 99 (2002).

[11] R. C. Jaklevic, J. Lambe, M. Mikkor, and W. C. Vassell, Phys. Rev. Lett. **26**, 88 (1971).

[12] F. K. Schulte, Surf. Sci **55**, 427 (1976).

[13] N. D. Lang and W. Kohn, Phys. Rev. B **1**, 4555 (1970).

[14] N. D. Lang and W. Kohn, Phys. Rev. B **3**, 1215 (1971).

[15] P. J. Feibelman, Phys. Rev. B **27**, 1991 (1983).

[16] M. Jalochowski and E. Bauer, Phys. Rev. B **38**, 5272 (1988).

[17] B. J. Hinch, C. Koziol, J. P. Toennies, and G. Zhang, Europhys. Lett. **10**, 341 (1989).

[18] Z. Y. Zhang, Q. Niu, and C. K. Shih, Phys. Rev. Lett. **80**, 5381 (1998).

[19] W. D. Knight *et al.*, Phys. Rev. Lett. **52**, 2141 (1984).

[20] K. A. Edwards *et al.*, Surf. Sci. **424**, 169 (1999).

[21] A. R. Smith, K. J. Chao, Q. Niu, and C. K. Shih, Science **273**, 226 (1996).

[22] W. B. Su *et al.*, Phys. Rev. Lett. **86**, 5116 (2001).

[23] D. R. Heslinga *et al.*, Phys. Rev. Lett. **64**, 1589 (1990).

[24] J. H. Cho, Q. Niu, and Z. Zhang, Phys. Rev. Lett. **80**, 3582 (1998).

[25] D. A. Luh *et al.*, Science **292**, 1131 (2001).

[26] W. Kohn and L. J. Sham, Phys. Rev. **140**, A1133 (1965).

[27] M. W. Finnis and V. Heine, J. Phys. F **4**, L37 (1974).

[28] R. Smoluchowski, Phys. Rev. **60**, 661 (1941).

[29] J. H. Cho, Ismail, Z. Y. Zhang, and E. W. Plummer, Phys. Rev. B **59**, 1677 (1999).

[30] M. M. Özer *et al.*, Phys. Rev. Lett. submitted .

[31] A. Kiejna, J. Peisert, and P. Scharoch, Surf. Sci. **432**, 54 (1999).

[32] J. N. Andersen, H. B. Nielsen, L. Petersen, and D. L. Adams, J. Phys. C **17**, 173 (1984).

[33] J. R. Noonan and H. L. Davis, Phys. Rev. B **29**, 4349 (1984).

[34] A. Crottini *et al.*, Phys. Rev. Lett. **79**, 1527 (1997).

[35] L. Floreano *et al.*, Prog. Surf. Sci. **72**, 135 (2003).

[36] P. Czoschke, H. Hong, L. Basile, and T. -C. Chiang, Phys. Rev. Lett. **91**, 226801 (2003).

[37] A. Mans, J. H. Dil, A. R. H. F. Ettema, and H. H. Weitering, Phys. Rev. B **66**, 195410 (2002).

[38] S. A. Lindgren and L. Walldén, Phys. Rev. Lett. **61**, 2894 (1988).

Chapter 3

Electronic structure of Pb films on Si(111)7×7

3.1   Introduction

To understand the role of the Quantum Size Effect (QSE) on the structure and growth of thin Pb film nanostructures, we performed a combined angle–resolved photoemission spectroscopy (ARPES) and low energy electron diffraction (LEED) study of ultrathin Pb films grown on Si(111)7×7. The photoemission results will be presented and analyzed in the present Chapter while the LEED studies will be presented in Chapter 5.

The quantized electronic states in the Pb/Si(111)7×7 system have been investigated as a function of layer thickness by angle–resolved photoemission spectroscopy. Photoemission is a suitable technique to probe quantum well states directly. Normal emission data at fixed photon energy show quantum well states dispersing to lower binding energy as the film thickness increases. The Bohr-Sommerfeld phase accumulation model very well reproduces this behavior and furthermore yields the interfacial phase shift parameter as a function of energy. Normal emission data at different photon energies reveal strong matrix element effects for photo-ionization. Angle-dependent photoemission data reveal a large in-plane effective mass for states that are close to the Fermi energy. These experimental results have been analyzed in detail and their implications for growth and stability will be discussed in the context of recent Scanning Tunneling Microscopy (STM) studies [1, 2].

3.2　Experimental setup

3.2.1　General

The experiments were performed at beamline BL33 of the MaxLab synchrotron radiation facility in Lund, Sweden [3]. The base pressure of the Ultra High Vacuum (UHV) chamber was 3×10^{-11} mbar. The photon energies were $\geq$ 22 eV because otherwise second order light from the monochromator would produce spurious features in the photoemission spectra. An n-type silicon sample was cleaned by flashing to 1375 K by resistive heating. After cooling to room temperature the sample showed a sharp 7×7 LEED pattern and photoemission spectroscopy showed no traces of contamination. The sample was subsequently cooled by a liquid-nitrogen cold finger to 110 K. Pb was evaporated from a Knudsen cell at a source temperature of 870 K which resulted in an evaporation rate of 0.11 monolayer (ML) per minute. The growth temperature of 110 K appeared low enough to prevent the presence of preferred (magic) island heights. Pb grows in the (111) orientation on Si(111)7×7 and therefore the film thickness is given in units of a Pb(111) monolayer (1 ML = 9.43×10^{14} atoms/cm^2).

3.2.2　Calibration procedure

The Pb evaporation rate was calibrated from the known evolution of the Schottky barrier as a function of deposition time and from the ratio of the Pb5d/Si2p photoemission line intensities as a function of coverage [4]. This intensity ratio abruptly saturates at the absolute coverage of 0.65 ML, which was independently checked with Rutherford Backscattering Spectrometry (RBS). The development of the Schottky barrier is complete at a coverage of 0.8 x 0.65 ML = 0.52 ML [4]. Fig. 3.1 shows the shift of the Si2p core level as a function of evaporation time, representing the development of the Schottky barrier. This calibration was consistent with the readings of our quartz crystal oscillator. In the LEED experiments of Chapter 5, Auger Electron Spectroscopy (AES) was used instead to calibrate the evaporation rate. In the AES experiment, the Si LVV line at 92 eV and the Pb NOO line at 96 eV cannot be resolved and are observed as a single peak in the spectrum. Upon Pb deposition, the peak-to-peak intensity of the combined Si-Pb peak decreases and saturates at a Pb coverage of 0.65 ML, which was also checked with RBS.

3.3　Results and discussion

3.3.1　Photoemission from quantum well states

A series of photoemission spectra of Pb on Si(111)7×7 at 110 K is shown in Fig. 3.2. The spectra were recorded at normal emission with 22 eV photon
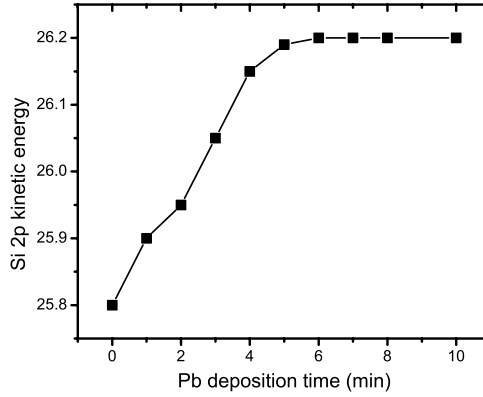
Figure 3.1: Shift of the Si $2p$ core level as a function of Pb deposition, representing the development of the Schottky barrier height. The development is complete at 0.52 ML, resulting in an evaporation rate of 0.11 ML/min.

energy. The incident angle was 45° and the polarization was in the plane of the incident photons and emitted electrons. The signature of the quantum well states is evident from (i) the binding energy shift of the peaks with increasing Pb coverage and (ii) the fact that the binding energy of a quantum well state is independent of photon energy (shown later in Fig. 3.9). Binding energies were determined from the minima of the second derivatives of the photoemission spectra. One can clearly see that the quantum well states shift to lower binding energy with coverage, which may seem counter intuitive but will be explained later on in this Chapter. At 22 eV photon energy, the quantum well states are only observed within a binding energy interval from 0 to 0.7 eV below the Fermi level.

Figure 3.3(a) shows a plot of the quantum well energies as a function of layer thickness (in ML Pb). As a first step toward the interpretation of the data we employ a symmetrical, one-dimensional square well potential [5] with a depth of 12.4 eV (8.1 + 4.3 eV for the Pb work function) and an effective mass of 1.2 m_e. The filled squares represent the energies of the quantum well states that are calculated with this model. The quantum numbers n are indicated and it can be seen that for each measured photoemission 'branch' $p \equiv 3N - 2n$ remains constant (N is the layer thickness in ML). The reduced quantum numbers p are indicated in Fig. 3.3(a).

Each photoemission branch has the property that it supports a new quantum well state as the thickness increases in multiples of two monolayers. The number of antinodes in the wave function (i.e. n) increases by three for each bilayer increment, hence the condition $3N - 2n = $ constant. From the bulk
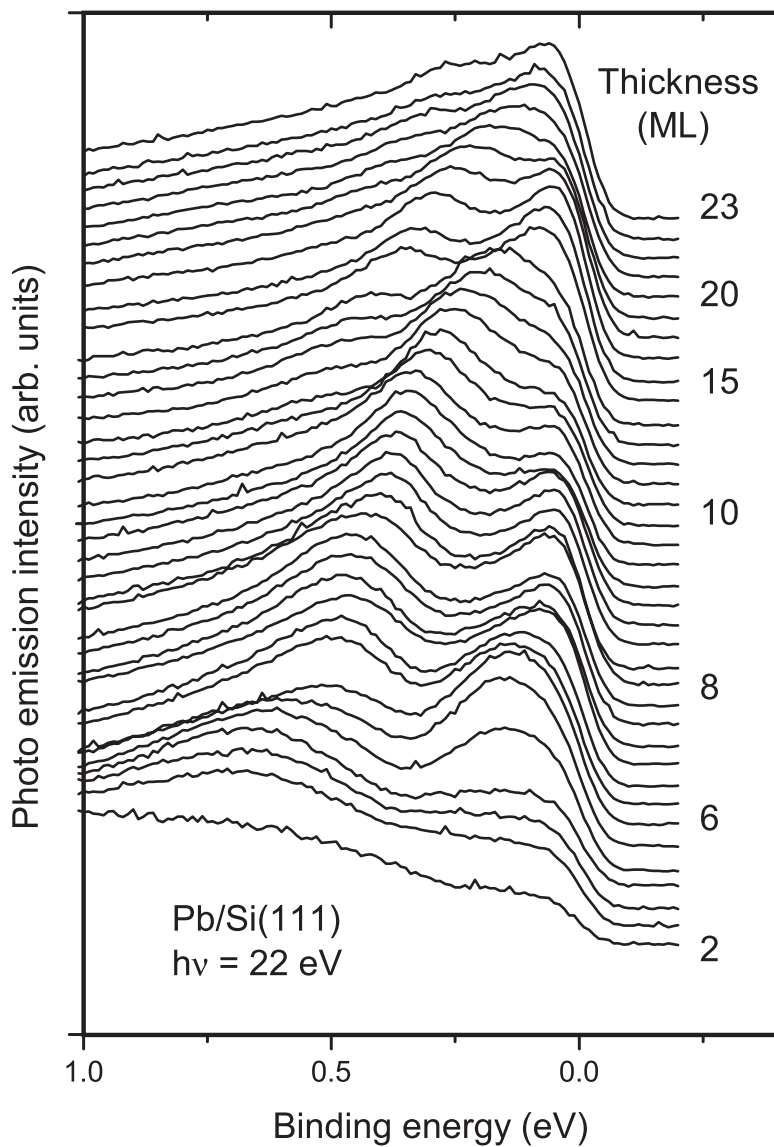
Figure 3.2: Normal-emission photoemission spectra of Pb on Si(111)7×7. The coverage ranges from 2 to 23 ML.
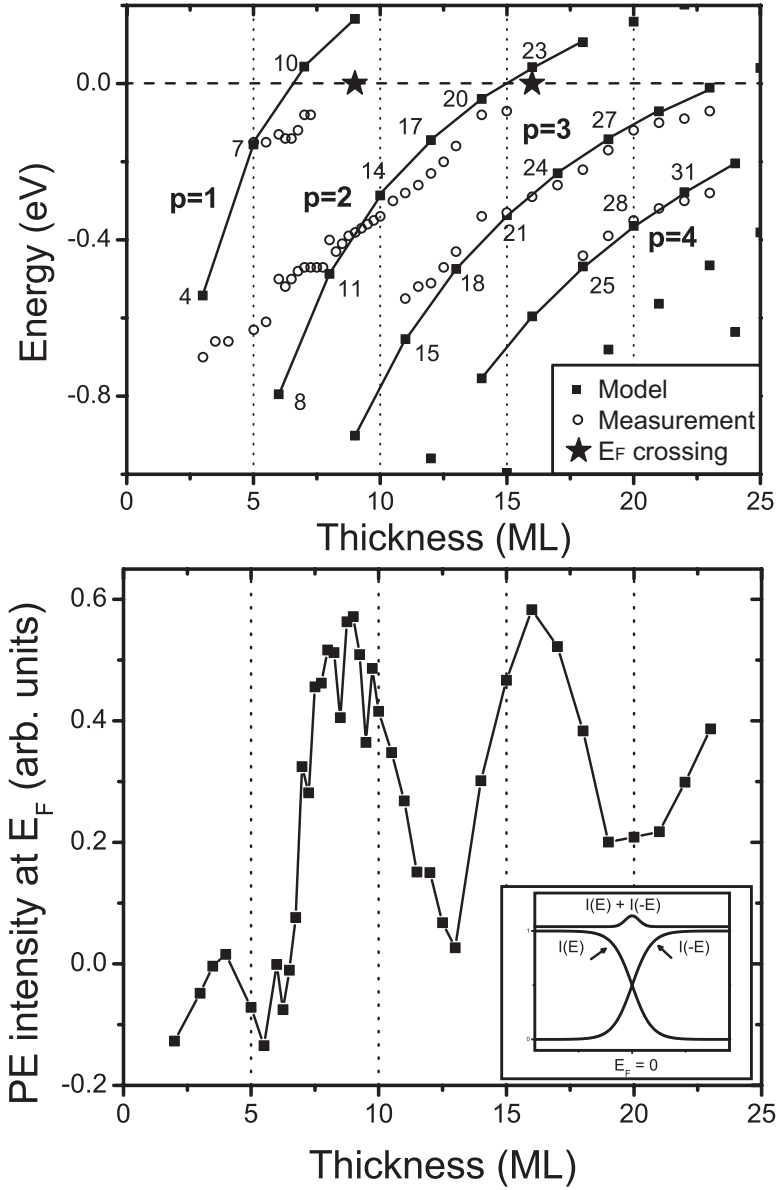
Figure 3.3: (a) Open circles: experimental quantum well states as a function of Pb coverage. The filled squares represent the best fit of the one-dimensional square well model to the photoemission data. The quantum numbers n and p are indicated. The solid lines or 'photoemission branches' serve as a guide to the eye. The filled stars locate the Fermi level crossings of the branches with $p = 1$ and $p = 2$. (b) Photoemission intensity at the Fermi level as a function of Pb coverage. Inset: illustration of the symmetrization procedure.

band structure of Pb [6], one finds that in this range of energy and momentum, $\lambda_F \approx 4d/3$, which shows indeed that a bilayer of Pb can support approximately three antinodes ($d = 2.85$Å and $\lambda_F = 3.95$Å, with k_F in the second Brillouin zone) [5]. The energy goes up slightly for each bilayer increment, which is due to the fact that the wavelength must be squeezed a little so that the wave function can still fit in the well. The number p can be viewed as a reduced quantum number corresponding to the long-wavelength (λ') modulation from the He scattering experiments of Fig. 2.5, which satisfies the condition $p\lambda'/2 = 2Nd$.

This simple model reproduces the Scanning Tunneling Microscopy and Spectroscopy (STM/STS) observations of Su et al. [1] and Altfeder et al. [2] that each quantum well branch only contains contributions from odd- or even-numbered layers. Branches with reduced quantum number p = even (odd) only have contributions from even (odd) layers. Another property of the system is that all films with an even number of atomic layers support a quantum well state 0.6 eV above the Fermi level. These states all belong to the branch $p = 0$ (not shown in Fig. 3.3(a)) and have $k = 3\pi/2d$, which corresponds exactly to the midpoint of the second Brillouin zone [1]. Su and coworkers [1] performed STM/STS measurements on Pb on Si(111)7×7 at 200 K and observed flat-top ('magic') islands on top of a wetting layer of Pb, while Altfeder and coworkers used the same technique on a wedge-shaped Pb island. In both papers, the $p = 0$ state is observed in STS only for (island) heights consisting of an odd number of atomic layers above the wetting layer. The present data provide an important clue regarding the thickness of this wetting layer, namely that the wetting layer in the STM studies consists of an odd number of Pb layers.

From the measurements it is furthermore deduced that the Pb growth is not perfectly layer-by-layer. The quantum well states disperse continuously with Pb coverage and do not reveal monolayer resolution. Neighboring quantum well states in each branch are often separated by less than 0.1 eV and hence it is also much more difficult to achieve monolayer resolution as compared with e.g. Ag films [7]. The small separation of the quantum well states is a direct consequence of the property that each bilayer supports three new states.

We now turn to a more quantitative analysis in terms of the Bohr-Sommerfeld phase accumulation model of Eq. (2.4).

$$2k(E)d + \phi_B(E) + \phi_C(E) = 2\pi n \tag{3.1}$$

The wave vectors $k(E)$ of interest are located in the second Brillouin zone. From this data set the band structure $E(k)$ in the direction normal to the surface and the phase shift ϕ_C can be obtained as described in Section 2.9. When two states have identical binding energy E_b Eq. (2.16) yields:

$$k_z(E_b) = \pi(n_2 - n_1)/(d_2 - d_1), \tag{3.2}$$

Because the dataset is limited to a small energy window of only 0.7 eV, this analysis can only be implemented for four pairs of quantum well states. The binding energies of these pairs were 0.39, 0.30, 0.27, and 0.12 eV. One pair of

states produces one data point in the $k - E$ plot. The result for $E(k)$ is shown in Fig. 3.4(a). The band structure is approximately linear for such a small interval [6]. The fit gives a value for k_F of 1.591 ± 0.006 Å^{-1}, which is in very good agreement with De Haas - Van Alphen measurements [8, 5] which produced a value of 1.596 Å^{-1}.

From this experimental relationship $k(E)$ and WKB values of ϕ_B from Eq. (2.9), ϕ_C can be calculated from Eq. (2.4): $\phi_C = 2\pi n - \phi_B - 2k(E)d$. Since the band structure $k(E)$ is known at only four experimental k-points, the $\phi_C(E)$ plot also consists of only four points. In the small energy window ϕ_C is a slowly varying function of energy. A linear fit gives the result $\phi_C = a + bE$, with $a = 3.1 \pm 0.1$ rad and $b = 0.34 \pm 0.11$ rad/eV, as shown in Fig. 3.4(b). These values are similar to those of Al/Si(111) [9], Ag/Si(001) and Ag/Si(111) [10].

At low coverages (< 8 ML) the finite square well model deviates significantly from the photoemission branches with $p = 1$ and $p = 2$. Of course, the square well model ignores the band structure and does not come anywhere close to reproducing the correct boundary conditions. The deviation from this model becomes increasingly important for thinner films. The phase accumulation model, instead, reproduces the photoemission branches over the entire coverage range. Fig. 3.5 shows a fit to the $p = 2$ photoemission branch using Eq. (3.1) in combination with the condition $n = (3N - p)/2$.

Fig. 3.3(b) shows the 'symmetrized' photoemission intensity at the Fermi level as a function of Pb coverage. The thermal broadening associated with the Fermi Dirac distribution is removed via the so-called symmetrization procedure, a common practice in the high T_c community [11, 12]. In this procedure, a mirror spectrum is generated above E_F (with $E_F = 0$) and subsequently added to the real spectrum, as shown in the inset of Fig. 3.3(b). Following the explanation in Ref. [12], we can show that the symmetrization procedure produces the photoemission spectral function $A(E)$ in the vicinity of the Fermi level, convoluted with a Gaussian instrument resolution $R(E)$. Omitting the **k**-dependence, the measured photoemission intensity can be written as:

$$I(E) = I_0 \int_{-\infty}^{\infty} R(E - E')f(E')A(E')dE' \qquad (3.3)$$

with I_0 a normalization constant. With the assumption that $A(E) = A(-E)$ in the vicinity of the Fermi level, and using $R(E - E') = R(E' - E)$ and $f(E) + f(-E) = 1$, we obtain the following expression for the symmetrized photoemission intensity:

$$I_{symm}(E) = I(E) + I(-E) = I_0 \int_{-\infty}^{\infty} R(E - E')A(E')dE'. \qquad (3.4)$$

Thus, the symmetrization procedure removes the effect of the Fermi-Dirac distribution and provides access to the photoemission spectral function at the Fermi level, regardless of the resolution of the experiment.

The symmetrized intensity peaks when a state crosses the Fermi level. The vertical axis of Fig. 3.3(b) shows the height of the peak in the symmetrized
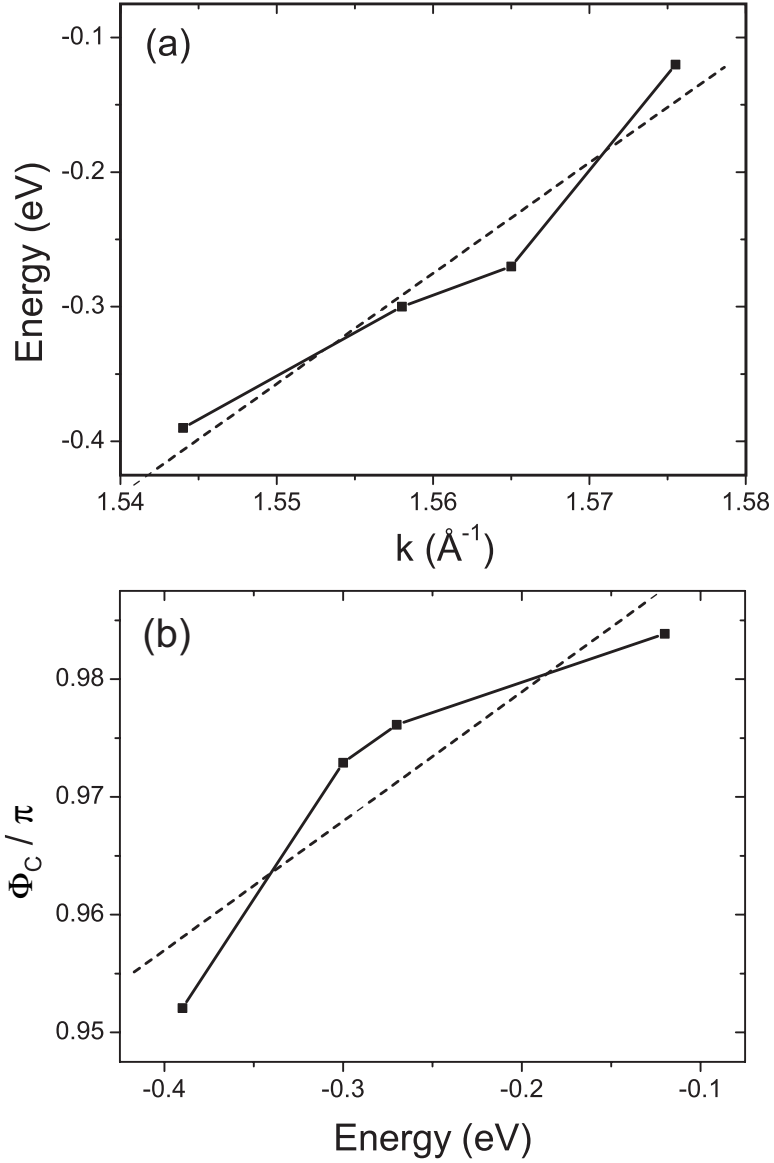
Figure 3.4: (a) Experimental band structure $E(k)$ of Pb in the ΓL direction in the second Brillouin zone. The linear fit produces a k_F of 1.591 ± 0.006 Å^{-1}. (b) Experimental phase shift Φ_C with linear fit.
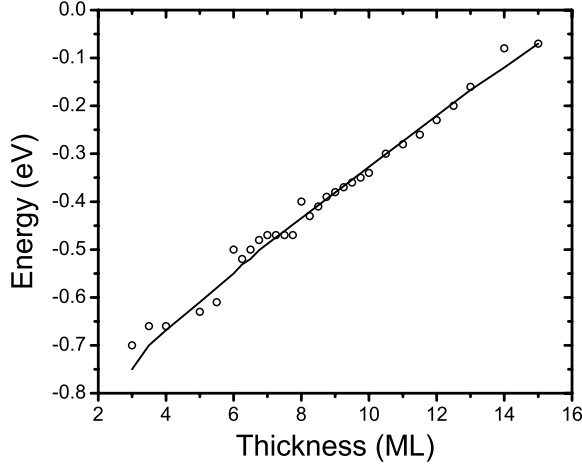
Figure 3.5: (a) Measured quantum well energies for the $p = 2$ branch (open circles) and the fit to the phase accumulation model.

spectrum divided by the height of the Fermi edge of a single spectrum (for normalization purposes). The broad features in Fig. 3.3(b) (i.e. the broad peaks around 9 and 16 ML) correspond to the Fermi level crossing of the first ($p = 1$) and second ($p = 2$) photoemission branches of quantum well states. A quantum well state close to E_F gives rise to an increased intensity at E_F. The maxima of these peaks are indicated as filled stars in Fig. 3.3(a) and are situated where the photoemission branches cross the Fermi level. The overall shape of Fig. 3.3(b) reflects the long wavelength oscillation in the so-called 'misfit function' $\delta = |Nd - n\frac{\lambda_F}{2}|$ which was introduced by Hinch et al. [13] and shown in the upper part of Fig. 2.5. Fermi level crossings appear when $\delta = 0$, which happens when the coverage equals 9 and 16 ML. Pronounced dips in the symmetrized photoemission intensity appear at 13 and 20 ML. At these points, the highest occupied quantum well state has the highest binding energy, i.e. these are the midpoints between two subsequent Fermi level crossings. With increasing coverage, the branches come closer together which explains the fact that the intensity minimum at 13 ML is deeper than the minimum at 20 ML.

The data in Fig. 2 of the paper by Su et al. [1] show the first Fermi level crossing when the Pb islands grow 8 ML high above their wetting layer. Altfeder et al. [2] observe the crossing of the second branch ($p = 2$) at a height of 15 ML. Our data indicate Fermi level crossings at 9 and 16 ML which shows that the wetting layer in the STM experiments [1, 2] can only be one layer thick instead of three, as was claimed by Su and coworkers. Taking a wetting layer of only

1 ML, all of the quantum well energies measured in the STM/STS experiments [1, 2] fit our photoemission results nicely. A 1 ML wetting layer reduces the quantum numbers of Su et al. by 3.

From purely electronic considerations as discussed in Section 2.6, higher binding energies at $\mathbf{k}_\parallel = 0$ imply larger stability [7], which would then suggest that films of 13 ML and 20 ML, and films below approximately 8 ML should be particularly stable. Realizing again that the spectra are not layer resolved and that the $p = 1$ branch belongs to the odd-numbered layers whereas the $p = 2$ branch belongs to the even-numbered layers, it is immediately evident that *below 9 ML, the even numbered layers are more stable than odd numbered layers, whereas the odd numbered layers are more stable between 9 and 16 ML*. Alternatively, below 9 ML islands consisting of an odd number of atomic layers above the wetting layer should be more stable than those with an even number of atomic planes. STM [14] and Spot Profile Analysis LEED data [15] indeed suggest that 5 ML and 7 ML height islands are strongly preferred; however the strongest preference for 7 ML height islands is inconsistent with the increased binding energy of the $p = 2$ branch toward lower coverage. The strong dips at 13 ML and 20 ML call for STM investigations to explore the possibility of a preferred thickness in this coverage range.

3.3.2   Simulation of photoemission spectra

The observed branches in photoemission do not follow the principal quantum number n, but can be characterized instead by a reduced quantum number p. A photoemission branch either contains quantum well states from even-numbered layers or from odd-numbered layers. The question arises whether the simultaneous observation of odd and even branches is caused by a rough growth front, or whether the growth proceeds in bilayers as was originally proposed by Hinch et al. [13]. Bilayer growth of e.g. odd numbered layers would explain the continuous evolution with coverage of the odd branch but would not explain the simultaneous presence of the even branches unless there is a strange mixing of even and odd layered domains during the initial stages of growth. An early scattering study [16] did not reveal experimental evidence for bilayer growth and only very recently the observation of pure bilayer growth has been reported for Pb on Si(111) and Ge(111) [17].

To check whether the shape of the observed branches can be explained by the roughness of the growth front, C.M. Wei and M.Y. Chou performed simulations of photoemission spectra. The quantum well energies were obtained from first-principles calculations of Pb(111) slabs [18] and the thickness distribution was modeled with a Gaussian. The quantum well peaks observed in the spectra were also modelled by Gaussian functions. Fig. 3.6(a) shows the result for a thickness ranging from 1 to 15 ML, with thickness increments of 0.20 ML. The Gaussian width of the growth front is 1.2 ML and the width of a single photoemission peak is 0.20 eV. The simulations reproduce the experiments
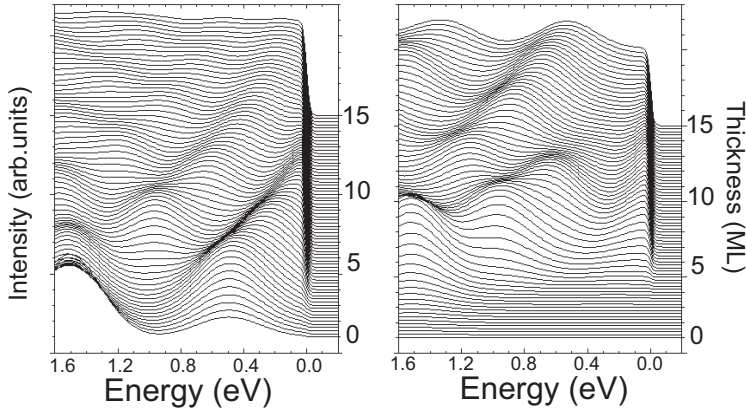
Figure 3.6: (a) Simulated photoemission spectra of Pb(111) slabs. The quantum well state peaks and thickness distribution are modeled with Gaussians with a width of 0.20 eV and 1.2 ML, respectively. (b) Same parameters as in (a), but with a temperature factor included to take the film energy into account.

quite nicely. The $p = 1$ and $p = 2$ branches can be identified as they move to lower binding energy for increasing coverage. The $p = 1$ branch crosses the Fermi level at a coverage of about 10 ML. From this figure it is directly clear that the gradual evolution of the photoemission branches can be attributed to the roughness during growth.

The assumed normal distribution of film thicknesses suggests that the film energy is not an important factor at 110 K, i.e., there are no preferred thicknesses as in STM studies at slightly higher temperature (> 200 K) [1]. A simple way to include the effect of the film energy in the simulations is to include a Boltzmann factor that determines the relative abundance of the various layer heights as a function of temperature. The film energy (see Fig. 5.10) was calculated as a function of film thickness, using DFT. In the low temperature limit, thicknesses with high energy are suppressed, while the high temperature limit reproduces the previous simulations. A representative result is shown in Fig. 3.6(b) for a temperature of 110 K. The Gaussian parameters are identical to Fig. 3.6(a). The suppression of the branch $p = 1$ is clear, which resembles the fact that the odd numbered layers are less favorable in this coverage regime (< 10 ML). At coverages beyond the Fermi level crossing of branch 1 (i.e., above 10 ML), branch 2 has been suppressed. Because these suppressions are not observed in the experiment, we can conclude that the growth proceeded in a quasi layer-by-layer fashion. There is no sign of preferred heights as this would have lead to the (partial) suppression of the photoemission branches in the experiment.

Table 3.1: Effective mass m^* (in units of m_e) as a function of binding energy (in eV) along the ΓM and ΓK direction from DFT calculations of Pb slabs.

Energy (eV)	4.03	3.36	2.54	1.39	0.16
m^*(ΓM)	0.59	0.65	0.78	0.89	1.28
m^*(ΓK)	0.60	0.62	0.64	0.86	1.01

3.3.3   Angle–resolved photoemission

The in-plane dispersion of a variety of quantum well states with up to 4 eV binding energy and coverages ranging from 5 to 12 ML, was measured with angle-resolved photoemission spectroscopy (ARPES). The spectra are recorded at a temperature of 110 K. The photon energy $h\nu$ is chosen to optimize the photoemission intensity of the state to be investigated (see Section 3.3.4). The in-plane dispersion of the quantum well states is parabolic according to Eq. (2.8). An example of this dispersion is shown in Fig. 3.7 for the $p = 2$ state of a 9 ML film, along the two main crystallographic directions ΓM and ΓK. In Fig. 3.7(a) and (b) the gray scale photoemission spectra are shown along the ΓM and ΓK directions, respectively. The parabolic dispersion of the peak maxima is shown in Fig. 3.7(c). The inset of this Figure shows the surface brioullin zone with the Γ, M and K points. The parallel momentum $\mathbf{k}_\parallel$ was obtained from $\hbar\mathbf{k}_\parallel$ = $\sqrt{2mE_k}sin\theta$, with $E_k = h\nu - E_b - \Phi_a$, and Φ_a the work function of the analyzer. The values for the effective masses m^* derived from the spectra along the ΓM and ΓK direction are 3.95 m_e and 3.61 m_e respectively.

The in-plane effective mass was also determined for other quantum well states at different thicknesses (see Fig. 3.8). The observed in-plane effective masses between 2 eV and 4 eV binding energy are close to the free electron mass. At lower binding energy however, the effective masses become extremely high, up to 20 m_e at 0.7 eV binding energy. (The values of 3.95 and 3.61 from the data of Fig. 3.7 are also included in Fig. 3.8 at 0.3 eV binding energy.)

To check whether these high values of the effective mass are an intrinsic property of two-dimensional Pb, Density Functional Theory (DFT) calculations have been performed on free standing Pb films, according to the localized spherical wave (LSW) technique [19]. This method is a modification of the augmented spherical wave (ASW) program that was developed by Williams et al. [20]. Exchange and correlation were treated within the local spin density approximation and scalar relativistic effects were included [21, 22]. The Pb atoms were not allowed to relax in these calculations. The calculated effective masses are listed in Table 3.1.

From these numbers it is clear that the measured values for m^* can not be explained from DFT calculations of free standing Pb(111) slabs. The theoretical values of m^*, ranging from 0.6 to 1.3 m_e, and the increase of the effective mass with decreasing binding energy are however consistent, however, with
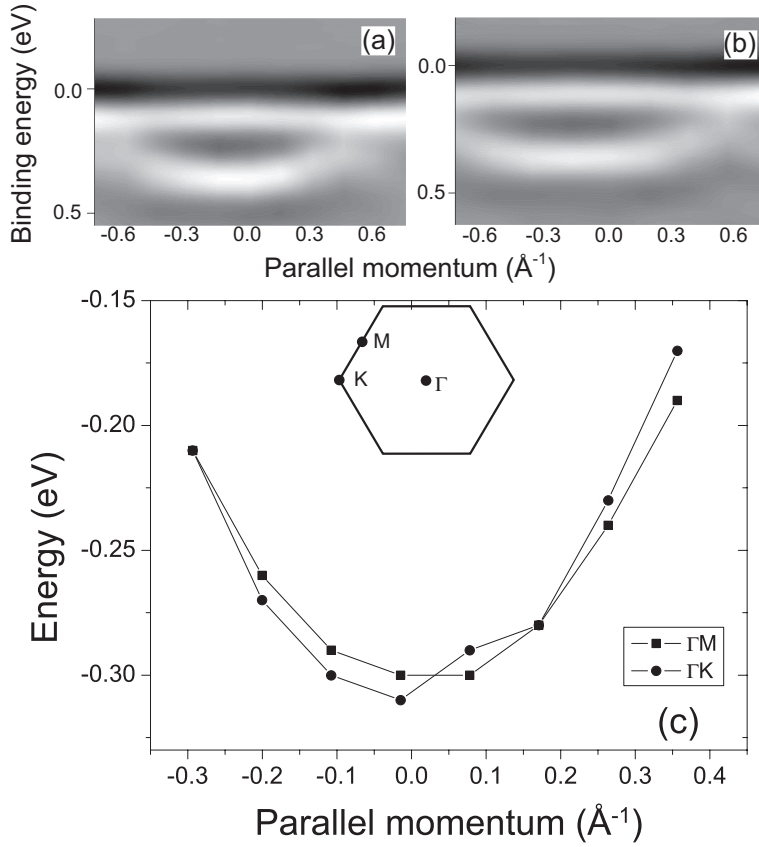
Figure 3.7: Parallel dispersion of a 9 ML Pb film on Si(111)7×7 in the ΓM and ΓK directions. The effective masses are 3.95 and 3.61, respectively. (a) and (b): gray scale plots, (c) Graph showing parabolic dispersion. Inset: Pb(111) surface Brioullin zone, with the high symmetry points Γ, K, and M.
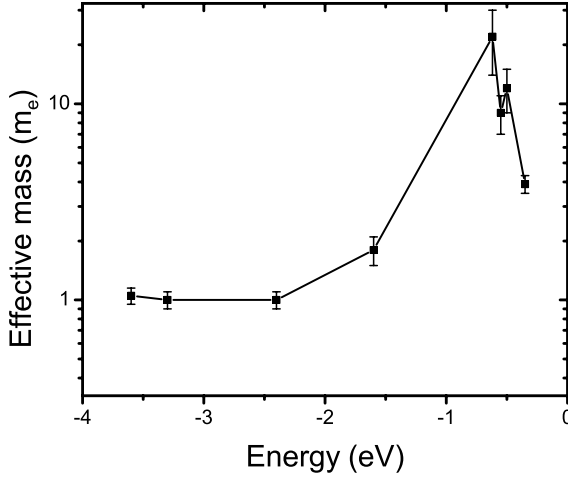
Figure 3.8: Experimental in-plane effective masses from a variety of coverages as a function of binding energy.

the measured values for Al/Si(111) [23] and Ag/Si(111) [24]. Some studies have indicated unexpected trends and sometimes unusually large mass parameters for quantum well states near the valence band edge of the substrate. Examples include Ag on Si(001) [24], Al on Si(111) [23], and Ag or Cu on V(001) [25]. For Pb on Si(111)7×7, the Fermi level is located near the bottom of the Si band gap [26] which means that the maximum of the effective mass curve of Fig. 3.8 must be close to the valence band maximum. We conjecture that this causes the unusually large values for m^*.

This explanation for the unexpectedly high in-plane effective mass is corroborated by the following observation. In a recent photoemission study of ultrathin Pb films on Cu(111) [27] the effective masses of the observed quantum well states do not show the extraordinary behavior of Fig. 3.8, but follow the DFT values of Table 3.1. The copper substrate does not have a band edge in the investigated energy window and the in-plane effective mass therefore appears consistent with the DFT calculations.

3.3.4   Photoemission intensities

At 22 eV photon energy quantum well states can only be observed for binding energies < 0.7 eV. However, if the photon energy is varied, quantum well states can be observed at different binding energies. For example, around $h\nu = 31$ eV
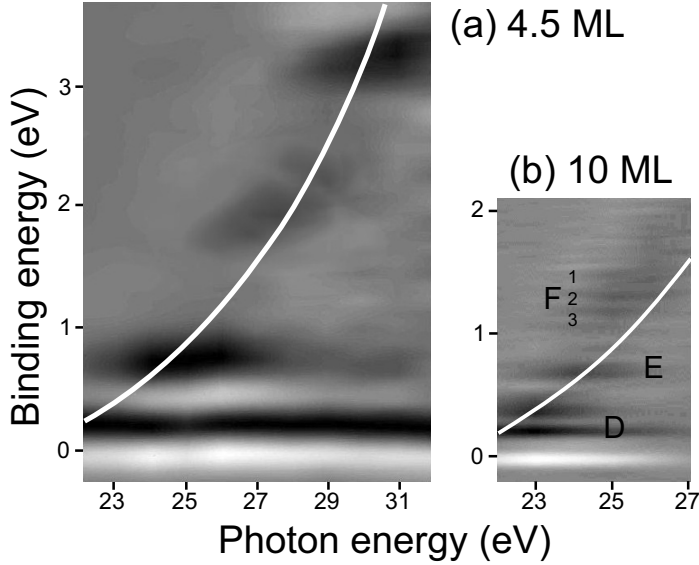
Figure 3.9: Gray scale representation of the photoemission spectra from a 4.5 ML (a) and 10 ML (b) Pb film on Si(111)7×7 as a function of the photon energy. The white line indicates the dispersion of the bulk Pb sp band. High photoemission intensity is represented by dark color.

a quantum well state appears at 3.3 eV binding energy. A series of photoemission spectra from a 4.5 ML Pb film on Si(111)7×7 taken with photon energies from 22 to 32 eV is presented in the gray scale plot of Fig. 3.9(a). This gray scale plot is obtained by multiplying the second derivative of the photoemission spectra with a function that corrects for the increased lifetime broadening at higher binding energy. This correction function is given by $-\sqrt{(\alpha E_b)^2 + \Delta E_{instr}^2}$, with E_b the binding energy, ΔE_{instr} the instrumental energy resolution and α (=0.1) a constant to be adjusted to obtain good contrast in the entire energy range of the plot [28]. Dark regions indicate high photoemission intensity.

It can be clearly seen that the intensity of the quantum well state at 0.7 eV binding energy is diminished for photon energies > 27 eV and that the state at 3.3 eV binding energy is only visible for $h\nu$ > 28 eV. The quantum well state at 2.0 eV binding energy is less pronounced and only visible in the region between 26 and 29 eV. In this 4.5 ML Pb film, the state labelled A at 0.7 eV binding energy can be attributed to the $p = 2$ branch, the state labelled B (1.9 eV binding energy) to the $p = 3$ branch and state C (3.3 eV binding energy) to the $p = 4$ branch. The contribution of the $p = 1$ branch is observed in the raw spectra for photon energies from 22 to 25 eV, but it is not visible in the gray scale plot due to the strong curvature near the Fermi level.

For the 10 ML film of Fig. 3.9(b), states D and E at 0.3 and 0.7 eV bind-ing energy can be attributed to the $p = 2$ and $p = 3$ branches, respectively. For binding energies greater than 1 eV, the individual quantum well states of the $p = 4$ branch (1.1 to 1.5 eV binding energy) can be observed and are la-belled F1-3. From the simple finite square well model, one finds that the F1, F2, and F3 states correspond to different layer thickness (8, 10 and 12 ML, respectively), which is again indicative of a rough growth front.

The observed intensity maxima of the quantum well states coincide with photon energies for direct transitions in bulk Pb. The curves in Figs. 3.9(a) and (b) indicate the locations where direct transitions would be possible in bulk Pb [6]. The valence states in ultrathin films are quantized, but the photoemis-sion matrix elements do not deviate much from those in the bulk [29, 30]. In thin films, however, matrix elements only integrate over the film region, which causes a broadening in momentum (=energy) space. This is illustrated in the Figures 3.9(a) and (b). Horizontal lines in this figure can be regarded as con-stant initial state (CIS) spectra. The photon energy width in which a certain quantum well state can be observed for a 10 ML film is 1.7 ± 0.1 eV (Fig. 3.9(b)) while for a 4.5 ML film it is 2.7 ± 0.3 eV (Fig. 3.9(a)). In summary, the photoemission cross section peaks at the energy locations of the vertical transitions in bulk Pb and the width of the peaks in the CIS spectra is due to the finite thickness of the film [31].

3.4   Summary

The growth of Pb on Si(111) has been studied with photoemission spectroscopy. The experimental photoemission branches of quantum well states can be de-scribed with a reduced quantum number $p \equiv 3N - 2n$. The number p can be viewed as a reduced quantum number corresponding to a long-wavelength modulation that satisfies the condition $p\lambda'/2 = 2Nd$. The photoemission bran-ches reflect the general property of the Pb films that in the energy range of interest, each bilayer of Pb can support approximately three antinodes of the quantum well wave function. The photoemission branches cross the Fermi level when the condition $Nd = n\lambda_F/2$ is satisfied. From simulation of the spectra it is concluded that the observed development of the photoemission branches can be explained by the roughness in the growth front. The quantum well states are furthermore characterized by a large binding energy dependence of the in-plane effective mass and strong matrix element effects for photo-ionization. The present study also sheds some light on previous STM experiments. It is now evident that below 9 ML, films with an even number of atomic layers are electronically more stable than those with an odd number of layers. This ob-servation accounts for the fact that the 'magic' islands in STM studies all have an odd number of atomic layers above the wetting layer. The wetting layer in the STM studies consists of only a single layer of Pb.

Bibliography

[1] W. B. Su *et al.*, Phys. Rev. Lett. **86**, 5116 (2001).

[2] I. B. Altfeder, K. A. Matveev, and D. M. Chen, Phys. Rev. Lett. **78**, 2815 (1997).

[3] B. N. Jensen *et al.*, Nucl. Instr. Meth. A **394**, 243 (1997).

[4] D. R. Heslinga *et al.*, Phys. Rev. Lett. **64**, 1589 (1990).

[5] M. Jalochowski and E. Bauer, Phys. Rev. B **38**, 5272 (1988).

[6] K. Horn *et al.*, Phys. Rev. B **30**, 1711 (1984).

[7] D. A. Luh *et al.*, Science **292**, 1131 (2001).

[8] J. R. Andersen and A. V. Gould, Phys. Rev. **139**, A1459 (1965).

[9] L. Aballe *et al.*, Surf. Sci. **482-485**, 488 (2001).

[10] A. Arranz *et al.*, Phys. Rev. B **65**, 195410 (2002).

[11] M. R. Norman *et al.*, Nature **392**, 157 (1998).

[12] J. Mesot *et al.*, Phys. Rev. B **63**, 224516 (2001).

[13] B. J. Hinch, C. Koziol, J. P. Toennies, and G. Zhang, Europhys. Lett. **10**, 341 (1989).

[14] M. Hupalo and M. C. Tringides, Phys. Rev. B **65**, 115406 (2000).

[15] V. Yeh *et al.*, Phys. Rev. Lett. **85**, 5158 (2000).

[16] D. Schmicker *et al.*, J. Phys. Cond. Matt. **9**, 969 (1997).

[17] M. M. Özer *et al.*, Phys. Rev. Lett. submitted .

[18] C. M. Wei and M. Y. Chou, Phys. Rev. B **66**, 233408 (2002).

[19] H. van Leuken *et al.*, Phys. Rev. B **41**, 5613 (1990).

[20] A. R. Williams, J. K Cler, and C. D. Gelatt Jr., Phys. Rev. B **19**, 6094 (1979).

[21] L. Hedin and B. I. Lundqvist, J. Phys. C **4**, 2064 (1971).

[22] M. Methfessel and J. K Cler, J. Phys. F **12**, 141 (1982).

[23] L. Aballe *et al.*, Phys. Rev. Lett. **87**, 156801 (2001).

[24] I. Matsuda, T. Ohta, and H. W. Yeom, Phys. Rev. B **65**, 085327 (2002).

[25] T. Valla *et al.*, Phys. Rev. B **54**, 11786 (1996).

[26] H. H. Weitering, D. R. Heslinga, and T. Hibma, Phys. Rev. B **45**, 5991 (1992).

[27] J. H. Dil *et al.*, Phys. Rev. B **70**, 045405 (2004).

[28] T. Abukawa *et al.*, Surf. Sci. **325**, 33 (1995).

[29] E. D. Hansen, T. Miller, and T. -C. Chiang, J. Phys.: Cond. Matter **9**, L435 (1997).

[30] M. Milun, P. Pervan, and D. P. Woodruff, Rep. Prog. Phys. **65**, 99 (2002).

[31] A. Mugarza *et al.*, Phys. Rev. B. **62**, 12672 (2000).

Chapter 4

Structure determination with LEED–I(V)

4.1   Introduction

In 1927, Davisson and Germer [1] showed that electrons are waves that can be diffracted by surfaces. The interaction of electrons with a crystal can give important information about the electronic and atomic structure of the surface. Especially low energy electrons (electrons with energies from 20 to 400 eV) are ideal probes for surface studies, because they are easily scattered, both elastically and inelastically. If an electron penetrates the surface, it can either propagate into the electron sea or back-scatter from the crystal (elastically or inelastically). Back-scattered electrons can provide chemical and structural information about the first four or five atomic layers of the crystal. The elastically scattered electrons can be used to determine the atomic structure of the solid's outermost five layers, while the inelastically scattered electrons (i.e. the ones that have lost energy) provide information about the electronic structure and excitations. In this Chapter, we focus on the use of the elastically scattered electrons for the purpose of structure determination.

First, in Section 4.2 the kinematic theory of scattering will be reviewed. This single scattering theory has proved to be very successful for the interpretation of X-ray and neutron diffraction experiments. In low energy electron diffraction (LEED) experiments, however, multiple scattering events play a crucial role, because the interaction of electrons with solids is much stronger than for X-rays. This leads us to the dynamical theory of diffraction which includes multiple scattering as oulined in Section 4.3. The most straightforward use of the LEED experiment (Section 4.4) is to obtain the symmetry of the surface from a visual inspection of the diffraction pattern. The LEED pattern corresponds to the two-dimensional reciprocal lattice. Analysis of the diffracted intensities as a function of electron energy presents the possibility for quantitative structural
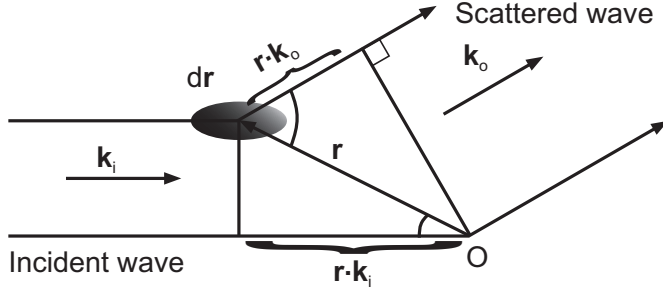
Figure 4.1: The scattered amplitude is proportional to the Fourier integral of the scattering power $\rho(\mathbf{r})$.

analysis. Section 4.5 describes the use of the dynamical theory for obtaining the atom positions at the surface from the measured intensity profiles. Finally, the structure of the Cu(001) surface has been investigated as a test case for our LEED data acquisition hardware and computational capability to resolve surface structures via LEED I(V).

4.2   Kinematic theory

4.2.1   Scattering amplitudes

The kinematic diffraction theory provides a description of scattering within the framework of single, elastic scattering. It also illustrates some important properties of scattering from surfaces [2]. We introduce the theory in its general form, which holds for any wave or wave-like particle such as electrons, atoms, molecules, and neutrons.

A mono-energetic plane wave is described by:

$$\Psi = A_i \exp(i\mathbf{k}_i \cdot \mathbf{r}), \tag{4.1}$$

where Ψ is the (particle) wave function, A_i is the amplitude, $\mathbf{k}_i$ is the incident wave vector, and $\mathbf{r}$ is the space vector. If we only include single scattering, the amplitude of the scattered wave, with wave vector $\mathbf{k}_o$, is proportional to both A_i and the integral of the scattering power $\rho(\mathbf{r})$. The scattering power is specific to the scattering process (electrons, neutrons, X-rays, atoms, etc.). The scattering power must be integrated with the proper phase over the scattering volume as Figure 4.1 illustrates. The scattered amplitude A_o becomes:

$$A_o = \alpha A_i \int \rho(\mathbf{r}) \exp(i\mathbf{s} \cdot \mathbf{r}) d\mathbf{r}. \tag{4.2}$$

The reciprocal space vector $\mathbf{s} = \mathbf{k}_o - \mathbf{k}_i$ is the momentum transfer. The indices i and o represent the incident and scattered entities. The integral is, except for a constant which depends on the convention, the Fourier transform of the scattering power $\rho(\mathbf{r})$. For a single atom n the transform is called the atomic scattering factor $f_n(\mathbf{s})$. For an arrangement of atoms at positions $\mathbf{r}_n$ the scattered wave can than be expressed as:

$$\Psi_s = A_i \alpha \Big[\sum_n f_n(\mathbf{s}) \exp(i\mathbf{s} \cdot \mathbf{r}_n) \Big] \exp(i\mathbf{k}_o \cdot \mathbf{r}), \qquad (4.3)$$

in which the summation runs over all scattering atoms. The above expressions for the scattered wave hold for any atomic arrangement. No crystal structure is included to reach this result. The expression that appears between square brackets in Eq. (4.3) is generally known as the structure factor S [3]. It is in general a continuous function $S(\mathbf{s})$ of the position vector $\mathbf{s}$ in reciprocal or Fourier space. We only include elastic scattering where no energy is lost in the scattering process, and therefore $|\mathbf{k}_i| = |\mathbf{k}_o|$.

In X-ray scattering the atomic scattering factor is usually taken to be isotropic: $f_n(s)$. For electron scattering, however, multiple scattering within the atom causes $f_n(\mathbf{s})$ to be highly anisotropic. If we choose an atomic scattering factor $f_n(s)$ which is direction independent (i.e., isotropic scattering), we would only be able to describe an observed LEED pattern and the mean peak positions in intensity curves. Therefore, in the kinematic theory of LEED the angular dependence of the scattering factor is a necessary ingredient.

Upon entering the solid, incident electrons have to pass the surface dipole layer, gaining an amount of kinetic energy V_0, the inner potential. The potential landscape inside the solid is lowered by a constant amount V_0 and therefore the electrons entering the solid are refracted, which affects both $\mathbf{k}_i$ and $\mathbf{k}_o$.

4.2.2 The Ewald sphere construction

The condition that, in the monochromatic and elastic case, the diffracted and incident wave vectors must have the same length led P.P. Ewald to the following geometric construction, the so called Ewald sphere construction. The vector $\mathbf{k}_i$ points to the origin of reciprocal space. The origin of the vector $\mathbf{k}_i$ is the center of a sphere with radius $|\mathbf{k}_i|$. The vector $\mathbf{k}_o$ also originates from the center of the sphere. Taking the incident beam direction as our reference direction, the end point of the vector $\mathbf{k}_o$ is also confined to the sphere. This, in turn, implies that the end point of the vector $\mathbf{s}$ is located on the same spherical surface. Thus, if the orientation between the scattering object and incident beam is kept constant, structure factors can only be observed if the vector $\mathbf{s}$ is located on the sphere. Figure 4.2 illustrates the Ewald construction, which reflects the condition of monochromatic and elastic scattering. It holds for any atomic configuration, no crystalline arrangement of the atoms is involved in its construction. If the energy (and thus $|\mathbf{k}_i|$) is changed, then the Ewald sphere
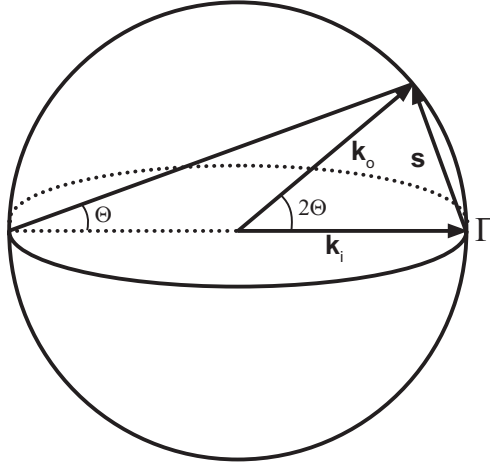
Figure 4.2: The Ewald sphere construction.

also changes, leading to the observation of $S(\mathbf{s})$ at other locations in reciprocal space. Changing the orientation of the scattering object with respect to $\mathbf{k}_i$, other objects (e.g., points, lines, planes) in reciprocal space can intersect the Ewald sphere.

4.2.3   The 3D Laue conditions

Any ordering of the atomic arrangement in real space will be reflected in the Fourier transform (i.e., the structure factor), in reciprocal space. Especially when the atomic arrangement shows strict translational symmetry, non zero values of $S(\mathbf{s})$ are confined to sets of parallel planes, parallel lines or even to a lattice of points in reciprocal space. The Ewald sphere construction tells us that non-zero values of $S(\mathbf{s})$ can be observed only if these planes, lines or lattice points coincide with the Ewald sphere. These restrictions lead to the Laue conditions for diffracted beams. Only beams fulfilling the Laue conditions can be observed.

The atomic positions $\mathbf{r}_n$ in the structure factor of a 3D crystal can be represented by the sum of the vectors of the lattice and the vectors within the unit cell: $\mathbf{r}_n = m_1\mathbf{a}_1 + m_2\mathbf{a}_2 + m_3\mathbf{a}_3 + \mathbf{R}_c$. Here, $\mathbf{R}_c$ are the space vectors of the atoms in the unit cell, $\mathbf{a}_1, \mathbf{a}_2, \mathbf{a}_3$ are the translation vectors of the lattice and m_1, m_2, m_3 are integers. The 3D structure factor S^{3D} can now be written as:

$$S^{3D}(\mathbf{s}) = \sum_c f_c(\mathbf{s}) \exp(i\mathbf{s} \cdot \mathbf{R}_c) \Big[\sum_{m_1,m_2,m_3} \exp(i\mathbf{s} \cdot [m_1\mathbf{a}_1 + m_2\mathbf{a}_2 + m_3\mathbf{a}_3]) \Big]. \quad (4.4)$$

The sum over the lattice vectors is equal to $\delta(\mathbf{s} - \mathbf{g})$, with $\delta(\mathbf{x})$ a 3D Dirac delta function and $\mathbf{g}$ a vector of the 3D reciprocal lattice. Given the lattice $(\mathbf{a}_1, \mathbf{a}_2, \mathbf{a}_3)$ the reciprocal lattice vectors are given by

$$\mathbf{g} = h\mathbf{g}_1 + k\mathbf{g}_2 + l\mathbf{g}_3, \tag{4.5}$$

with

$$\mathbf{g}_1 = 2\pi \frac{\mathbf{a}_2 \times \mathbf{a}_3}{\mathbf{a}_1 \cdot (\mathbf{a}_2 \times \mathbf{a}_3)}, \mathbf{g}_2 = 2\pi \frac{\mathbf{a}_3 \times \mathbf{a}_1}{\mathbf{a}_1 \cdot (\mathbf{a}_2 \times \mathbf{a}_3)}, \mathbf{g}_3 = 2\pi \frac{\mathbf{a}_1 \times \mathbf{a}_2}{\mathbf{a}_1 \cdot (\mathbf{a}_2 \times \mathbf{a}_3)}. \tag{4.6}$$

So, in the 3D structure factor of Eq. (4.4) the last factor (equal to the Dirac delta function $\delta(\mathbf{s} - \mathbf{g})$) defines the direction of the diffracted beams and is called the 3D Laue condition:

$$\mathbf{s} = \mathbf{k}_o - \mathbf{k}_i = \mathbf{g}. \tag{4.7}$$

The first factor in Eq. (4.4) (with the atomic scattering factors) defines the scattered intensity. In this 3D case the structure factor $S^{3D}(\mathbf{s})$ has only non zero values at the points of the reciprocal lattice. This means that only accidentally a diffracted beam will be present, i.e., when one of these reciprocal lattice points happens to lie on the surface of the Ewald sphere. By carefully selecting the corresponding orientations of the crystal with respect to the incident beam, the diffracted beams can successively be observed. This 3D case is suitable to describe X-ray and neutron scattering experiments where the incident beam traverses a whole three dimensional crystal. In the case of surface diffraction only translational symmetry in two dimensions is observed. This leads us to the 2D Laue conditions.

4.2.4 The 2D Laue conditions

Low energy electrons, usually with energies from 20 to 400 eV, have a significant interaction with matter. This interaction gives rise to elastic and inelastic scattering. In the LEED experiment, only elastically scattered electrons are considered. Inelastically scattered electrons generally do not contribute to the observed diffracted intensities.

   All inelastic scattering processes can be parameterized with a single parameter, the inelastic mean free path (IMFP). In general, the IMFP is energy dependent because the scattering processes are energy dependent [4]. The dependence of the IMFP on the energy of the electrons is shown in Fig. 4.3. Inelastic scattering is strongest near 50 eV electron energy, resulting in an IMFP of only ≈ 5 Å. In the energy region of interest (20-400 eV) backscattered electrons probe a surface depth of approximately 10 to 20 Å.

   Another way to represent the IMFP is by the use of a complex inner potential $V_0 = V_{0r} + iV_{0i}$ and a complex wave number [2, 5] $k = k_r + ik_i$. A plane wave $\exp(ikx)$ with energy $E = \hbar^2 k^2 / 2m$ penetrating a surface, acquires an energy $E + V_0 = \hbar^2 k'^2 / 2m$ (i). The wave inside the crystal is represented by $\exp(ik'x) = \exp(ik'_r x) \exp(-k'_i x) = \exp(ik'_r x) \exp(-x/\lambda)$ (ii). The imaginary part of
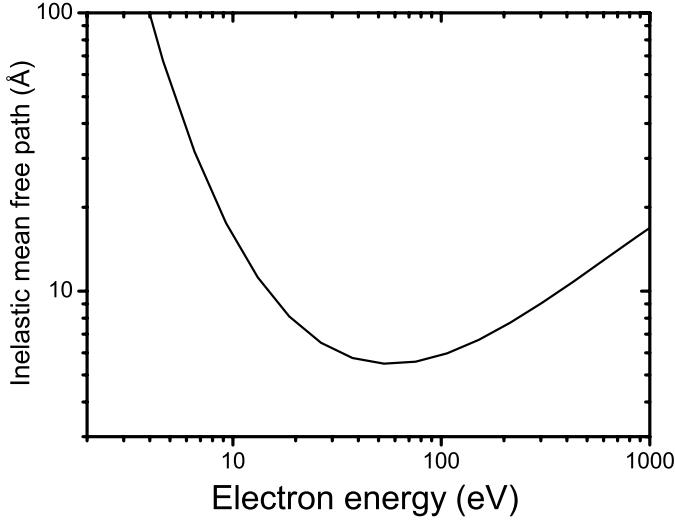
Figure 4.3: Schematic drawing of the electron inelastic mean free path as a function of energy.

the wave number describes the damping of the wave function inside the crystal by the inelastic mean free path $\lambda = 1/k_i'$. Separation of the real and imaginary parts of (*i*) and (*ii*) gives an expression for λ: [2, 5]

$$\lambda = \frac{1}{k_i'} \propto \frac{\sqrt{E + V_{0r}}}{V_{0i}} \tag{4.8}$$

The choice of

$$V_{0i} = C \left(\frac{E}{7.35 + V_{0r}} \right)^{\frac{1}{3}} \tag{4.9}$$

for the imaginary part of the inner potential [5] results in a reasonable approximation of $\lambda(E)$ (Fig. 4.3) in the energy range of interest in LEED, 20-400 eV.

We know that only the outermost 10 to 20 Å of the crystal contributes to the observed LEED intensities, hence the periodicity of the diffracting lattice is lost in the direction normal to the surface. Translational symmetry in only two directions is preserved, leading to a two dimensional space lattice with translation vectors $\mathbf{a}_1$ and $\mathbf{a}_2$ both parallel to the surface. The atomic positions now must be written in the form $\mathbf{r}_n = m_1 \mathbf{a}_1 + m_2 \mathbf{a}_2 + \mathbf{R}_c$. $\mathbf{R}_c$ is a three dimensional vector describing the atomic positions within the boundaries of the two dimensional unit cell defined by $\mathbf{a}_1$ and $\mathbf{a}_2$, which happen to lie in the slice of the crystal that

contributes to the LEED intensities. The 2D structure factor S^{2D} now becomes:

$$S^{2D} = \sum_c f_c(\mathbf{s}) \exp(i\mathbf{s} \cdot \mathbf{R}_c) \Big[\sum_{m_1, m_2} \exp(i\mathbf{s} \cdot [m_1 \mathbf{a}_1 + m_2 \mathbf{a}_2]) \Big]. \tag{4.10}$$

The lattice sum in the last factor is zero unless both $\mathbf{s} \cdot \mathbf{a}_1 = 2\pi h$ and $\mathbf{s} \cdot \mathbf{a}_2 = 2\pi k$, where h and k are integers. That means that the vector $\mathbf{s}$ must end on one of the intersecting lines of two sets of equidistant parallel planes, which are perpendicular to the surface. The lattice sum can be written as $\delta(\mathbf{s}_\parallel - \mathbf{g}_\parallel)$, where $\mathbf{s}_\parallel$ and $\mathbf{g}_\parallel$ are the component vectors of $\mathbf{s}$ and $\mathbf{g}$ parallel to the surface. The vector $\mathbf{g}_\parallel$ is defined by:

$$\mathbf{g}_\parallel = h\mathbf{g}_1 + k\mathbf{g}_2, \tag{4.11}$$

with

$$\mathbf{g}_1 = 2\pi \frac{\mathbf{a}_2 \times \hat{\mathbf{n}}}{\mathbf{a}_1 \cdot (\mathbf{a}_2 \times \hat{\mathbf{n}})}, \mathbf{g}_2 = 2\pi \frac{\hat{\mathbf{n}} \times \mathbf{a}_1}{\mathbf{a}_1 \cdot (\mathbf{a}_2 \times \hat{\mathbf{n}})}. \tag{4.12}$$

These vectors span the two dimensional reciprocal lattice conjugate to $\mathbf{r} = m_1 \mathbf{a}_1 + m_2 \mathbf{a}_2$. Within the framework of this two dimensional representation a corresponding 2D Laue condition for LEED can be formulated as:

$$\mathbf{s}_\parallel = \mathbf{k}_{o\parallel} - \mathbf{k}_{i\parallel} = \mathbf{g}_\parallel. \tag{4.13}$$

In three dimensional direct and reciprocal space the Laue condition is still given by Eq. (4.7). In 3D reciprocal space this implies that because of Eq. (4.11) the end points of vectors $\mathbf{g}$ are confined to a set of parallel lines perpendicular to the surface. The 3D concept of reciprocal lattice points must be replaced by lattice lines or rods. Only along these rods, but everywhere on them, the Laue conditions are fulfilled. This situation is shown in Fig. 4.4(a). If now in a diffraction experiment the energy is increased, the Ewald sphere radius increases and the sphere slides along the rods. So every rod contributes to the diffracted intensity, as long as the Ewald sphere intersects the rod.

Restricting the diffraction to the last factor (between square brackets) in Eq. (4.10), would result in a uniform distribution along the rods. The factor in Eq. (4.10) in front of the square brackets modulates the intensity because $\mathbf{R}_c$ will point into the dimension perpendicular to the surface. Diffraction from the atoms in a 10 to 20 Å thick layer makes the intensity along the rods to be structured. The diffracted intensity depends on the position on the rod. When the energy of the incoming electrons is varied, the radius of the Ewald sphere changes while it remains fixed at the origin Γ. The intersection of the sphere and the rods shifts along the rods and the diffracted intensity shows minima and maxima, as can be seen in Fig. 4.4(b). In LEED theory, the experimental curve describing the diffracted intensity along a 2D reciprocal lattice rod is called and I(V)-curve, intensity versus acceleration voltage of the electrons. The main peaks in the I(V)-curve are at the energies of the 3D Laue conditions.
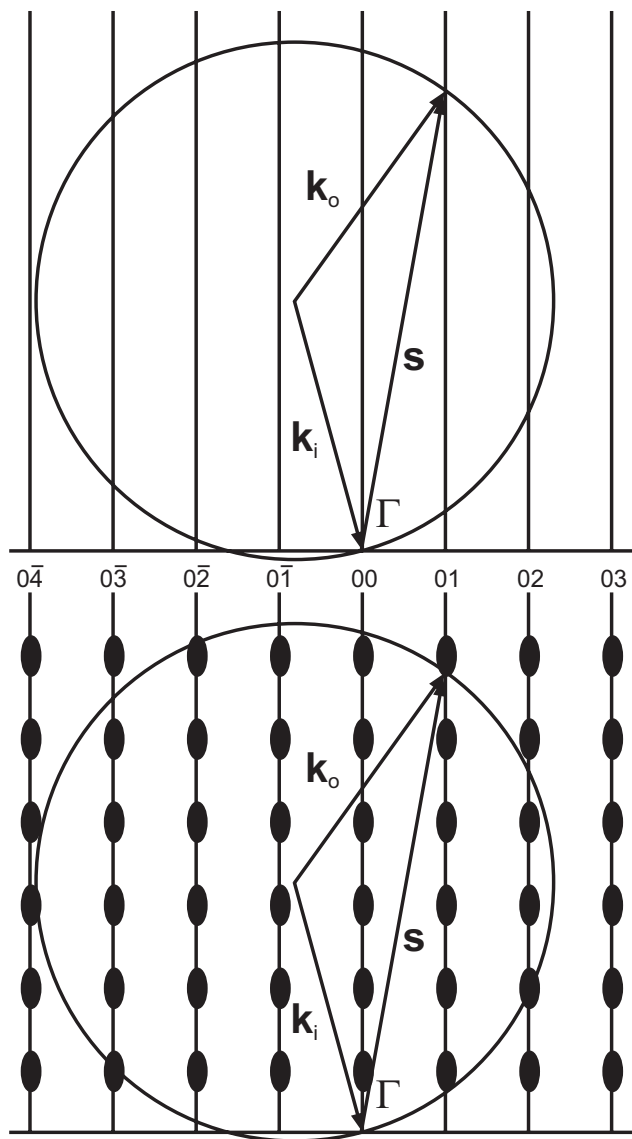
Figure 4.4: Ewald sphere construction for scattering from (a) a two–dimensional lattice, (b) a thin surface slice, giving rise to structured rods, see text.
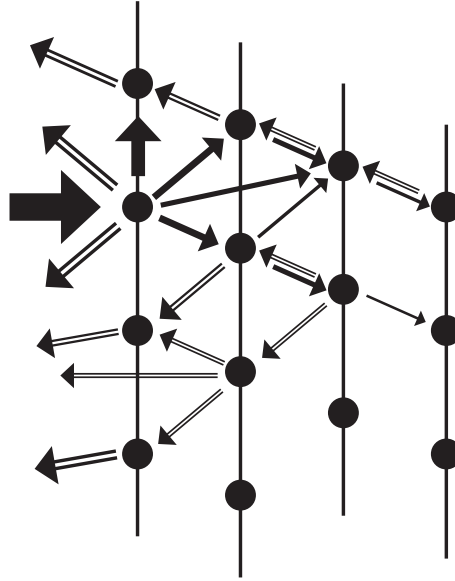
Figure 4.5: Schematic drawing of forward (solid arrows) and backward (open arrows) scattered waves. The amplitude of the waves is damped due to inelstic scattering.

4.3   Dynamic theory

The major difference between the dynamical and kinematic theory of diffraction is that dynamical theory includes the treatment of multiple scattering, while kinematic theory does not. In this section, the ingredients of the dynamical theory will only be briefly explained. For a more detailed description, several LEED theory books are available, such as the books written by M.A. van Hove [2] and J.B. Pendry [4].

The diffracted amplitudes in the dynamical theory are calculated in a two-step process. First, the scattering property of a single atom is considered as a function of the direction and energy of the incoming wave. Multiple scattering effects occur even in a single atom and are taken into account. Second, all these scattering atoms are positioned at their crystal sites in layers parallel to the surface and these layers are stacked to form the crystal structure. For each layer, beginning with the topmost layer, the scattered wave is calculated both in the forward and backward direction. The backward scattered wave contributes to the measured intensities, while the forward scattered wave is the incident wave for the next layer of atoms. The amplitude of the wave inside the crystal is damped due to inelastic scattering (Section 4.2.4), and when its value drops under a certain value it is no longer taken into account. Fig. 4.5 shows a

schematic illustration of this procedure. In this way the total scattered wave outside the crystal is calculated with the atomic positions as input parameters.

4.3.1   Atomic phase shifts

To calculate the diffracted intensities, the potential inside the crystal is approximated by a muffin-tin potential [2]. The ion cores are surrounded by spherically symmetrical potentials up to a radius r_m, while outside these spheres the potential is approximated by a constant value, the muffin-tin constant. The muffin-tin constant and the real part of the inner potential V_{0r} are used interchangeably in LEED literature, and we shall do this here as well.

The scattering amplitude of the atoms in the muffin-tin potential can be written [2, 5] as:

$$f(k, \theta) = \frac{1}{2ik} \sum_l (2l + 1)(e^{2i\delta_l} - 1)P_l(cos\theta), \tag{4.14}$$

with k the wave number, l the angular momentum, θ the polar angle and P_l the l-th Legendre polynomial. The scattering amplitude does not depend on the azimuthal angle ϕ since the atomic potential is completely symmetrical. Eq. (4.14) shows that the scattering amplitude depends mainly on the atomic phase shifts δ_l, which are therefore an essential part of the dynamical calculation of the diffracted intensities. The equations to calculate the atomic phase shifts as a function of energy can be achieved by matching the wave functions and their first derivatives at the muffin-tin radius r_m [2, 5]. Note that this is identical to the case of the square well potential (Sec. 2.2).

The summation in Eq. (4.14) runs from zero to infinity, so, in practice we have to limit this summation to a certain l_{max}. A simple way to estimate a reasonable value for l_{max} is to consider the number of oscillations of the electron wave within the atomic potential, which is $\pi d/\lambda$, with d being the 'diameter' of the atom [2]. Since a polynomial of order l can have l full oscillations, the l_{max} needed is approximately $\pi d/\lambda$. For example, an electron with 100 eV kinetic energy has a wavelength of approximately 1 Å and therefore needs $l_{max} \approx 9$. In practice this value will be somewhat too large, because the outer part of the atom scatters rather weak, reducing the effective diameter of the atom. When the electron energy is increased, and therefore the electron wavelength decreased, a larger value for l_{max} is needed.

4.4   Experimental setup

A schematic drawing of the experimental LEED setup is shown in Fig. 4.6. The sample is positioned at the center of four concentric grids and a phosphorous screen. An electron gun is used to generate an electron beam that is accelerated by a voltage V_a. The entire setup is placed in an ultra high
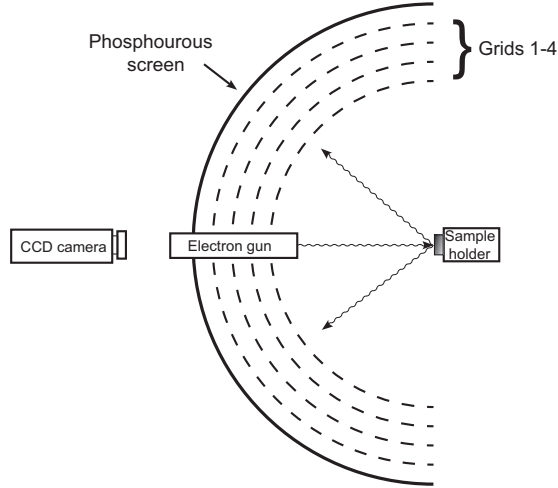
Figure 4.6: Schematic drawing of the experimental LEED setup.

vacuum (UHV) chamber, for reasons of surface cleanliness. From the sample both elastically and inelastically scattered electrons are moving towards the hemispherical grids. The first three grids are used to filter out the inelastically scattered electrons that have an energy less than eV_a. Only electrons that do not lose energy during the scattering process are allowed to pass. The fourth grid is then used to accelerate these electrons with a high voltage to visualize them on the phosphorous screen. Behind this screen a CCD camera is positioned to grab the actual diffraction pattern into a computer file. By taking diffraction patterns for a range of energies, the intensity of diffracted beams can be measured as a function of energy. Since the electron current from the sample is dependent on the energy of the electrons, the measured diffracted intensities have to be normalized with respect to this emission current.

4.4.1   The LEED pattern

In general, the LEED pattern reflects the symmetry of the 2D reciprocal lattice corresponding to the surface lattice. Examples of possible surface symmetries and their 2D reciprocal lattices can be found in several textbooks [6, 2]. Point group symmetry operations are conserved in the Fourier transformation from direct to reciprocal space. Therefore threefold and fourfold rotation axis are easily recognized in the diffraction pattern. The analysis of the diffraction patterns is hampered by the addition of inversion symmetry as one can only detect the absolute square of the diffracted wave field amplitude, not its phase. In rare occasions, the surface is visible as a single domain lattice. For multiple-
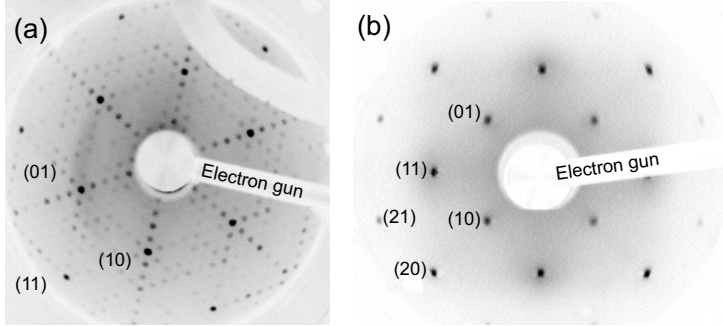
Figure 4.7: LEED patterns of (a) Si(111)7×7 at 100 eV, and Cu(001)1×1 at 218 eV. The integer order spots are indexed. (For clarity the negative images are shown.)

domain surfaces, it can be difficult to discriminate 3-fold from 6-fold and 2-fold from 4-fold rotational axes.

As a consequence of the reciprocal relationship between the real space lattice and momentum space lattice, the formation of large supercells gives rise to many diffraction satellites in between the main diffraction spots. For instance, the LEED pattern of the Si(111)7×7 surface shows many superstructure spots, as show in Fig. 4.7(a). The bright indexed spots or 'integer order reflections' reflect the symmetry of the primitive bulk-truncated lattice; the smaller superstructure spots or 'fractional-order spots' in between are due to the 7×7 super cell. The superstructure spots divide the distance between the main spots into seven equal parts.

The intensity of the observed spots varies with energy, as explained in section 4.2.4. The maximum intensity is reached at energy ($= \mathbf{k}$) values for which the 3D Laue conditions are fulfilled ($\mathbf{s} = \mathbf{k}_o - \mathbf{k}_i = \mathbf{g}$). An example of a typical I(V)-curve is shown in Fig. 4.8. This curve shows the averaged intensity of the (10), (01), ($\bar{1}$0), and (0$\bar{1}$) spots of Cu(001) as a function of energy. This averaging is allowed, since the presence of 90° rotated domains on the surface result in equal intensity profiles in these four beams. The major peaks (indicated by solid arrows) can be identified as Bragg peaks, while the minor peaks (indicated by open arrows) are due to multiple scattering effects. It can be clearly seen that the distance between subsequent Bragg peaks in the curve increases with energy. In k-space however, the peaks are equidistant.

From the position of the Bragg peaks in k-space, the real part of the inner potential V_{0r} can be determined. Since the electrons gain an amount of energy eV_{0r} when entering the surface, inside the crystal the Laue conditions can be written as:

$$\frac{\hbar^2 \mathbf{k}_{Bragg}^2}{2m} = E_k + V_{0r} = E_{Bragg}, \tag{4.15}$$

with E_k the electron's kinetic energy outside the crystal. The observed Bragg
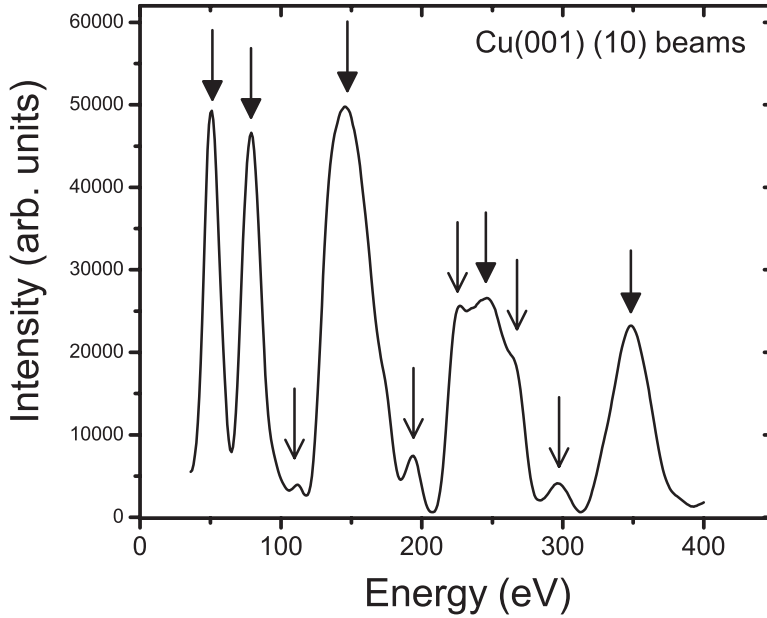
Figure 4.8: Experimental I(V)-curve of the four (10) beams of Cu(001) averaged. The Bragg peaks are marked by solid arrows, the multiple scattering peaks are marked by open arrows.

peaks at energy E_k are a few eV lower than the ones calculated for zero inner potential V_{0r}. By plotting of the observed Bragg peak energies against the calculated Bragg peaks for zero inner potential V_{0r}, one can determine the real part of the inner potential V_{0r} from the axis intercept. The data of Fig. 4.8 yield a value for V_{0r} of 5.0 ± 0.3 eV.

4.5   Structure determination with LEED I(V)

Analyzing a LEED pattern, one can obtain information about the size and symmetry of the surface unit cell. The background intensity in the diffraction pattern provides information about the roughness of the surface. More information can be obtained by measurement of the I(V)-curves of the visible spots. From the position of the Bragg peaks, one can estimate the interatomic distances. But the most powerful application of the LEED experiment is surface structure determination.

Due to the significant contribution of multiple scattering, direct Patterson inversion of the I(V)-curves does not give reliable results for atomic positions. Surface structure determination is generally performed by comparing measured I(V)-curves and calculated I(V)-curves of an assumed atomic arrangement. The procedure is illustrated in Fig. 4.9.
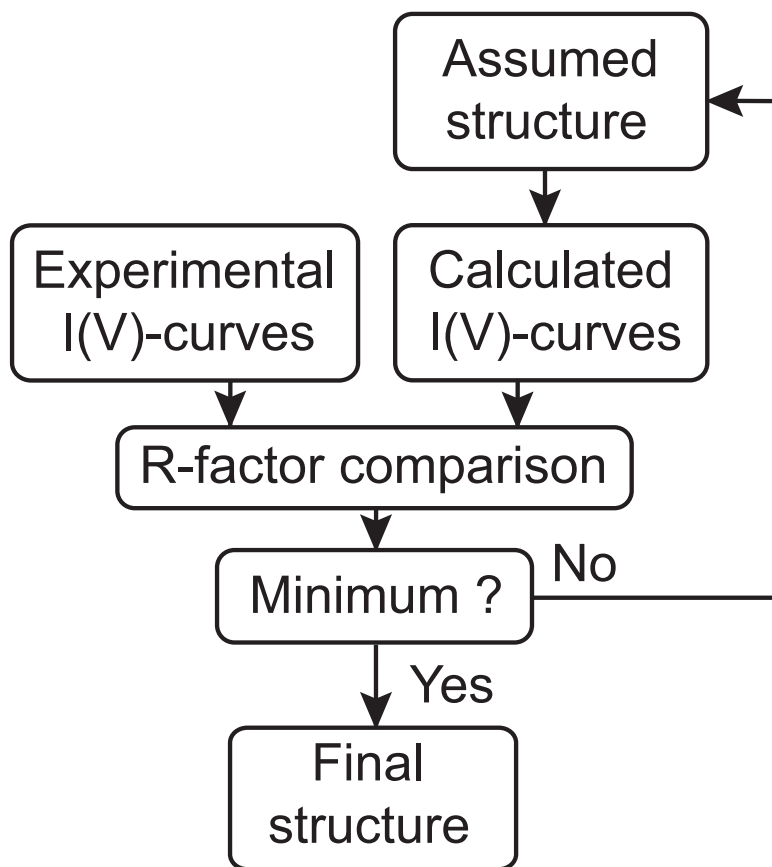
Assumed structure

Experimental I(V)-curves

Calculated I(V)-curves

R-factor comparison

Minimum ?   No

Yes

Final structure

Figure 4.9: Schematic drawing of the followed procedure for surface structure determination in LEED–I(V).

Data acquisition and analysis goes as follows. First, LEED images at various beam energies are recorded and stored in computer files. Generally, the beam energy ranges from 20 to 400 eV with increments of 1 eV. A 1 eV step is usually sufficient to sample the peaks in the I(V)-curves. A computer program extracts the intensity of every spot on every image and returns the data as I(V)-curves. The experimental I(V)-curves provide the input for the iterative procedure of surface structure determination. This procedure starts by assuming a geometrical arrangement of the surface atoms. Using this geometry, a computer program performs full dynamical calculations and produces the theoretical I(V)-curves of the assumed structure. The comparison between theory and experiment is the beginning of an iterative procedure that will be describes in the next section. The calculations were performed using programs from the Barbieri / Van Hove Symmetrized Automated Tensor LEED (SATLEED) package [7]. The atomic phase shifts needed for the dynamical treatment are calculated with the Barbieri / Van Hove phase shift package [7].

4.5.1   Tensor LEED

In the LEED experiment, only the intensity of the diffracted beams can be measured, the phase information is lost. This lack of phase information prohibits the calculation of the atomic structure of the surface from the diffracted intensities. In the past, surface structure determination was essentially a trial and error process. I(V)-curves were generated for each trial structure, using dynamical diffraction theory. The calculated I(V)-curves were compared with the experimental I(V)-curves by means of an R–factor.

Nowadays, perturbation theory is used to search for the structure with the minimum R–factor. The SATLEED code calculates the I(V)-curves of a trial structure and uses perturbation theory to calculate the changes in the I(V)-curves caused by small ($\pm$ 0.1 Å) atomic displacements from the initial trial structure. The calculated and experimental curves are compared via an R–factor, and the R–factor minimum is determined within the range of infinitesimal displacements.

The displacement of an atom j in the surface changes the scattering $\mathbf{t}$-matrix as follows:

$$\hat{\mathbf{t}}^j = \mathbf{t}^j + \delta\mathbf{t}^j(\delta\mathbf{r}_j), \qquad (4.16)$$

with $\delta\mathbf{t}^j$ the change of $\mathbf{t}^j$ due to the displacement $\delta\mathbf{r}_j$. With $|\phi(\mathbf{k})\rangle$ representing the exact state of the undistorted system, the change in diffracted amplitude becomes:

$$\delta A = \sum_j \langle\phi(\mathbf{k})|\delta\mathbf{t}^j|\phi(\mathbf{k})\rangle \qquad (4.17)$$

and the diffracted intensity can now be written as:

$$I \propto |A + \delta A|^2. \qquad (4.18)$$

The calculation of the tensor $\delta \mathbf{t}^j$ allows for the evaluation of I(V)-curves from structures that are close to the initial trial structure, without the need for a new time consuming dynamical calculation. This first order approximation only works for small displacements, because multiple scattering between the displaced atoms is not taken into account.

The structure corresponding to the R–factor minimum acts as the new 'assumed structure' and the process of dynamical calculations and R–factor comparison is repeated until the atomic displacements that minimize the R–factor have been reduced to (almost) zero. This defines a local minimum. To find the global minimum, several other structures have to be checked. If they all converge to the same local minimum, then this local minimum is likely to be a global minimum.

4.5.2   Fitting parameters

In order to fit the experimental and calculated spectra, one also needs to optimize the so-called non-structural parameters. These are the real and imaginary part of the inner potential and the (surface) Debye temperature Θ_D. The real part of the inner potential V_{0r} is fitted by the SATLEED program; it causes the displacement of the I(V)-curve along the energy-axis (Eq. 4.15).

The imaginary part if the inner potential is not allowed to vary with energy (Eq. (4.9)) in the SATLEED code. It is treated as a constant which has to be fitted manually. V_{0i} relates to the width of the main Bragg reflections in the I(V)–spectra. A higher value for V_{0i} increases the absorption of electrons in the solid and reduces the thickness of the surface layer contributing to the diffraction. The Fourier transform of a thinner surface slab implies broader peaks in the I(V)-curves.

Temperature effects are included through the Debye-Waller factor $\exp(-2M)$, multiplying the intensities as $I = I_0 \exp(-2M)$. The Debye-Waller factor has the form

$$\exp(-2M) = \exp(-|\mathbf{s}|^2 \langle (\delta \mathbf{r})^2 \rangle) \propto \exp(-\frac{|\mathbf{s}|^2 T}{\Theta_D^2}), \qquad (4.19)$$

with temperature T, $\mathbf{s}$ the momentum transfer of the beam and $\langle (\delta \mathbf{r})^2 \rangle$ the mean square deviation of the thermal motion of the atoms. The Debye temperature is therefore a measure for the rigidity of the lattice with respect to vibrations (phonons). The smaller Θ_D, the larger M and the larger the influence of temperature on the spectra.

4.5.3   R–factors

The experimental and calculated I(V)-curves are compared via an R–factor. This R–factor is a crucial ingredient of the procedure of surface structure determination with LEED. It is preferable to assess the reliability of a certain assumed structure with a single number or quality parameter. Until the late

1970's, several R–factors ('R' from 'reliability') were used in LEED crystallography, but none of them was well suited for the purpose of LEED structure determination. Two groups have proposed more sophisticated LEED-I(V) R–factors, the groups of J.B. Pendry [8] and F. Jona [9]. The Pendry R–factor (R_P) is widely used in the LEED community, while the Zanazzi and Jona R–factor (R_{ZJ}) is no longer in use. In this section, the physics and mathematics of the Pendry R–factor is explained.

The development of the Pendry R–factor originates from the need for an R–factor that is first of all sensitive to peak positions. It should not be sensitive to absolute intensities, but it should pay some attention to relative peak intensities. Because of the noise in the experimental I(V)-curves, it should also not contain derivatives higher than first order.

Insensitivity to the peak amplitudes can be accomplished by taking the logarithmic derivative of the spectra:

$$L(E) = \frac{I'(E)}{I(E)}, \tag{4.20}$$

$I(E)$ represents the intensity versus energy or I(V)-curve. Comparison between the experimental and calculated $L(E)$ curves works well, except in cases where $I(E)$ goes to zero. To avoid such singularities, the $Y(E)$-function is defined as follows:

$$Y(E) = \frac{L^{-1}(E)}{L^{-2}(E) + V_{0i}^2}. \tag{4.21}$$

In the Y-function, all peaks are rescaled to the same height while their width remains unaffected. Fig. 4.10 shows the experimental I(V)-curve of Fig. 4.8 together with its Y-function. The Y-functions of the experimental and calculated I(V)-curves (Y_{exp} and Y_{calc}, respectively) can be compared in a standard way via the Pendry R–factor R_P:

$$R_P = \frac{\sum_{\mathbf{g}} \int (Y_{\mathbf{g},exp} - Y_{\mathbf{g},calc})^2 dE}{\sum_{\mathbf{g}} \int (Y_{\mathbf{g},exp}^2 + Y_{\mathbf{g},calc}^2) dE}. \tag{4.22}$$

In a usual structure determination, R_P is the average of the R–factors of the individual beams that are included in the fit. In the SATLEED program, every experimental I(V)-curve can be given a certain weight in the fitting procedure. An overall Pendry R–factor below 0.2 generally implies good agreement, whereas a $R_P > 0.5$ means that the assumed surface structure is not reliable.

4.6   Results for Cu(001)

To test the experimental LEED setup and the process of surface structure determination with the SATLEED package [7], a series of LEED images has been recorded from the unreconstructed Cu(001)1×1 surface.
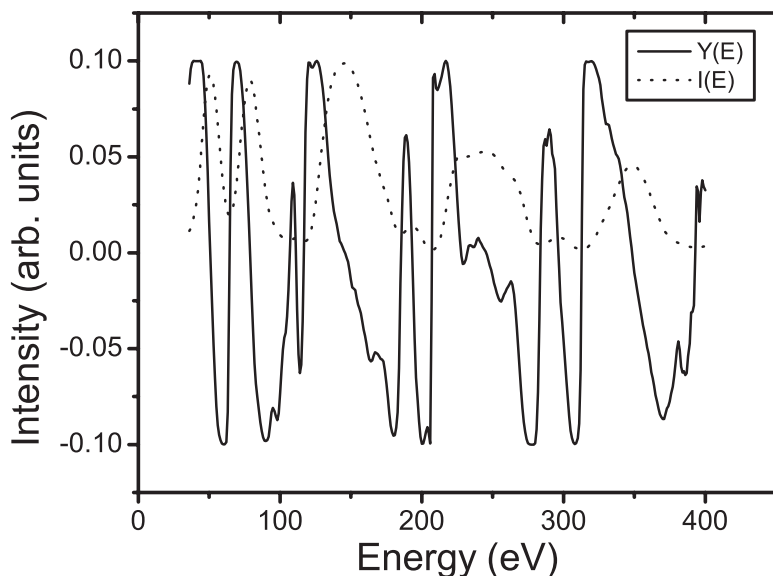
Figure 4.10: Gray: Experimental I(V)-curve of the four (10) beams of Cu(001) averaged (see also Fig. 4.8). Black: Y-function of this I(V)-curve.

The experiments were performed in a UHV chamber equipped with a LEED system with data acquisition facilities and Auger Electron Spectroscopy (AES). The base pressure of the system was 5×10^{-11} mbar. The Cu(001) sample was cleaned by cycles of Ar sputtering and annealing until no traces of contaminants were visible in AES and a sharp, low-background LEED pattern was observed. A series of LEED images was recorded with energies ranging from 30 to 400 eV with 1 eV energy increment per image and a filament emission current of approximately 0.5 mA. The experimental beams included in the fitting procedure were: (10) [4], (11) [3], (20) [4], (21) [8], (22) [3], and (30) [4]. (The numbers with between square brackets correspond to the number of symmetry-equivalent beams, which have been averaged). The fourth (11) and (22) beams are obscured behind the electron gun. The background has been subtracted for all beams.

In a well performed LEED experiment, symmetry-equivalent beams should have identical I(V)-curves. The presence of a magnetic field or small misalignment of the sample is manifested by differences in the I(V)-curves of symmetry equivalent beams. A nice check for the equivalency of the I(V)-curves is to calculate their mutual Pendry R–factor. According to Van Hove [2], a set of experimental beams can be regarded equivalent when the R–factors of all pairs are smaller than 0.10. The execution of this check showed that all R–factors in the Cu(001) dataset were smaller than 0.09. The values for the low order beams (10) and (11) were even smaller than 0.06.
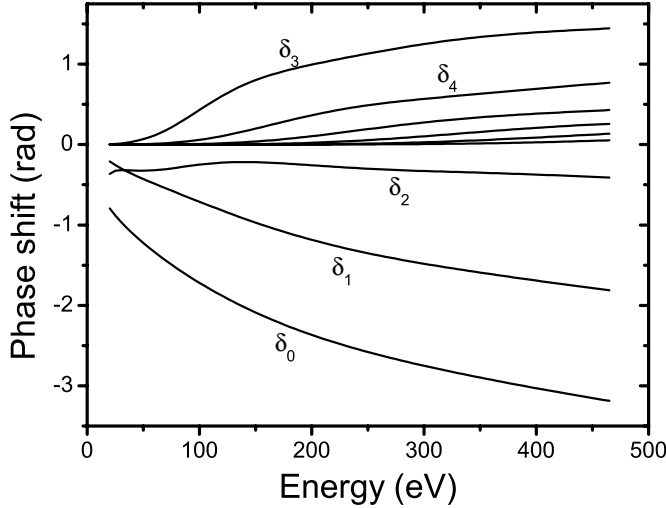
Figure 4.11: Atomic phase shifts δ_l for Cu as a function of energy, calculated by the Barbieri / Van Hove phase shift package [7].

A set of 10 atomic phase shifts was obtained with the Barbieri / Van Hove phase shift package [7]. A plot of the calculated phase shifts for bulk Cu is shown in Fig. 4.11.

The starting point of the fitting procedure was the fcc Cu(001) bulk truncated structure with a lattice parameter of 3.610 Å. The starting value for the inner potential was $V_0 = V_{0r} + iV_{0i} = 5 - 5i$ eV; the surface Debye temperature was 250 K. With these parameters an overall Pendry R–factor of 0.235 was reached (averaged over the six beams present). Then, the first five atomic layers of the Cu(001) surface were allowed to relax, but only perpendicular to the surface. The optimization of the imaginary part of the inner potential and surface Debye temperature is presented in Fig. 4.12 and 4.13, respectively. Both curves clearly show a minimum and the minimum values are found to be $V_{0i} = -5$ eV and $\Theta_D = 325$ K.

With these optimized values for the surface Debye temperature and inner potential, an overall R–factor of 0.164 was reached. Fig. 4.14 shows the I(V)-curves from the best fit, together with the experimental beams. Individual R–factors are shown for each beam. It can be seen that the experimental and calculated beams are very similar. The peaks and the majority of the shoulders from experiment are nicely reproduced by the calculations. In the optimization procedure, the weight of the individual beams in the structure determination was proportional to the energy region in which they were recorded.
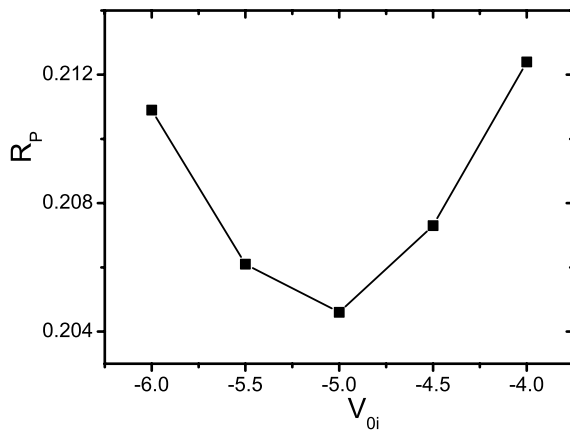
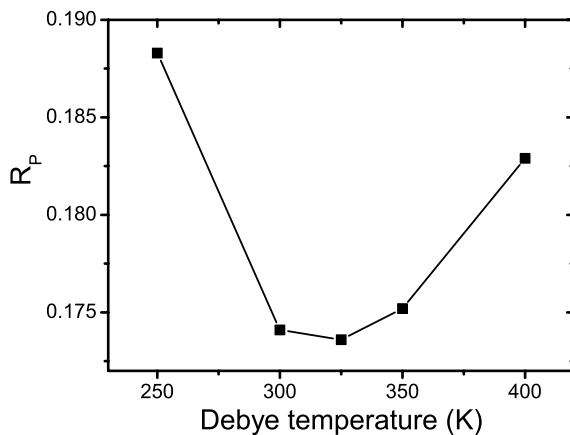Figure 4.12: Pendry R–factor as a function of the imaginary part of the inner potential.

Figure 4.13: Pendry R–factor as a function of the surface Debye temperature.
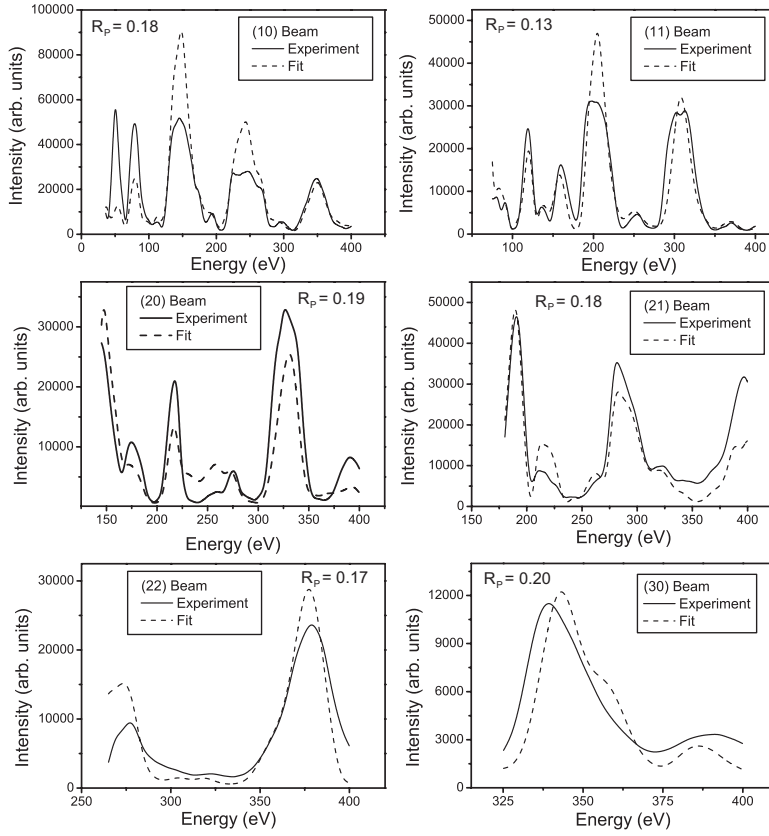
Figure 4.14: Experimental and theoretical LEED I(V) curves for Cu(001), with their individual Pendry R–factors.

Table 4.1: Comparison of structure determination results for Cu(001) from several groups. d_{12}, d_{23}, and d_{34} are the first, second and third interlayer spacing, respectively. Relaxations $\Delta(d_{12})$, $\Delta(d_{23})$, and $\Delta(d_{34})$ are in percentage deviation from bulk value. Typical error bars for the LEED experiment are indicated.

Reference	Method	V_{0R} (eV)	V_{0i} (eV)	Θ_D (K)	$\Delta(d_{12})$ (%)	$\Delta(d_{23})$ (%)	$\Delta(d_{34})$ (%)
This work	LEED	5.14	5.0	325	-1.1	0.1	-0.1
[10]	LEED	$V_{0R}(E)$			-1.8	0.4	-0.2
[11]	LEED		4.7	327	-1.0	0.4	0.4
[12]	LEED			235	-1.4	0.8	0.6
[13]	MEIS				-2.4	1.0	
[14]	LEED				-1.2	0.9	
Error bars	LEED				0.3	0.4	0.6

The parameters of the best-fit structure are displayed in Table 4.1, together with the structure parameters from other experiments. All experiments show a contraction of the first interlayer spacing, as expected from the theory presented in Section 2.7. There is a small spread in the magnitude of the relaxations, however, among the different experiments. Medium energy ion scattering (MEIS) indicates larger layer relaxations; LEED data all indicate smaller relaxations. Some spread may be due to differences in measurement temperature. The third and higher interlayer spacings exhibit a large spread in values. Both the measurement temperature and the cleaning procedure of the Cu(001) surface can be the cause of this spread.

The optimized value for the surface Debye temperature is smaller than the value for bulk Cu (443 K). A smaller value is expected, because the surface atoms have a larger vibrational amplitude than bulk atoms (Section 4.5.2). The optimized value is also in good agreement with the other LEED experiments. The fitting procedure could be made more sophisticated by assigning a different Debye temperature to every single atomic layer. The value for the imaginary part of the inner potential, -5.0 eV, is also in good agreement with other reports [3, 11]. Some of the LEED studies used an energy dependent imaginary part of the inner potential, $V_{0i}(E)$. This is justifiable, because the inelastic mean free path depends on energy (Fig. 4.3). Surprisingly, none of the other LEED studies on Cu(001) reported a best-fit value for the real part of the inner potential. Therefore a comparison of V_{0r} could not be made.

In conclusion, we have outlined the theory and procedures for structure determination via LEED-I(V). The results of our study of the unreconstructed Cu(001) surface are in good agreement with other state-of-the-art LEED-I(V) studies.

Bibliography

[1] C. J. Davisson and L. H. Germer, Nature **119**, 558 (1927).

[2] M. A. van Hove, W. H. Weinberg, and C. M. Chan, *Low-Energy Electron Diffraction* (Springer Verlag, Berlin, 1986).

[3] C. Kittel, *Introduction to Solid State Physics, 6th edition* (Wiley, New York, 1986).

[4] J. B. Pendry, *Low Energy Electron Diffraction* (Academic, London, 1974).

[5] Ismail, *The structure and dynamics of magnesium surfaces* (PhD thesis, The university of Tennessee, 1999).

[6] H. Lüth, *Surfaces and Interfaces of Solid Materials, 3rd edition* (Springer, Berlin, 1995).

[7] A. Barbieri and M. A. van Hove, private communication (http://electron.lbl.gov/leedpack/) .

[8] J. B. Pendry, J. Phys. C **13**, 937 (1980).

[9] E. Zanazzi and F. Jona, Surf. Sci. **62**, 61 (1977).

[10] S. Walter, Surf. Sci. **458**, 155 (2000).

[11] A. Mikkelsen and D. L. Adams, Phys. Rev. B **60**, 2040 (1999).

[12] S. Muller, Phys. Rev. Lett. **75**, 2859 (1995).

[13] Q. T. Jiang, P. Fenter, and T. Gustafsson, Phys. Rev. B **44**, 5773 (1991).

[14] D. M. Lind, F. B. Dunning, G. K. Walters, and H. L. Davis, Phys. Rev. B **35**, 9037 (1987).

Chapter 5

Structure determination of Pb films on Si(111)7×7

5.1   Introduction

Until recently, research on quantum size effect (QSE) focused almost exclusively on the electronic structure of quantum-confined objects, including that of thin films. The interplay between quantum size effects and morphological evolution of the films is a novel phenomenon which received considerable attention following the discovery of a 'magic thickness' and preferred island height in ultrathin metal films grown at moderately low temperature [1, 2]. The influence of the quantum size effect on the lattice relaxations, however, has hardly been investigated. This is surprising, considering the fact that the interplay between quantum confinement and atomic arrangement is one of the most fundamental questions in nanoscience.

Interlayer spacings in quantum confined thin films have been studied in recent years with STM [3], He atom scattering (HAS) [4, 5, 6], and X-ray scattering [7]. However, STM and HAS do not probe the actual positions of the ion cores in the film. Instead, they probe the electron density above the surface. DFT calculations [8, 9] on the other hand, have predicted thickness dependent relaxations in thin films, but it remains difficult to include the substrate in these calculations.

This Chapter presents a LEED structure determination study of Pb films on Si(111)7×7 as a function of thickness in the quantum size regime. It is found that the surface relaxations are affected by the quantum size effect, although the effects are quite small. The results will be discussed and compared with STM, He scattering experiments, and DFT predictions.

5.2   Experimental procedure

The experiments were performed in a ultra high vacuum (UHV) chamber lo-
cated at Delft University of Technology. The system was equipped with Auger
electron spectroscopy (AES), low energy electron diffraction (LEED) with data
acquisition system, ion gun, and liquid nitrogen sample cooling capability. The
base pressure was 4×10^{-11} mbar. To obtain a clean 7×7 reconstructed Si(111)
surface the sample was flashed by e-beam heating to 1100°C. After this flash,
no traces of contaminants were found by AES and LEED showed a very sharp
and low background 7×7 pattern.

High purity Pb (5N) was evaporated from a Knudsen cell at a tempera-
ture of 595°C. The angle of incidence was 40° from the surface normal to
allow for real-time monitoring of the Auger Electron Spectrum in order to cal-
ibrate the deposition rate. The sample was kept at room temperature during
the calibration run. The peak-to-peak intensity of the combined Pb(NOO, 96
eV)Si(LVV, 92 eV) Auger line decreases sharply during Pb deposition until the
coverage saturates at 0.65 ML Pb (Fig. 5.1). The absolute coverage at the
break point was determined by ex-situ Rutherford backscattering spectrometry
(RBS). In this chapter (and the entire thesis), the coverage of Pb is expressed
in terms of a close-packed Pb(111) monolayer (1 ML = 9.43×10^{14} atoms/cm^2).
Following this calibration procedure, the sample was flashed again and subse-
quently cooled to 100 K. Pb was then deposited using the same growth rate
as above; the growth rate in all experiments of this chapter was of the order of
0.15 ML/min.

The experimental I(V)-curves were obtained from the LEED images by
home built software. The program places a circle around a spot in the diffrac-
tion pattern and adds the intensity of all pixels within the circle. The back-
ground intensity is corrected for by subtracting the intensity of a nearby circle,
not placed on a spot, that is located at a similar distance from the center of the
pattern. The resulting I(V)-curves are checked to be independent of the size of
the circle used. Since the emission current from the LEED filament depends
on the electron energy, the measured intensities need to be corrected for the
beam intensity. The observed intensity is proportional to the emission current,
therefore the intensity at energy E must be divided by the emission current at
that energy. Experiments show that the emission current is only dependent on
the electron energy.

5.3   Experimental results

5.3.1   Morphology of the films

The growth of Pb on Si(111)7×7 has been investigated intensively during the
last decades [10, 11, 12]. Therefore, the initial stages of growth are well known
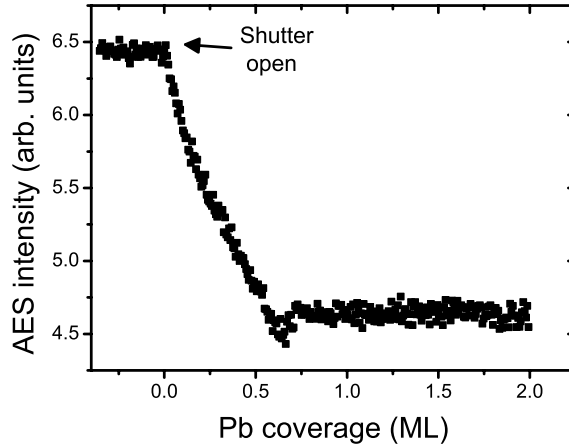
Figure 5.1: Intensity of the combined Pb-Si Auger line as a function of Pb coverage used for calibration of the Pb coverage. The intensity saturates at 0.65 ML Pb. (For the definition of ML, see text).

and observed many times by different groups and with different experimental methods.

At room temperature and below, in the initial stages of Pb growth (up to 0.15 ML) Pb atoms occupy 6 distinct sites in the 7×7 unit cell, while maintaining the 7×7 symmetry [11]. At higher coverages Pb atoms cover more of the Si substrate, until a full wetting layer is developed, still with 7×7 symmetry. During the growth of this wetting layer, the fractional order spots in the sharp Si(111)7×7 LEED pattern gradually disappear. The only fractional order spots that remain visible are the ones neighboring the integer order spots ($\frac{1}{7}$, $\frac{6}{7}$ and $\frac{8}{7}$ spots) and the ones located along the main crystallographic directions (Figure 5.2(a)). Combined LEED, STM and RBS studies [10, 11] identify this phase as having a Pb coverage of 0.66 ML. From the STM results, the authors propose a model with 8 Pb atoms along the Si(111)7×7 unit cell axes, while the remaining Pb atoms are distributed over sites above the top layer of Si atoms. The kink in the combined Pb-Si Auger line is likely to be caused by the stacking of Pb atoms on Pb atoms.

At higher coverages the background further increases, until Pb crystallites start to grow, with Pb(111) facets parallel to the Si(111) surface. The Pb islands are mainly oriented along the substrate axes, i.e., [110]Pb ∥ [110]Si, but exhibit a 6° mosaic spread (Fig. 5.2(b)). The LEED pattern shows sixfold symmetry, in contrast with the threefold symmetry of the Si(111) substrate. This shows that ABC and ACB stacked domains are present in (nearly) equal amounts.
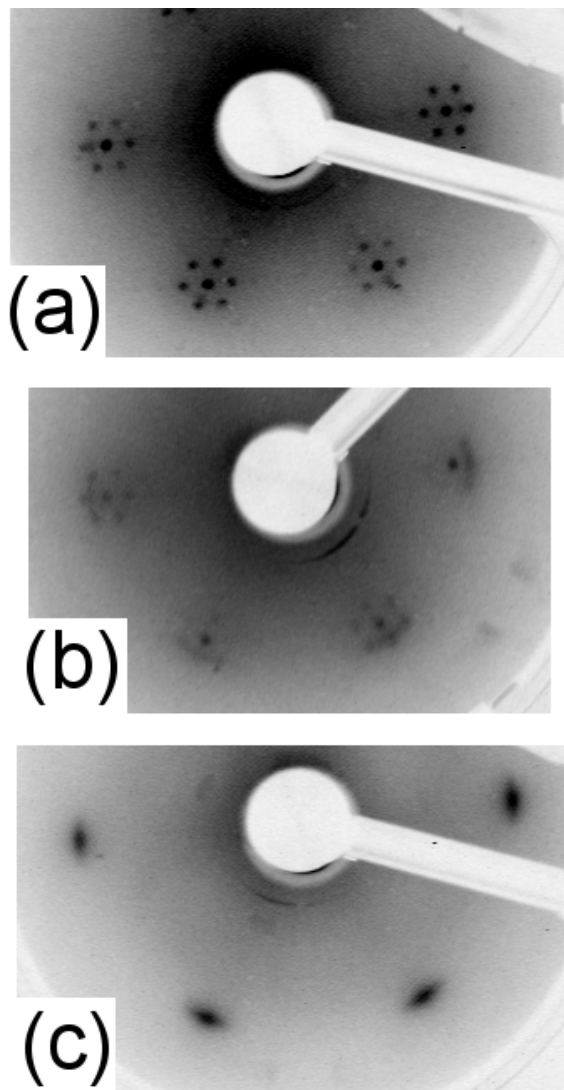
Figure 5.2: LEED patterns of characteristic Pb formations on Si(111)7×7. (a) The Pb wetting layer with 7×7 symmetry. (b) Pb(111) crystals on top of the wetting layer, at a total coverage of 2.5 ML. (c) Closed Pb(111) film.

These domains are rotated $60°$ with respect to each other, thus averaging the (10) and (01) diffracted intensities. This leads to equal intensity in the six (10) beams, the six (11) beams and the six (20) beams from the Pb layer.

The LEED intensity from the Pb islands shows some overlap with the fractional order spots of the wetting layer. The reason for this is the 10 percent smaller (in-plane) lattice parameter of Pb compared to Si(111). Consequently, the $\frac{8}{7}$ wetting layer spots coincide with the Pb(111) (10) spots. Within the $12°$ angular spread, the LEED intensity is equally distributed. There is no indication of a preferred coordination within this interval, in contrast with a previous LEED study [12] where a preference was observed for the $6°$ rotated island.

Upon increasing the Pb coverage at low temperature (less than 120 K), the Pb film closes. The fractional order spots of the wetting layer disappear first. The Si integer order spots disappear next and finally only banana shaped spots of the Pb crystallites remain visible in LEED. As the film is closed the mosaic spread narrows significantly (Fig. 5.2(c)). The spots remain banana shaped, but the angular spread is reduced. Fig. 5.2(c) is representative of the LEED patterns from which the I(V)–curves are obtained for the structure determination of the Pb films on Si(111)7×7.

For the purpose of structure determination, Pb films of 4, 5, 7, 8, and 9 ML nominal Pb coverage were grown at 110 K on Si(111)7×7. LEED intensity spectra (I(V)-curves) of the (10), (11), (20), and (21) beams were measured for each thickness, except for the 9 ML film of which only the (10) and (20) have been measured. The six symmetry equivalent beams from the various films always showed mutual R–factors smaller than 0.10, which is indicative of a good quality data set. Symmetry-equivalent beams were averaged before data analysis. The incident electron energy ranges from 50 to 250 eV with 1 eV increments, which is sufficient for sampling the peaks present in the intensity spectra. The large energy range also indicates good film quality. For comparison, in the Pb(111) bulk crystal LEED study of Ref. [13] spots were no longer visible above 200 eV beam energy.

5.3.2   R–factor analysis

The quantized energy levels in the film determine the stability, and are likely to influence the multilayer relaxation at the surface of the films. Strictly speaking, the electronic structure and stability of the Pb films exhibit *quasi* bilayer oscillations, i.e., bilayer oscillations are interrupted by even-odd crossovers that are separated by 9 ML (see Chapter 3). Here we focus on films between 4 and 9 ML thick. In this range, even thicknesses are energetically stable while odd thicknesses are unstable. Hence, the periodicity of these oscillations is exactly 2 ML.

Since the total charge density shows a 2 ML periodicity, one might also expect bilayer oscillations in the structural parameters of the film, as the lattice relaxations should be proportional to the derivative of the charge density vari-

ations (linear response regime [7]). The magnitude of this effect may be small, however, as we will learn from the following discussion.

A simple check for a possible bilayer periodicity in the structure of the films is to calculate the mutual (Pendry) R–factors [14] of the experimental I(V)–curves. If the structural parameters would indeed exhibit bilayer periodicity, then the mutual R-factors from the N and ($N \pm$ even) monolayer films should be systematically smaller for identical (h,k) diffracted beams. Alternatively, the mutual R–factors of N and ($N\pm$ odd) monolayer films should be higher.

The results of this analysis are shown in Tables 5.1 to 5.3 for the (10), (11), and (20) beams, respectively. The tables are symmetrical around the diagonal axis. Fig. 5.3 shows the experimental beams used in this analysis. The energy range of the (21) beam was too limited to calculate a reliable R–factor and was not included in this analysis. A low R–factor of two I(V)-curves means that the I(V)-curves are similar, while a high R–factor means less similarity between the two curves. From the argument of bilayer periodicity in the structure of the films, bilayer periodicity in the R–factors is expected.

Inspection of the tables shows that the expected bilayer periodicity in the R–factors is present for some beams, but much less pronounced in others. For example the (10) beam from the 5 ML film shows low R–factors when compared with identical beams from the 7 and 9 ML films (0.072 and 0.062, respectively). Comparison with the 4 and 8 ML films yields significantly higher R-factors (0.137 and 0.132, respectively). Some other beams do not show this behavior. Clearly, not all beams show a systematic bilayer trend which is possibly due to scatter in the data as well as variations in the film quality, such as surface roughness.

Therefore, to check for an overall trend, R–factors from all [N versus $N \pm$ even] and from all [N versus $N \pm$ odd] numbered layers have been averaged. Table 5.4 shows the results for the (10), (11), and (20) beams. The average R–factor from the [N versus $N \pm$ even] numbered layers shows a significantly lower value than the [N versus $N \pm$ odd] numbered layers. Even in the absence of a full blown LEED I(V) analysis, inspection of the raw I(V) data strongly suggests a bilayer periodicity in the structural parameters of the films.

5.3.3   Structure determination results

To obtain quantitative information about the atomic structure and relaxations of the individual films, the I(V)–spectra were analyzed with the Van Hove SATLEED software package [15]. The structural parameters to be optimized were the real and imaginary part of the inner potential V_{0r} and V_{0i}, the Debye temperature Θ_D and the first and second interlayer spacings d_{12} and d_{23}. No more than two interlayer spacings were included in the fit, since Pb is a strong scatterer and the spectra therefore do not obtain much information about the deeper layers. The third and higher interlayer spacings were kept fixed at their bulk values. The values of V_{0r}, d_{12}, and d_{23} were optimized by the fitting routines of the
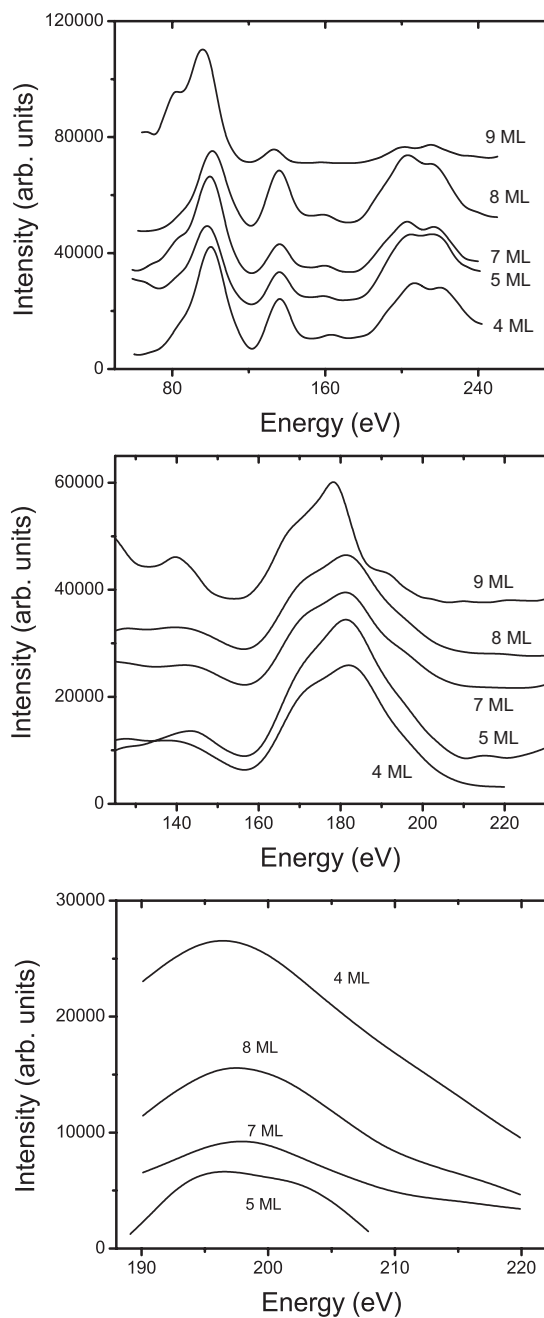
Figure 5.3: Experimental I(V)-curves of the 4, 5, 7, 8, and 9 ML Pb films on Si(111)7×7 used in the R–factor analysis. (a) (10) beams, (b) (11) beams, and (c) (20) beams.

Table 5.1: Mutual Pendry R–factors of (10) beams in experimental data sets. The energy of the I(V)-curves ranges from 50 to 220 eV.

(10) beams	4 ML	5 ML	7 ML	8 ML	9 ML
4 ML		0.137	0.085	0.105	0.175
5 ML	0.137		0.076	0.132	0.062
7 ML	0.085	0.076		0.094	0.095
8 ML	0.105	0.132	0.094		0.139
9 ML	0.175	0.062	0.095	0.139	

Table 5.2: Mutual Pendry R–factors of (11) beams in experimental data sets. The energy of the I(V)-curves ranges from 117 to 181 eV.

(11) beams	4 ML	5 ML	7 ML	8 ML	9 ML
4 ML		0.276	0.090	0.073	0.149
5 ML	0.276		0.170	0.199	0.174
7 ML	0.090	0.170		0.040	0.091
8 ML	0.073	0.199	0.040		0.091
9 ML	0.149	0.174	0.091	0.091	

Table 5.3: Mutual Pendry R–factors of (20) beams in experimental data sets. The energy of the I(V)-curves ranges from 125 to 196 eV.

(20) beams	4 ML	5 ML	7 ML	8 ML	9 ML
4 ML		0.106	0.115	0.067	0.188
5 ML	0.106		0.038	0.023	0.096
7 ML	0.115	0.038		0.032	0.075
8 ML	0.067	0.023	0.032		0.099
9 ML	0.188	0.096	0.075	0.099	

Table 5.4: Average Pendry R–factors of beams from thicknesses differing even and odd number of layers.

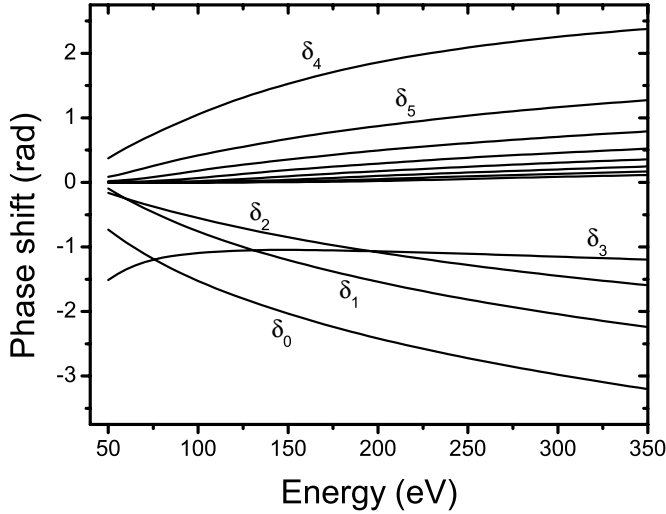| Beam	(10)	(11)	(20)
Average R(N vs. N±even)	0.090	0.127	0.072
Average R(N vs. N±odd)	0.127	0.141	0.094

Figure 5.4: Atomic phase shifts δ_l for Pb as a function of energy, calculated by the Barbieri / Van Hove phase shift package [15].

SATLEED program, while V_{0i} and Θ_D had to be fitted manually.

In the dynamical treatment of the scattered intensities, a set of 13 relativistic phase shifts was used ranging from 50 to 350 eV, calculated by the Barbieri / Van Hove phase shift package [15] and shown in Fig. 5.4. The 14th and higher phase shifts gave very small numbers and were not included in the calculations.

Since the SATLEED program only allows for the use of a single trial structure, the treatment of the domains present in the films needs attention. The $60°$ rotated domains average the observed LEED intensities of the (10) and (01) beams, for example, making it impossible to distinguish them. Therefore, in the SATLEED code the I(V)-curves of the (10) and (01) beams are both calculated and subsequently averaged. The part of the program that optimizes the atomic structure and R–factors now compares the averaged I(V)-curve with the measured one. Or, in general, the program must average those I(V)-curves that are also averaged in the experiment due to e.g. domains.

The first step in the search for the optimized structures was the determination of the values for V_{0i} and Θ_D. All of the five experimental data sets gave values for V_{0i} between -7 and -9 eV. The relaxations and R–factors only showed very small changes when varying V_{0i} between -7 and -9 eV and a value of -8 eV for V_{0i} was taken for all thicknesses during the remainder of the optimiza-

Table 5.5: Structure determination results for several Pb coverages on Si(111)7×7. The in-plane lattice parameter is fixed at 3.489 Å. Deviations from the bulk interlayer spacings are given as percentage.

Thickness (ML)	4	5	7	8	9
$\Delta(d_{12})$ (%)	-2.9	-3.3	-2.8	-2.3	-2.8
$\Delta(d_{23})$ (%)	+1.6	+0.5	+0.5	+1.1	+0.6
$V_{0R}(eV)$	4.9	4.8	5.1	5.5	4.1
$R_{P,tot}$	0.142	0.257	0.166	0.193	0.225
R_{10}	0.09	0.19	0.13	0.15	0.16
R_{20}	0.26	0.35	0.25	0.30	0.34
R_{21}	0.23	0.12	0.09	0.15	-

tion procedure. The same holds for Θ_D and a final value of 125 K was chosen, which is slightly larger than the literature value of 105 K [16]. Fig. 5.5 shows the total Pendry R–factor of three different data sets as a function of V_{0i} (a) and Θ_D (b). The overall similarity of the data sets with respect to these two parameters is represented by the coincidence of the minima. The vibration amplitude of the topmost Pb layer is enhanced in the search by a factor of $\sqrt{2}$, to take the reduced coordination of the surface atoms into account.

First, the five structures were optimized with a constant in-plane lattice parameter of 3.489 Å. The (11) beams were not included in the fit, because that produced high R–factors (> 0.4 in all data sets). The influence of the (11) beam on the structure determination results will be discussed in Section 5.3.4. The total Pendry R–factor $R_{P,tot}$ is a geometric average of the individual R–factors, and their weights were taken proportional to the energy range of the individual beams [17]. The results of the layer relaxations are given in Table 5.5.

The search for the global R–factor minimum for each film thickness started from a variety of trial structures. All calculations converged toward the same global R–factor minimum. Fig. 5.6 shows a contour plot of the total Pendry R–factor around the global minimum of the 7 ML film at $R_P = 0.166$ as a function of $\Delta(d_{12})$ and $\Delta(d_{23})$. The minimum is indicated by the black square. This R–factor landscape is typical for all five data sets. The SATLEED program does not allow for keeping the real part of the inner potential constant in the fit, it is always optimized. Therefore, R-factors outside the minimum tend to be underestimated, because V_{0R} is always optimized at each location in the R-factor landscape of Fig. 5.6. The figure shows that the R-factor depends much stronger on $\Delta(d_{12})$ than on $\Delta(d_{23})$; i.e., the curvature of the landscape is stronger in the horizontal than in the vertical direction. Clearly, the parameter d_{12} is the dominant contributor to the R-factor. The experimental and calculated I(V)-curves of the 7 ML data set are shown in Fig. 5.7. The I(V)-curves of all five data sets can be found in Appendix A.

The uncertainties in the values of $\Delta(d_{12})$ and $\Delta(d_{23})$ can be obtained [14]
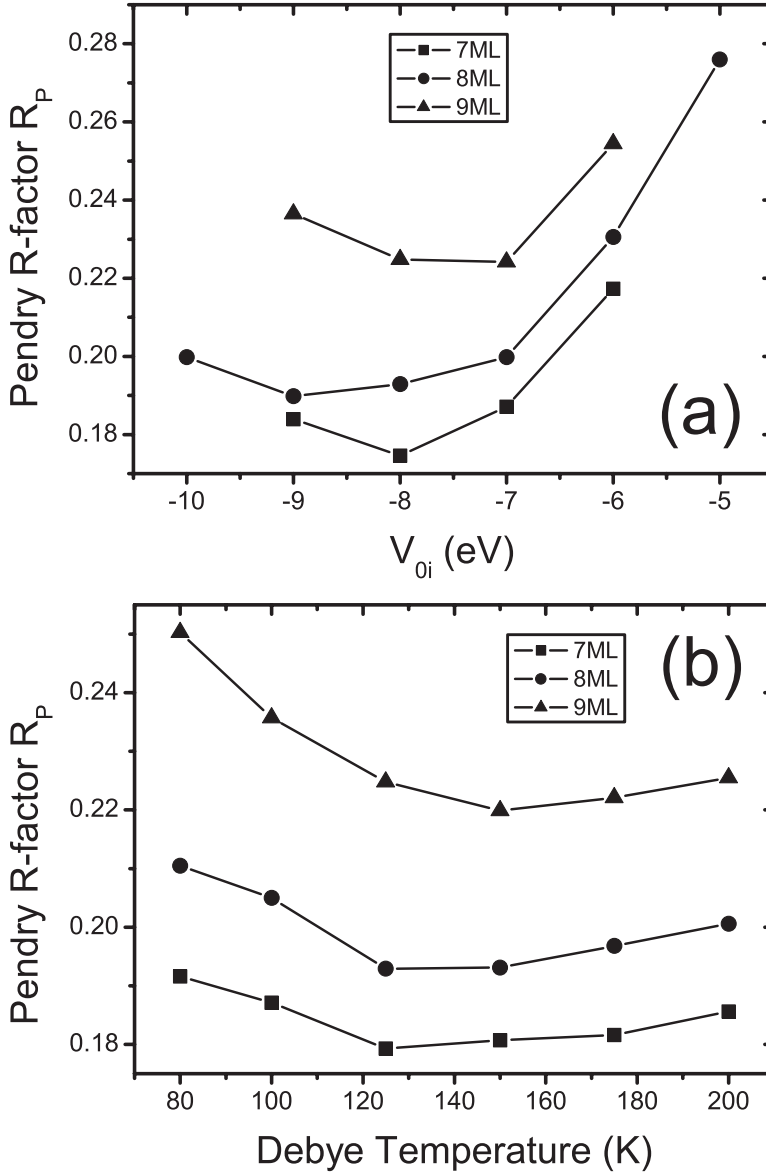
Figure 5.5: Pendry R–factor as a function of imaginary part of the inner potential V_{0i} (a) and Debye temperature Θ_D (b) for the 7, 8, and 9 ML datasets. The optimum values are -8 eV and 125 K, respectively.
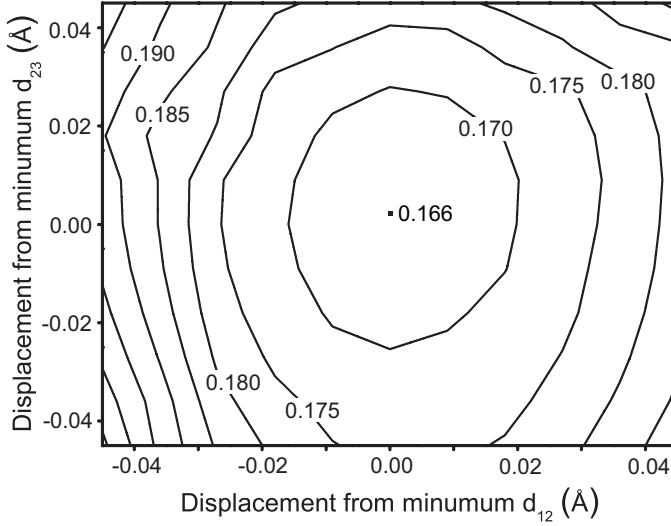
Figure 5.6: Contour plot of the total Pendry R–factor $R_{P,tot}$ as a function of $\Delta(d_{12})$ and $\Delta(d_{23})$ in Åfor the 7 ML optimized structure. The minimum ($R_{P,tot}$ = 0.166) is indicated by the black square.

from the variance σ of the total Pendry R–factor:

$$\sigma = R_{P,min} \sqrt{\frac{8|V_{0i}|}{\Delta E}}, \tag{5.1}$$

with $R_{P,min}$ the Pendry R–factor at the global minimum and ΔE the total energy range of the experimental data set. The uncertainty in $\Delta(d_{12})$ is given as $\Delta(d_{12})(R_{P,min} + \sigma) - \Delta(d_{12})(R_{P,min})$. All five data sets show similar curvature of the R–factor landscape as a function of d_{12} and d_{23}. Taking into account the systematic underestimation of R_P in the R–factor landscape, this leads to uncertainties in $\Delta(d_{12})$ and $\Delta(d_{23})$ of 0.7% and 1.0% of the bulk interlayer spacing, respectively.

5.3.4   Stacking faults and the (11) beam

The fact that the structure determination in the previous sections is performed without the (11) beam raises the question what influence this beam has on the results. Since the (11) beam is the beam most sensible to stacking faults on fcc(111) and hcp(0001) surfaces [18], it has to be investigated whether the high R–factor of this beam can be related to deviations from the Pb fcc stacking sequence. Therefore, the 8 ML data set has been investigated for the existence of stacking faults.

Assuming that the top layer Pb atoms are located in the 'A position' of a closed-packed stacking arrangement, we can place the second layer atoms
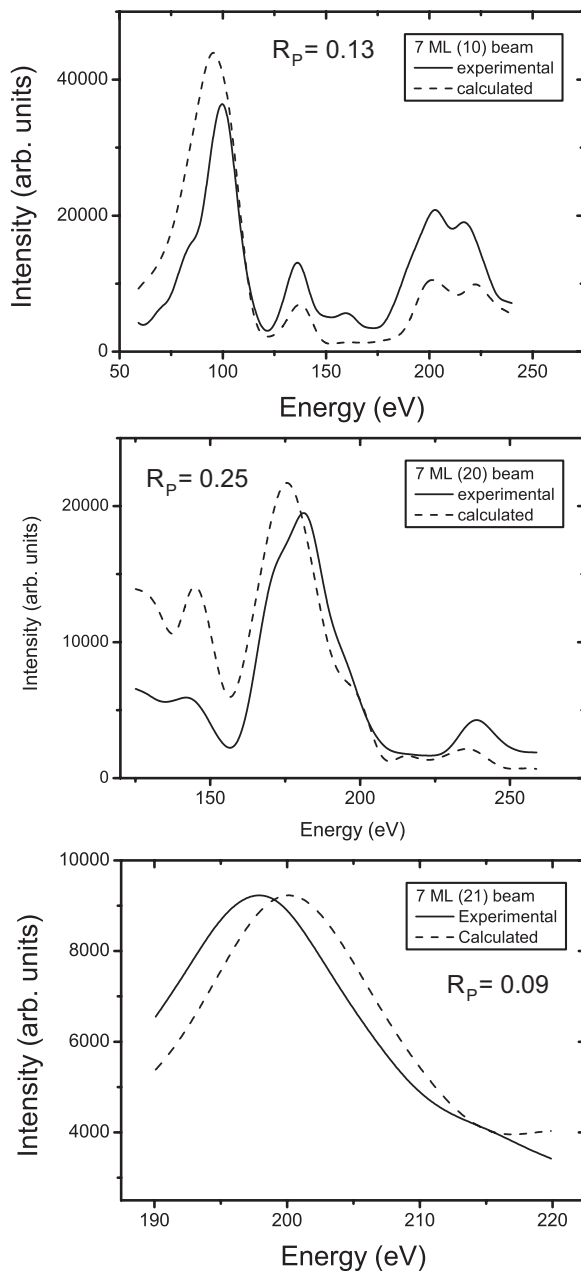
Figure 5.7: Experimental (solid line) and calculated (dotted line) LEED I(V)-curves from a 7 ML Pb film on Si(111)7×7. Images of all data sets can be found in Appendix A.

Table 5.6: Pendry R–factors of the 8 ML data set tested for stacking faults. The results of the
fcc structure are shown and of the two stacking faults.

Structure	R	fcc	$ABABCABC\ldots$	$ABACABCABC\ldots$
Without (11) beam	$R_{P,tot}$	0.19	0.20	-
With (11) beam	$R_{P,tot}$	0.28	0.33	0.32
With (11) beam	$R_{P,11}$	0.43	0.62	0.59

in either the B or C positions. We already know that both possibilities oc-
cur with equal probability since the LEED pattern has the six-fold symme-
try (Sec. 5.3.1). This twinning (i.e., the coexistence of $ABCABC\ldots$ and
$ACBACB\ldots$ stacked domains) was already taken into account in the I(V) anal-
ysis (see Sect. 5.3.3). Therefore, in order to explore whether the high R–
factor of the (11) beam is related to stacking faults, we must consider devia-
tions from the above fcc stacking sequence. As we move into the crystal, we
only need to consider the following faulty stacking sequences: $ABABCABC\ldots$
and $ABACABCABC\ldots$. (For the unavoidable symmetry reasons mentioned
above, these are averaged with $ACACBACB\ldots$ and $ACABACBACB\ldots$, re-
spectively). Both cases amount to a stacking fault between the second and
the third layer. Stacking faults in deeper layers are not included because of the
very low sensitivity of the LEED experiment for the atomic positions in deeper
layers [20].

   The 8 ML data set has been tested for the two detectable stacking faults
with and without inclusion of the (11) beam. The results are displayed in Table
5.6. If we exclude the (11) beam from the analysis, the R–factor shows a
slight increase for the $ABABCABC\ldots$ stacking sequence, while for the other
stacking fault sequence no R–factor minimum was found. However, if all four
beams are included in the analysis, the total Pendry R–factor increases upon
the introduction of the stacking fault. This increase can be attributed exclusively
to the increase of R_{11} from 0.4 to 0.6; the R–factors of the other beams did not
change. The relaxations in the optimized structure including all four beams
differs only marginally from the three-beam fit in Table 5.5; $\Delta(d_{12})(4beams) =$
2.1% and $\Delta(d_{23})(4beams) = 1.0\%$. This analysis proofs that the (11) beam is
the most sensitive to stacking faults. Most importantly, however, it also shows
that the rather large R–factor of the (11) beam in the fully optimized structure
(i.e. Table 5.5) cannot be attributed to stacking faults.

5.4   Discussion and conclusions

Because similar multilayer relaxations lead to similar spectra, kinematic diffrac-
tion theory would predict low mutual R–factors for layers having similar relax-
ations. The results of Tables 5.1- 5.4 show that the Pendry R–factors for the
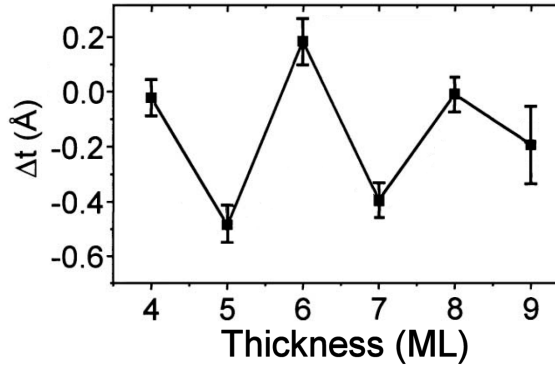
Figure 5.8: Atomic step heights between thickness $N-1$ and N measured with STM for Pb islands on Si(111). Figure from Ref. [3].

[N vs. $N \pm even$] numbered layers are significantly smaller than for the [N vs. $N \pm odd$] numbered layers. The R–factor analysis of the experimental spectra thus provides direct evidence for a bilayer periodicity in the multilayer relaxations of the films, without any need for a dynamical analysis of the intensities. The quantitative LEED analysis confirms the existence of bilayer oscillations in the surface relaxation, although the variations are quite small (Table 5.5). Notice that *the first interlayer spacing d_{12} is always contracted, regardless of the film thickness*.

The literature is quite confusing with regard to the magnitude of the multi-layer relaxations in quantum confined films. The Helium atom scattering (HAS) [4, 5, 6] and scanning tunneling microscopy (STM) [3] data have shown extremely large relaxations up to -30% for $\Delta(d_{12})$ and +15% for $\Delta(d_{23})$ around the bulk equilibrium spacing [5]. These very large relaxations must be attributed to electronic effects such as charge spilling from the quantum well into the vacuum, not to the relaxations of the atomic core positions. Similar arguments can be given for the huge oscillatory behavior of the step heights observed in STM [3], Fig. 5.8. Clearly, reliable structure parameters can only be obtained via X-ray diffraction or LEED I(V) analysis.

There have been two attempts recently to measure the multilayer relaxations in quantum-confined Pb films with X-Ray diffraction and X-Ray reflectivity. Floreano et al. [6] concluded that the outer layer spacing, d_{12}, oscillates around the bulk equilibrium value with an amplitude of +/- 5%. They noted that these oscillations are much smaller than those in their HAS experiments. The fitting of their rod scans required many parameters and hence, it is not easy to assess the reliability of the fit. Czoschke et al. [7] on the other hand used a simple theoretical model to reduce the number of fitting parameters. They fitted the X-Ray reflectivity data from a 10 ML Pb film on Si(111)($\sqrt{3} \times \sqrt{3}$) by modelling the film as a 2D quantum well system with hard wall potential

barriers. The total charge density $\rho(z)$ in the film was calculated by summing over all occupied, free-electron subbands. To include the effects of charge spilling, the width of the well was adjusted on both sides which introduces the 'charge spillage parameter'. The displacement of the atomic planes from their bulk positions was then taken proportional to the derivative $\partial\rho/\partial z$ of the theoretical charge density at the bulk location of the atomic planes. The resulting displacement pattern was then fitted to the experimental reflectivity data which produced a d_{12} contraction of 9% for 10 ML of Pb. (A 5% contraction was found for a 9 ML film [19]). This model also produced very large relaxations, although not as large as the HAS and STM results would suggest.

The model, though very transparent and elegant, is likely too simplistic. The charge distribution used for the fitting of the data is model dependent and may not be accurate, especially in the surface region, while the linear response approximation is probably not valid for relaxations as large as 9%.

On the theoretical side, DFT calculations of Pb(111) slabs [8, 9, 20] and Pb on Cu(111) [9] show that the actual differences in relaxation from layer to layer are much smaller than the above HAS, STM and X-ray reflectivity experiments would suggest. Fig. 5.9 shows the calculated relaxations for d_{12} and d_{23} of Pb(111) slabs as a function of thickness. The theoretical value of $\Delta(d_{12})$ oscillates around -5 % while the layer to layer variations are of the order of 1%.

Our LEED results are qualitatively consistent with DFT but indicate even smaller variations: -2.5 to -3% for $\Delta(d_{12})$ and +1% for $\Delta(d_{23})$, with a superimposed bilayer oscillation in $\Delta(d_{12})$ of $\approx$ 0.5% (0.01 to 0.02 Å). The even layers show a smaller d_{12} contraction than the odd layers, also consistent with DFT. In contrast to the STM and HAS results, both LEED and DFT indicate a contraction of the first interlayer spacing for all thicknesses. Our LEED I(V) results are consistent quantitatively with a dynamical LEED I(V) study [13] of bulk Pb(111), which reported $\Delta(d_{12})$= -3.5 ± 1.0% and $\Delta(d_{23})$ = +0.5 ± 1.4%. The discrepancy between the absolute magnitude of the relaxations in LEED and DFT can be attributed in part to thermal expansion of the lattice in the LEED experiment because the DFT result only applies to T = 0 K.

The amplitude of the superimposed quasi-bilayer oscillation in $\Delta(d_{12})$ of about 0.5% originates from the thickness-dependent modulation of the valence charge density. For comparison, this relaxation amplitude is similar to the structure modulations in weakly coupled incommensurate charge density wave systems [21, 22].

Although our data are qualitatively consistent with the DFT calculations, this does not automatically offer insight into the fundamental aspects that drive the layer relaxations. In the following, we will attempt to correlate quantum electronic structure with surface relaxations.

A parameter that is very sensitive to the surface charge density is the work function. The work function of free standing Pb films was calculated by M.Y. Chou (Fig. 5.10(b)). The work function also reveals quasi-bilayer oscillations. Comparison with Fig. 5.10(b) shows that the stable films have the largest work
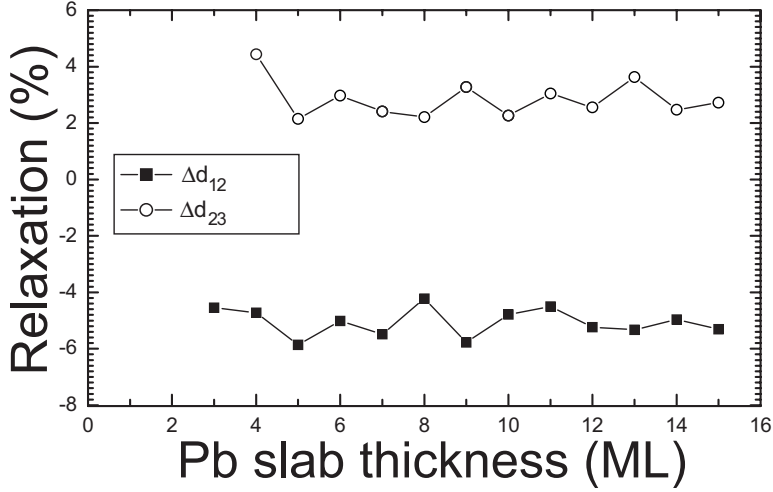
Figure 5.9: Calculated d_{12} and d_{23} relaxations as a function of slab thickness. Figure from M. Y. Chou [8].

function while the unstable films have the lowest work function. This oscillating work function can be directly related to the oscillating charge spilling from the quantum well. The tails of the wave function extending into the vacuum constitute a surface dipole layer and therefore contribute to the work function. The more charge spilling, the larger the dipole, the larger the work function. Evidently, charge spilling is largest for the stable films (6, 8, and 10 ML).

At first sight, this observation seems counter intuitive, since the quantum well states of the stable films are supposed to be deeper in energy than those of unstable films (see Chapter 2) and should therefore spill less charge into the vacuum. However, in order to calculate the total surface charge density, one has to consider the full two-dimensional subband dispersion, not just the states near Γ. Detailed jellium calculations show that the total charge spilling is smallest when the bottom of subband is located right at the Fermi level, and largest when the Fermi level is located exactly in between the highest occupied and the lowest unoccupied level at the Γ point [23].

It now appears that the data of Table 5.5 and the theoretical results in Figs. 5.9 and 5.10 can all be understood on the basis of this simple charge spilling concept. The theoretical maxima in the work function coincide with the smallest contraction of the first interlayer spacing. According to the discussion in Section 2.7, close-packed (111) surfaces usually show minimal relaxations, as opposed to open surfaces that are usually contracted (e.g. cubic (100) surfaces). On close-packed surfaces, there is not much 'room' for Smoluchowski charge smoothening and, consequently, much of the charge density remains located above the surface. In fact, many (111) surfaces show small expan-
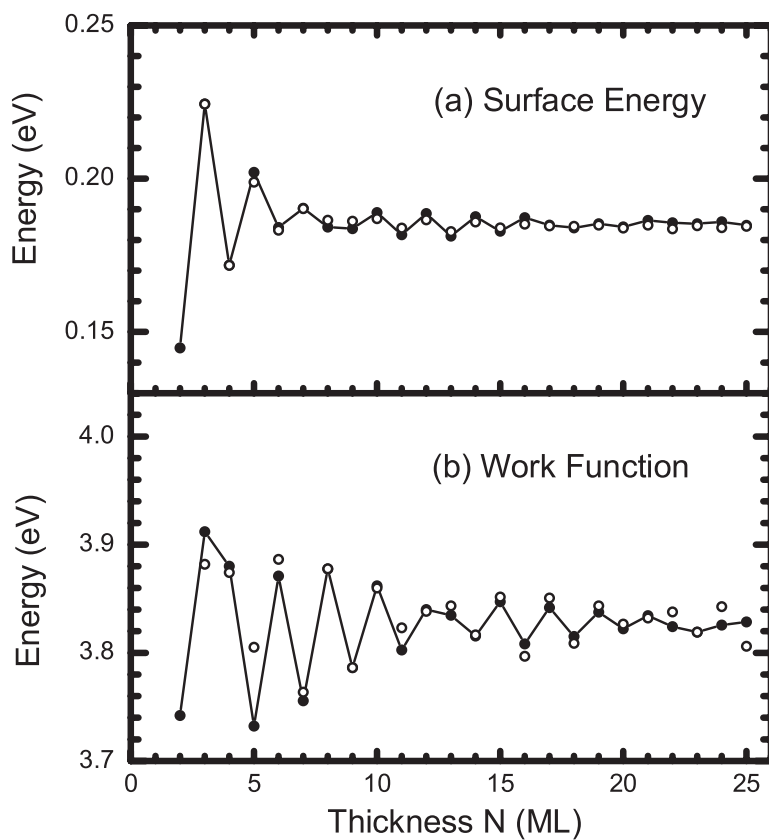
Figure 5.10: a) Surface energy per unit cell. b) Calculated work function as a function of slab thickness. Figure from C. M. Wei and M. Y. Chou [20].
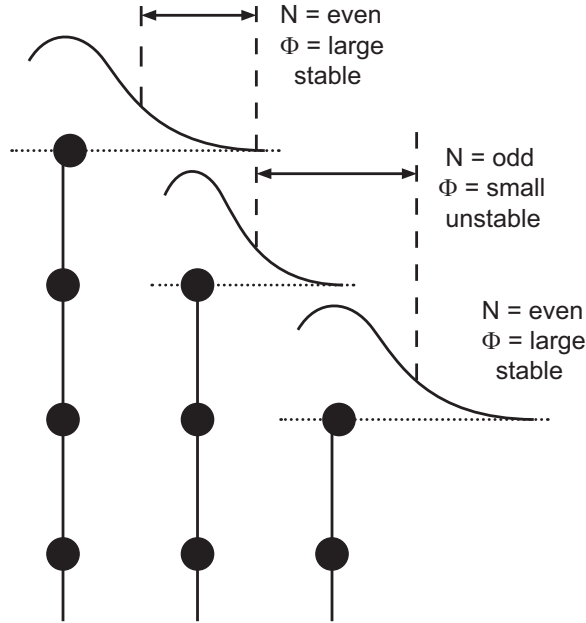
Figure 5.11: Schematic drawing of the increased charge spilling (and work function) in the even layers with respect to the odd layers. In the even layers the first layer atoms are pulled outwards, reducing the contraction.

sions as the ion cores move away from the crystal to compensate the excess charge density above the surface (Smoluchowski smoothening would lead to a contraction). Although there are many exceptions to this simple electrostatic argument (see e.g. Feibelman [24], in fact the 3.5 % contraction of the Pb(111) surface is also an anomaly), this argumentation appears to work quite well to explain the layer-by-layer variations of the d_{12} contraction. The larger work functions of the even layers correspond to more charge spilling and hence the outer layer expands relative to its bulk equilibrium value, meaning less contraction. This is consistent with the smaller contractions of the even layers in Table 5.5 and Figure 5.9. Fig. 5.11 illustrates the increased charge spilling (and work function) in the even and stable layers with respect to the odd and unstable layers.

This line of arguments should of course be checked against the STM and HAS results which are also very sensitive to surface charge density. STM results of Pb on Si(111)7×7 indicate that the step height between a 7 and 8 ML terrace is reduced while the step height between a 6 and 7 ML terrace is expanded (Su et al. [3]; this counting scheme includes the wetting layer). This suggests that the charge spilling from the $N = 7$ terrace is large while the

charge spilling from the $N = 8$ terrace would be small, opposite to the scenario outlined above (Fig. 5.11). However, STM experiments are most sensitive to states near the Γ point [25], while the step height is strongly dependent on bias. The STM step heights can in principle be calculated with DFT but this has not yet been done for the Pb films. Helium scattering data on the other had, are very confusing. For instance, the results presented by Crottini et al. in Ref. [5] suggest an expansion of step height between 7 and 8 ML, whereas the data presented Floreano et al. [6] indicate the opposite. Incidentally, these authors reference the same data set of Pb on Ge(100).

5.5 Summary

In conclusion, the surface relaxation of quantum confined Pb films has been determined with LEED I(V). The interlayer relaxations $\Delta(d_{12})$ and $\Delta(d_{23})$ have small values that are quite typical for close-packed fcc surfaces, showing a few percent contraction for the first interlayer spacing and a somewhat smaller expansion for the second layer spacing. The relaxations oscillate as a function of layer thickness with can be attributed to the bilayer oscillations in the electronic structure (i.e., the quantum size effect). The observed decreased contraction in d_{12} for the stable films can be explained by the increased charge spilling from the quantum well. The extremely large relaxations observed in He scattering and STM must be attributed to charge spilling effects, as these measurements probe the tails of the electronic charge distribution above the surface, not the atom core positions.

We finally remark that much effort has been devoted toward understanding surface relaxations on simple metal crystals. The usual approach is to compare the surface relaxations of different elements and different crystal orientations. These comparative studies have had mixed success [24, 26, 27]. Quantum confined Pb films, on the other hand, prove to be unique model system to test the simple electrostatic Finnis-Heine model of surface relaxations because the surface charge density of Pb(111) can be tuned by tuning the layer thickness. The present study unambiguously demonstrates the basic validity of the Finnis-Heine model.

Bibliography

[1] A. R. Smith, K. J. Chao, Q. Niu, and C. K. Shih, Science **273**, 226 (1996).

[2] K. Budde, E. Abram, V. Yeh, and M. C. Tringides, Phys. Rev. B **61**, R10602 (2000).

[3] W. B. Su *et al.*, Phys. Rev. Lett. **86**, 5116 (2001).

[4] J. Braun and J. P. Toennies, Surf. Sci. **384**, L858 (1997).

[5] A. Crottini *et al.*, Phys. Rev. Lett. **79**, 1527 (1997).

[6] L. Floreano *et al.*, Prog. Surf. Sci. **72**, 135 (2003).

[7] P. Czoschke, H. Hong, L. Basile, and T. -C. Chiang, Phys. Rev. Lett. **91**, 226801 (2003).

[8] M. Y. Chou, private communication .

[9] G. Materzanini, P. Saalfrank, and P. J. D. Lindan, Phys. Rev. B **63**, 235405 (2001).

[10] E. Ganz *et al.*, Surf. Sci. **257**, 259 (1991).

[11] E. Ganz, F. Xiong, I. Hwang, and J. Golovchenko, Phys. Rev. B **43**, 7316 (1991).

[12] H. H. Weitering, D. R. Heslinga, and T. Hibma, Phys. Rev. B **45**, 5991 (1992).

[13] Y. S. Li, F. Jona, and P. M. marcus, Phys. Rev. B **43**, 6337 (1991).

[14] J. B. Pendry, J. Phys. C **13**, 937 (1980).

[15] A. Barbieri and M. A. van Hove, private communication (http://electron.lbl.gov/leedpack/) .

[16] C. Kittel, *Introduction to Solid State Physics, 6th edition* (Wiley, New York, 1986).

[17] M. A. van Hove, W. H. Weinberg, and C. M. Chan, *Low-Energy Electron Diffraction* (Springer Verlag, Berlin, 1986).

[18] H. Ascolani *et al.*, Surf. Sci. **345**, 320 (1996).

[19] T. -C. Chiang, private communication .

[20] C. M. Wei and M. Y. Chou, Phys. Rev. B **66**, 233408 (2002).

[21] M. Bovet *et al.*, Phys. Rev. B **67**, 125105 (2003).

[22] A. Spijkerman *et al.*, Phys. Rev. B **56**, 13757 (1997).

[23] F. K. Schulte, Surf. Sci **55**, 427 (1976).

[24] P. J. Feibelman, Phys. Rev. B **53**, 13740 (1996).

[25] R. M. Feenstra, J. A. Stroscio, and A. P. Fein, Surf. Sci. **181**, 295 (1987).

[26] P. J. Feibelman, Phys. Rev. B **27**, 1991 (1983).

[27] J. H. Cho, Ismail, Z. Y. Zhang, and E. W. Plummer, Phys. Rev. B **59**, 1677 (1999).

Appendix A

LEED I(V) data fits

This appendix shows the experimental and calculated LEED I(V) spectra from the optimized structures of Table 5.5. In all the images, the solid lines indicate the experimental I(V) curves, while the dotted lines show the spectra calculated with the Van Hove SATLEED software package.
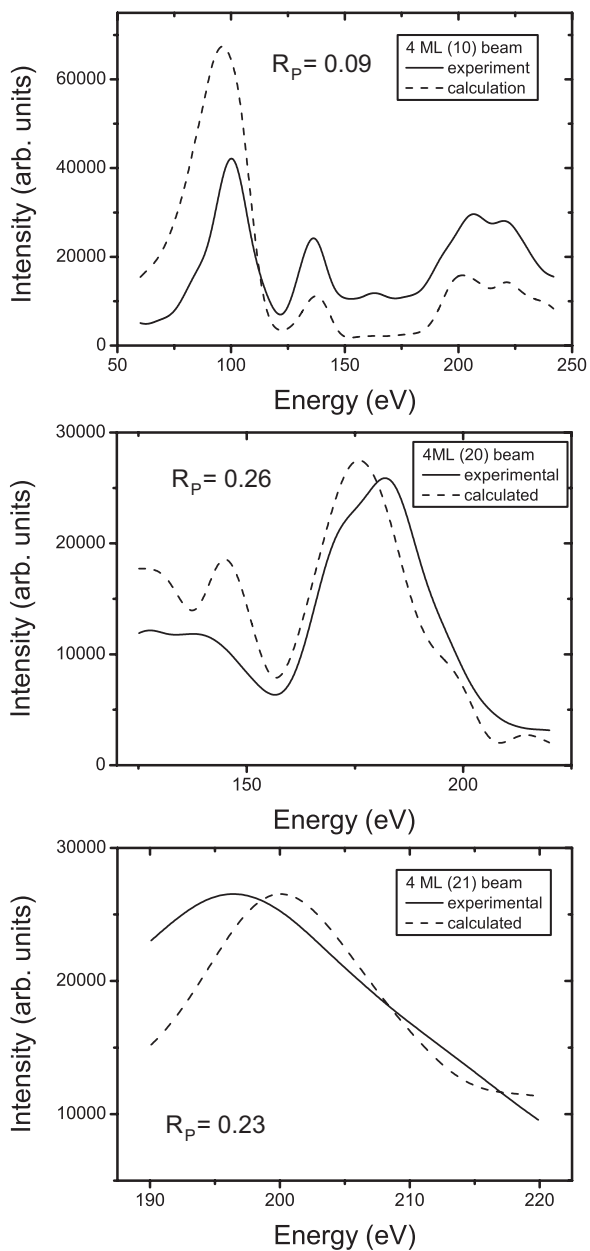
Figure A.1: Experimental (solid line) and calculated (dotted line) LEED I(V)-curves from a 4 ML Pb film on Si(111)7×7.
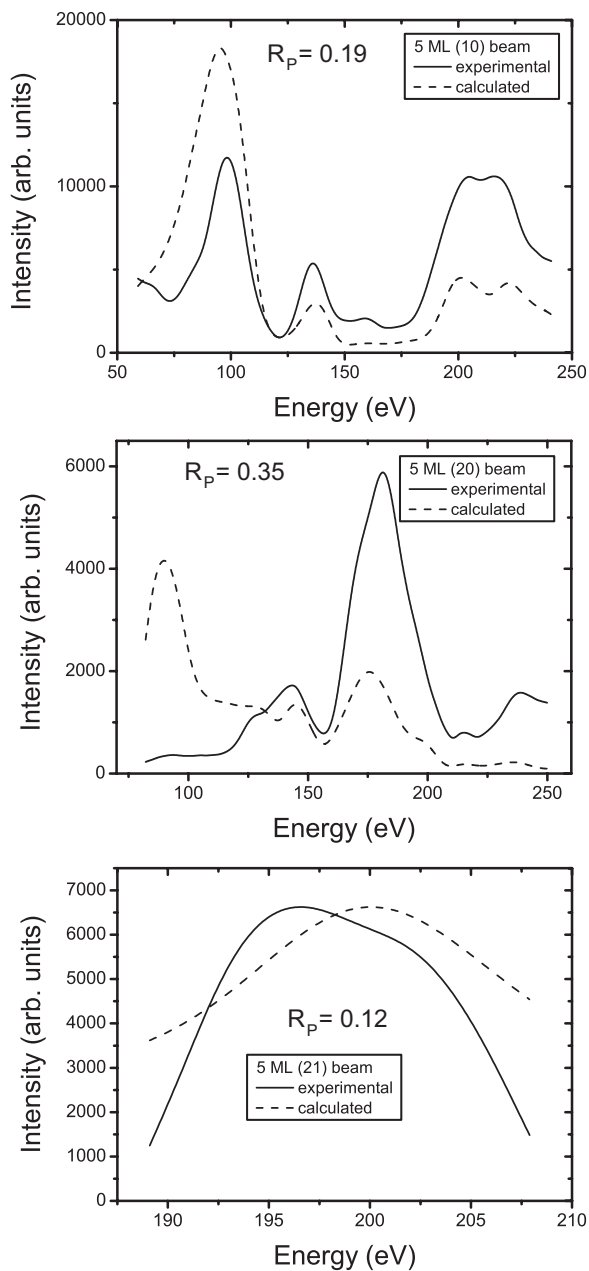
Figure A.2: Experimental (solid line) and calculated (dotted line) LEED I(V)-curves from a 5 ML Pb film on Si(111)7×7.
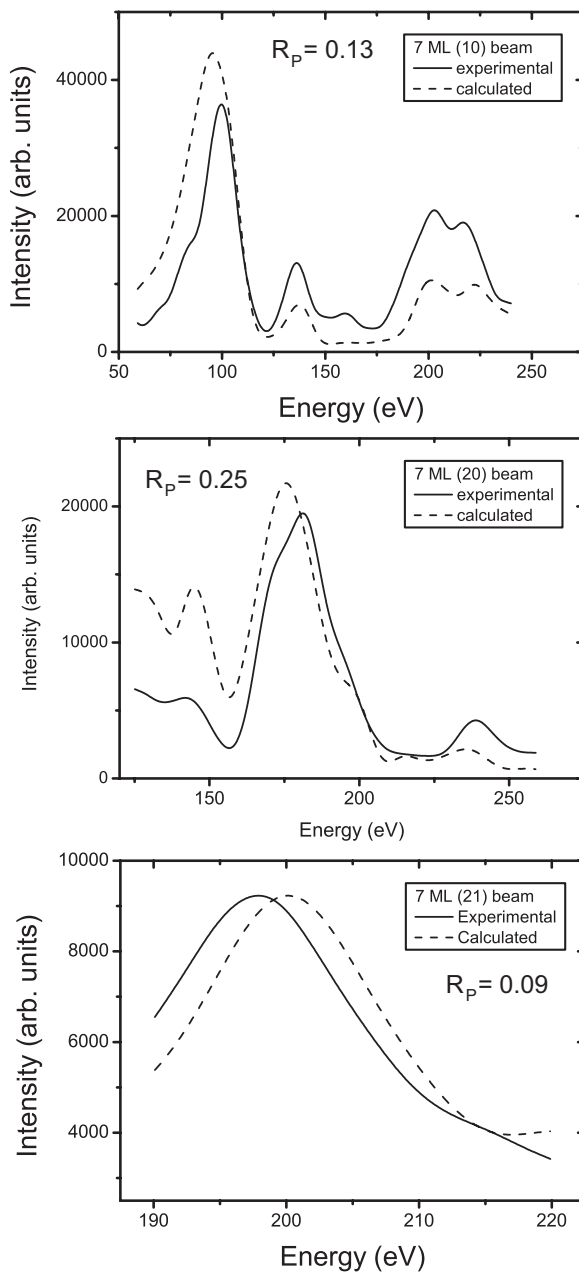
Figure A.3: Experimental (solid line) and calculated (dotted line) LEED I(V)-curves from a 7 ML Pb film on Si(111)7×7.
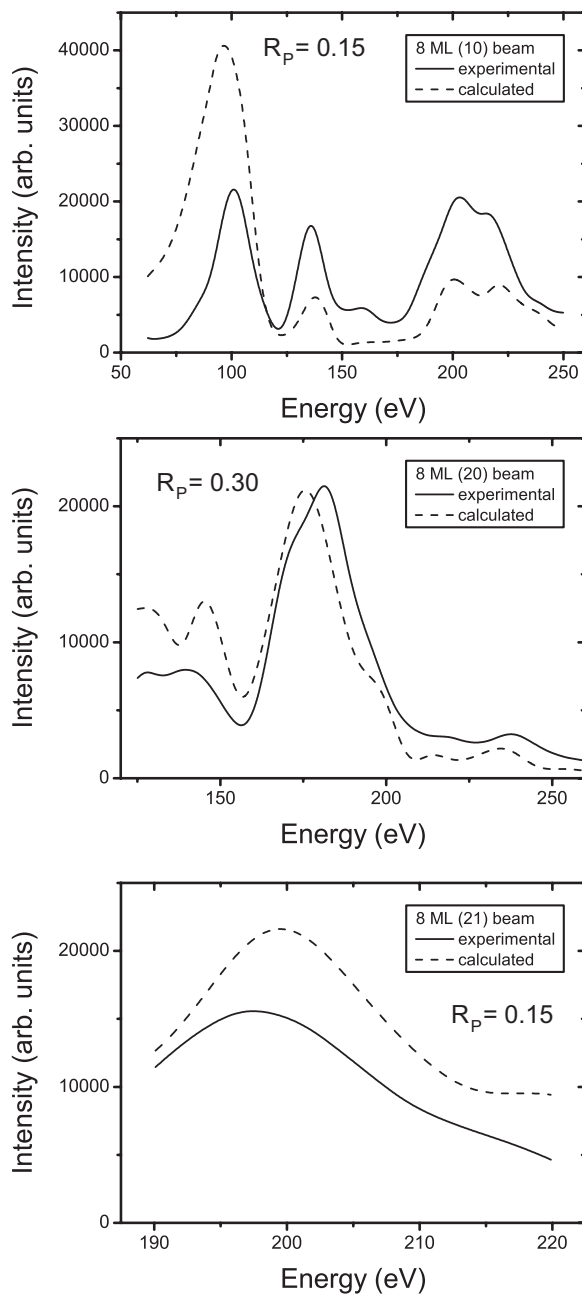
Figure A.4: Experimental (solid line) and calculated (dotted line) LEED I(V)-curves from a 8 ML Pb film on Si(111)7×7.
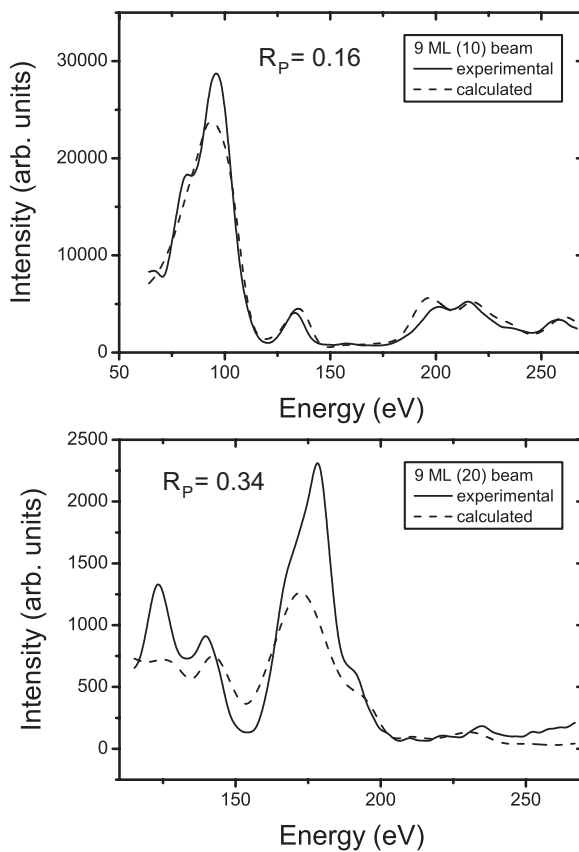
Figure A.5: Experimental (solid line) and calculated (dotted line) LEED I(V)-curves from a 9 ML Pb film on Si(111)7×7.

Summary

Epitaxial films that are only several atoms layers thick exhibit interesting properties associated with quantum confinement. When the coherence length of the electrons in the film is large enough, electrons will undergo multiple reflections between the surface and interface, producing electron standing wave patterns. The classical analog is that of a violin string, clamped at both ends. Only certain wavelengths are allowed while others cancel out. For electrons in an epitaxial thin film, this problem can be formulated in terms of the quantization of the wave number perpendicular to the film. This so-called 'quantum size effect' (QSE) alters the physical properties of the film, such as the resistivity, work function, or thermodynamic stability. The film acts as a potential well for the electrons, and therefore electron states with discrete wave numbers (or bound states) are called 'quantum well states'. In this thesis, we emphasize the consequences of the quantum size effect for the stability and lattice relaxations of Pb films grown on a Si(111)7×7 substrate.

Because the electron's wave number is directly linked to its energy via the band structure $E(\mathbf{k})$, the energy spectrum of the film becomes quantized. Electronic motion is characterized by two-dimensional subbands having fixed wave numbers perpendicular to the surface, and non-zero dispersion parallel to the surface. It is expected that this energy quantization must have an effect on the total energy, and hence the stability of the film. Angle resolved photoemission spectroscopy (ARPES) is a powerful technique to detect the occupied quantum well states. A high-intensity monochromatic light source is used to eject electrons from the surface. Their energy and parallel momentum can be measured directly. This experimental technique thus offers direct access to the two-dimensional band structure of a quantum confined film.

The first part of this thesis, consisting of the Chapters 2 and 3, introduces the quantum size effect and presents the results of ARPES measurements of Pb films on Si(111)7×7. Photoemission 'branches' are observed: films differing in thickness by an even number of atom layers accommodate quantum well states at approximately the same energy. These photoemission branches can conveniently be described by a reduced quantum number. This bilayer periodicity in the electronic structure is also reflected in the physical properties of the film. The photoemission branches cross the Fermi level whenever an integer

number of half Fermi wave lengths fit exactly in the film. These Fermi level crossings mark a crossover in the observed bilayer behavior: below nine layers even layers are more stable, whereas above nine layers the odd numbered ones are. The quantum well states are furthermore characterized by a large binding energy dependence of the in-plane effective mass and strong matrix element effects for photo-ionization. Finally, the analysis shows that the wetting layer observed in this system with scanning tunneling microscopy (STM) must consist of a single atomic layer instead of three, as was claimed in the literature.

The quantum size effect may also be manifested in the atomic positions or lattice relaxations. The second part of this thesis, consisting of the Chapters 4 and 5, describes low energy electron diffraction (LEED) experiments on ultrathin Pb films on Si(111)7×7. LEED, and especially the variety LEED I(V), is a suitable technique to measure the atomic positions, and therefore the lattice relaxations in the films. The results show a few percent contraction of the first interlayer spacing and a somewhat smaller expansion of the second layer spacing. Qualitatively speaking, this behavior is the same for all films, regardless of their thickness. However, the absolute magnitude of the first interlayer contraction oscillates as a function of film thickness. The oscillation period approximately corresponds to a bilayer of Pb. The decreased contraction of the first interlayer spacing in the even numbered layers (below 9 ML) nicely corresponds to an increased charge spilling from the quantum well. The measurements furthermore show that the extraordinary large relaxations reported from He scattering and STM experiments must be attributed to charge spilling from the quantum well, not to structural relaxations.

This thesis provides the first quantitative experimental analysis of atom layer relaxations induced by the quantum size effect. Although relaxations in quantum confined films are quite small, it is speculated that further confinement or lower dimensionality will yield larger relaxations or perhaps even induce a complete restructuring. These findings thus have interesting and important implications for the science and technology of materials and devices of *nanoscale* dimensions.

Samenvatting

Epitaxiale dunne lagen van slechts enkele atoomlagen dik vertonen interessante eigenschappen die te maken hebben met kwantummechanisch gedrag. Wanneer de coherentielengte van de elektronen in de laag lang genoeg is, kunnen ze meerdere malen weerkaatst worden aan het oppervlak van de laag en het grensvlak met het substraat. Dit heeft tot gevolg dat er staande golven van elektronen ontstaan. Het klassieke analogon van deze situatie is de vioolsnaar die aan beide uiteinden vast zit. Slechts bepaalde golflengten kunnen voorkomen als trillingen van de snaar, alle andere doven uit. Voor de elektronen in een dunne laag kan dit vertaald worden als de kwantisatie van het golfgetal in de richting loodrecht op het oppervlak. Dit zogenaamde 'quantum size effect' (QSE) beïnvloedt de eigenschappen van de laag, zoals de weerstand, werkfunctie en thermodynamische stabiliteit. De dunne laag is in feite een potentiaalput voor de elektronen en daarom worden de elektrontoestanden met discreet golfgetal 'kwantum put toestanden' genoemd. Dit proefschrift behandelt de gevolgen van het quantum size effect voor de stabiliteit en de roosterrelaxaties in dunne lood lagen, die gegroeid zijn op een Si(111)7×7 substraat.

Omdat het golfgetal van de elektronen direct gekoppeld is aan de energie via de bandenstructuur $E(\mathbf{k})$, wordt het hele energiespectrum van de laag gekwantiseerd. De beweging van de elektronen wordt weergegeven door tweedimensionale sub-banden, die een vast golfgetal hebben in de richting loodrecht op de laag en dispersie vertonen in het vlak. Het mag verwacht worden dat deze energie kwantisatie invloed heeft op de totale energie, en dus de stabiliteit van de laag. Hoek opgeloste fotoelektronen spectroscopie (ARPES) is een krachtige methode om de bezette kwantum put toestanden te detecteren. Een monochromatische lichtbron met hoge intensiteit wordt gebruikt om elektronen uit de dunne laag te halen. Hun energie en impuls parallel aan het oppervlak kan gemeten worden. Deze experimentele methode geeft dus directe toegang tot de tweedimensionale bandenstructuur van de film.

Het eerste deel van dit proefschrift, bestaande uit de hoofdstukken 2 en 3, beschrijft het quantum size effect en de resultaten van ARPES metingen aan dunne Pb lagen op Si(111)7×7. De fotoelektronen spectra worden gekarakteriseerd door pieken die geleidelijk verschuiven als funktie van de laagdikte.

Deze pieken vormen daarmee zogenaamde "photoemission branches". Afzonderlijke "takken" bevatten uitsluitend bijdragen (kwantum put toestanden) van even aantal atoomlagen, of van een oneven aantal atoomlagen. Deze fotoelektron takken kunnen worden beschreven met een gereduceerd kwantum getal. De waargenomen dubbellaags periodiciteit in de elektronische structuur wordt teruggevonden in andere eigenschappen van de laag. De fotoelektron takken kruisen het Fermi niveau wanneer een staande golf met de Fermi golflengte precies overeenkomt met de dikte van de Pb laag. Deze Fermi niveau doorgangen zijn een omslagpunt voor de waargenomen dubbellaags periodiciteit: even lagen zijn stabieler beneden de negen monolagen terwijl oneven lagen stabieler zijn daarboven. Verder worden de kwantum put toestanden gekenmerkt door een effectieve massa die sterk afhangt van de bindingsenergie en sterke matrix element effecten voor foto-ionisatie. Tenslotte laat onze analyse zien dat de eerste Pb laag aan het grensvlak, zoals deze is waargenomen in raster-tunnel microscoop opnames, zich al volledig sluit bij een laagdikte van slechts een enkel atoom; dit in tegenstelling tot eerdere publicaties waarbij een minimale laagdikte van drie atomen werd verondersteld.

Het is te verwachten, dat het quantum size effect ook terug te vinden is in de atomaire posities (of roosterrelaxaties). Het tweede deel van dit proefschrift, bestaande uit de hoofdstukken 4 en 5, beschrijft lage energie elektronen diffractie (LEED) experimenten aan Pb lagen op Si(111)7×7. LEED, en in het bijzonder de variant LEED I(V), is een geschikte methode om de atomaire posities, en dus de relaxaties, in de laag te meten. Het blijkt dat de afstand tussen de buitenste twee atoomlagen gereduceerd is met een paar procent ten opzichte van de laagafstand in de bulk. De afstand tussen de tweede en derde laag is daarentegen juist weer wat groter. Kwalitatief gezien is dit gedrag identiek voor alle onderzochte laagdiktes. De absolute waarde van de waargenomen contractie tussen de eerste en tweede atoomlaag oscilleert echter als functie van de laagdikte, met eveneens een dubbellaags periodiciteit. De verminderde contractie voor even atoomlagen komt overeen met een verhoogde hoeveelheid lading die uit de kwantum put puilt. De metingen laten verder zien dat de buitengewoon grote relaxaties die waargenomen zijn met STM en helium verstrooiingsexperimenten moet worden toegeschreven aan een verhoogde kans op het uitpuilen van lading uit de kwantum put, en niet zozeer aan veranderingen van de atomaire posities.

Dit proefschrift levert de eerste kwantitatieve experimentele analyse van de invloed van het quantum size effect op atomaire relaxaties. Hoewel deze veranderingen van de relaxaties klein zijn, mag er verwacht worden dat bij nog kleinere afmetingen of lagere dimensionaliteit, grotere veranderingen in de relaxaties optreden. Zelfs een overgang naar een andere structuur behoort dan tot de mogelijkheden. De bevindingen van dit proefschrift zijn daarom belangrijk en interessant voor die deelgebieden van de wetenschap die zich bezighouden met materialen en devices op nanometer schaal.

Curriculum Vitae

Anton Mans

29 juli 1975	Geboren te Dordrecht
1987 - 1993	VWO aan het Thuredrechtcollege te Dordrecht
1993 - 1997	Studie Technische Natuurkunde aan de Technische Universiteit Delft
1998 - 2002	Promotieonderzoek aan de Technische Universiteit Delft in de onderzoeksgroep 'Fysica van Electronische Materialen', onder leiding van Prof. H.H. Weitering
2002 - 2003	Wetenschappelijk Medewerker aan het Nederlands Meetinstituut
2004	Wetenschappelijk Medewerker aan de Universiteit van Amsterdam in de onderzoeksgroep 'Condensed Matter Physics', onder leiding van Prof. M.S. Golden

Nawoord

Het heeft iets langer geduurd dan verwacht en gehoopt, maar het is er dan toch van gekomen: een afgerond proefschrift. Dit boekje is een tegenvoorbeeld van een van de stellingen van een eerdere Delftse promovendus, die stelde dat het schrijven van een proefschrift naast het vaderschap een onmogelijke opgave is. Dit neemt echter niet weg dat ik de achterliggende gedachte van deze stelling volledig onderschrijven moet. Echter, zonder de hulp van promotoren, begeleider en technici was het inderdaad een onmogelijke opgave geweest. Degenen die bij de totstandkoming van dit proefschrift betrokken zijn geweest, wil ik daarom in deze plaats hartelijk danken.

In de eerste plaats moet ik dan mijn promotor Hanno Weitering noemen. Hanno, na mijn beginperiode als promovendus kwam jij naar Delft, wat resulteerde in een keerpunt in mijn promotietijd. Het onderwerp werd veranderd en de aanwezige expertise gecombineerd, wat geresulteerd heeft in dit proefschrift. Ik heb je aanwezigheid en kritische kijk altijd als heel inspirerend ervaren. Niet alleen heb ik veel over fotoemissie geleerd, maar belangrijker: een kritische kijk op experimenteren en het blijven stellen van (relevante) vragen. Zonder jouw inbreng zou dit proefschrift niet geworden zijn wat het nu is.

Ook Ad Ettema wil ik hier hartelijk bedanken, je enthousiasme voor de experimentele fysica heb je aan mij overgedragen: van de basics van UHV tot dynamische LEED theorie, het is allemaal even leuk. Ook bij het presenteren horen de vonken eraf te springen, iets waar jij me de ogen voor geopend heb. Verder natuurlijk de wekelijkse biertjes op vrijdagmiddag, hoewel ik daarin je enhousiasme niet helemaal kon bijbenen. Ook Fokke Tuinstra wil ik bedanken voor de begeleiding, voor het 'Delftse' promotorschap en alles wat daarbij komt kijken.

De LEED metingen uit hoofdstuk 5 zijn gedaan door Hugo, ook zijn inbreng tijdens de tweede bundeltijd in Lund was onmisbaar. Kennelijk is er wat van de inspiratie overgekomen, want de basis voor je interesse in een promotieplaats ligt misschien wel in Lund. Mijn roommate Conor mag ik natuurlijk niet vergeten. Altijd was er wat te beleven, met alkalibronnen in het lab of grappige e-mails. Daarnaast wil ik je hartelijk bedanken voor het lezen van het manuscript.

Zonder technische ondersteuning is een promotieonderzoek in de experi-

mentele natuurkunde natuurlijk onmogelijk, daarom wil ik de bijdragen van de technici hier nadrukkelijk noemen. Bij Charles, Herman en Ruud stond de deur altijd open om een nieuwe opdampbron of samplehouder te laten maken of diskquota te verhogen. Ook de verhalen over de nieuwste verbouwing van Ruud zullen me nog lang bijblijven. Voor de metingen in Lund was de assistentie van Balu erg nuttig, bij de RBS metingen bij AMOLF was er hulp van Jeroen Kalkman en Michiel de Dood. Administratieve ondersteuning was er van meerdere secretaresses, waarvan Margaret en Monique het grootste deel voor hun rekening namen.

Zonder een 'thuisfront' valt er natuurlijk niets te beginnen. Erika, je hebt me heel wat avonden af moeten staan aan de wetenschap. Ook het antwoord van mama: 'papa moet op zolder werken' werd al snel het commentaar van Michiel: 'papa moet zeker op zolder werken...' Michiel, Nanette en Jacqueline, jullie kunnen nu weer wat vaker computeren. Ook mijn ouders wil ik hier hartelijk bedanken voor de mogelijkheid om te gaan studeren en de onvoorwaardelijke steun tijdens mijn promotietijd. Maar bovenal, verstand is een gave, daarom komt mijn Schepper de meeste eer toe. Ik beschouw de gelegenheid om Zijn schepping te mogen onderzoeken als een groot voorrecht.